Doctoral Dissertation

Ferromagnetic properties of Na-K alloy clusters incorporated in zeolite low-silica X

（ゼオライト low-silica X 中の Na-K 合金クラスターにおける強磁性）

Luu Manh Kien

Department of Physics, Graduate School of Science

Osaka University

June 2015

Abstract

Zeolite low-silica X (LSX) has the FAU-type aluminosilicate framework, where the supercages and β-cages are arrayed in a double diamond structure. Zeolite LSX in the present study contains zeolite-cations xNa and $(12-x)$K per β-cage (or supercage), and has a chemical formula of $Na_xK_{12-x}Al_{12}Si_{12}O_{48}$. By the loading of guest nK atoms, Na-K alloy clusters are generated in these cages by the sharing of s-electrons.

In previous studies for Na-K alloy clusters at K-rich region $0 \leq x \leq 4.0$, ferrimagnetism and metallic properties have been observed at higher K-loading densities, but Na-rich samples at $x = 7.8$ have shown nearly non-magnetic properties. In the present study, Na-rich samples at $x = 7.3$ and 5.1 are prepared, and optical, magnetic and electrical transport properties have been investigated in detail. For $x = 7.3$, large Curie constants are observed for $8.2 < n < 9.7$, and simultaneously nearly pure ferromagnetic properties are observed at $8.6 \leq n \leq 9.5$. The optical reflectance spectra reveal the formation of new clusters at β-cages for $8 < n$. The origin of magnetic moments is assigned to these β-cage clusters, where supercage clusters are non-magnetic. The direct magnetic interaction between β-cage clusters, however, is not expected because of a large separation by double six-rings between them. Furthermore, the electrical resistivity measurements indicate nearly insulating states in all samples. In order to explain the origin of the ferromagnetism in insulating state, a model of the ferromagnetic superexchange interaction between β-cage clusters is newly proposed via supercage clusters with the sp^3 closed-shell configuration. For $x = 5.1$, similar results are observed, but magnetic properties are ferrimagnetic.

The ferrimagnetism observed at $0 \leq x \leq 4.0$ has been explained by a model of antiferromagnetic coupling between two non-equivalent magnetic sublattices, one of which is formed by the itinerant electron ferromagnetism at the supercage clusters and the other by localized magnetic moments of β-cage clusters. Present results at $x = 5.1$ are explained by the mixture of ferromagnetism and ferrimagnetism with a weak disorder. A larger electron-phonon interaction is expected in Na-rich systems, because the ionization energy of Na is larger than that of K. The x-dependences of magnetic and electrical properties are discussed in terms of the distribution of Na and K atoms.

Table of contents

Chapter I
Introduction

1.1 Novel electronic properties of arrayed alkali metal clusters

The studies on physical properties of metal clusters have become the occupation of numerous research groups from the middle of 20th century. A metal atom cluster is defined as a finite group of metal atoms, which are held together entirely, mainly, or at least to a significant extent, by bonds directly between atoms even though some non-metal atoms may be associated intimately with the cluster [1]. The first investigation on metal cluster was probably done by British physicist Lord Reyleigh, who found that the colors of the stained glasses caused by the scattering of light by small metal particles embedded in the glass. From the years of 1960s to 1970s, new cluster sources were developed and studied. In 1967, Robbins *et al*, produced clusters composed of few atoms in the gas phase. These clusters exhibited quite different properties when compared with bulk materials [2-3]. The first theoretical treatment on electronic properties of metal clusters was carried out by Kubo in 1962 [4]. He proposed that the novel electronic properties of metal clusters come from the discrete energy levels of conductions electrons. Moreover, magnetic moment can be realized in clusters composed of non-magnetic elements when they have odd number of electrons. More than twenty years later, in 1984 Knight *et al*., found that the electronic structure of alkali metal clusters behaved as a spherical shell model [5]. At the same time, Ekardt performed a calculation on the work function of small metal clusters by using the local density approximation applied to the spherical jellium-background model [6]. According to this model a small metal clusters can have quantum electronic 1*s*, 1*p*, 1*d*, 2s, 1*f*… with increasing order of energy. The studies on free metal clusters, which mentioned above, are quite effective to elucidate the electronic shell structure of alkali metal clusters. Nevertheless, direct physical measurements are not relevant on free metal clusters. Hence, alkali metal clusters embedded in matrices were used to investigate the quantum electronic states, surface plasmon exciations, hyperfine coupling and geometry of clusters [7−8]. However, physical properties of these clusters are ambiguous due to wide size distribution.

Zeolites, which have nanoporous crystal structure with periodically well-defined size cages, have emerged as a host material to create arrayed alkali metal clusters. The mutual interaction between these arrayed clusters are expected through sharing windows of cages. Therefore, macroscopic physical properties such as magnetic orderings are supposed to be occurred although there are no magnetic elements. Zeolites with different types of framework structure have been used to host alkali metal clusters. By loading alkali metal atoms into zeolites, arrayed alkali metal clusters are stabilized. Depending on the kind of alkali metal as well as framework structure, several magnetic orderings have been observed. Canted antiferromagnetism, ferrimagnetic and antiferromagnetic have been observed in K loaded in zeolite Linde Type A (LTA) [9-11], Rb loaded in zeolite LTA [12-15] and Na loaded in zeolite Sodalite (SOD) [16-18], respectively. Recently, the physical properties of Na-K alloy clusters incorporated in zeolite low-silica X (LSX) have been investigated. Zeolite LSX has the faujasite (FAU) type framework structure, where β-cage and supercage are arrayed in a double diamond structure. In this research, zeolite LSX contains both of Na^+ and K^+ cations as extraframework. By loading guest K atoms into zeolite LSX, Na-K alloy clusters are generated. The chemical formula of zeolite LSX with loaded nK atoms is given by $Na_xK_{12-x+n}Al_{12}Si_{12}O_{48}$ per β-cage (or supercage), where n, x, $Al_{12}Si_{12}O_{48}$ are K-loading density, Na-concentration and negatively charge framework of zeolite LSX, respectively. The chemical formula then can be abbreviated as K_n/Na_xK_{12-x}-LSX. Magnetic properties strongly vary depending on Na-concentration x as well as K-loading density n. At lower Na-concentration samples $x \leq 4.0$ (x = 0, 1.0, 1.5, 2.4 and 4.0), ferrimagnetic properties have been observed at specific region of K-loading densities n, where the Weiss temperatures are negative [19-22]. In particular, at x = 4.0 a clear Néel's N-type ferrimagnetism has been found for $6.7 \leq n \leq 8.0$ [19]. These ferrimagnetic properties are well explained by a model of two non-equivalent magnetic sublattices, which have antiferromagnetic interaction, one of which form itinerant electron network in supercage clusters, the other has localized magnetic moment in β-cage clusters. The antiferromagnetic interaction here is expected to realize through the single six-membered ring, which will be indicated in the FAU-type framework structure of zeolite LSX in chapter I. The interaction between localized magnetic moments with in β-cage clusters is assumed to be absent in order to explain the Néel's N-type ferrimagnetic properties. In real system, this kind of interaction is very rarely observed because β-cages are well separated by double six-

membered ring. The above experimental results at lower Na-concentration samples $x \leq 4.0$ obviously indicate that the ferrimagnetic properties strongly depend on the Na-concentration x and the K-loading density n. In addition, the region of K-loading density n, where the ferrimagnetic properties are observed, has a tendency to shift to lower K-loading density region with increasing the Na-concentration x. These systematically changes can be assigned to the differences in the electronic potential depth of β-cage [19].

In this study, we have prepared the samples at high Na-concentration $x = 7.3$ and $x = 5.1$ at various loading density n. Magnetic, optical and electrical transport properties have been investigated. Samples at $x = 7.3$ show the spontaneous magnetization at K-loading densities $8.6 \leq n \leq 9.5$. The magnetic properties at $x = 7.3$ can be assigned to nearly pure ferromagnetic property. The experimental results on optical measurements imply the formation of localized magnetic moments in β-cage clusters network. This is different with samples at lower Na concentration $x \leq 4.0$, where magnetic moments are assigned to form in both of supercage and β-cage clusters due to the ferrimagnetic properties. The electrical resistivity measurements carried out for samples with $x = 7.3$ reveal the insulating properties. A model of superexchange ferromagnetic interaction has been proposed in order to explain the origin of ferromagnetic properties at $x = 7.3$. In this model the ferromagnetic ordering of localized magnetic moments in β-cages is provided by the superexchange interaction through sp^3-like state of supercage clusters. In this dissertation, the results in physical properties of samples at $x = 7.3$ will be shown and discussed in details. The spontaneous magnetization has also been observed for sample $x = 5.1$ at K-loading densities $8.2 \leq n \leq 8.9$. The temperature dependence of magnetization curves of these samples resembles the ferrimagnetic properties. The scene of ferrimagnetic properties observed at $x = 5.1$ are considered to be difference when compared with those at lower Na concentration samples $x \leq 4.0$. In addition, insulating properites have been found for all K-loading densities of $x = 5.1$. A possibility of ferromagnetism with Anderson localization state at supercage clusters network coupled localized magnetic moments in β-cage clusters has been proposed in order to explain the ferrimagnetic properties at $x = 5.1$. The comparison on physical properties between $x = 5.1$, 7.3 and the other x samples are also carried out.

1.2 Introduction to zeolites

Zeolites are inorganic microporous materials, which have a three-dimensional framework structure where the nanometer-sized channels and cages are regularly arrayed. They allow some molecules to pass through and cause others to be either excluded or broken down due to the crystal structure with channels and pores. The term of "zeolite" was first introduced by Swedish mineralogist Alex Fredrik Cronstedt in 1756 when he discovered the first zeolite mineral. Based on his observation that they formed a frothy mass when heated in the blowpipe, he named the material "zeolite" from two Greek words "*zeo*" and "*lithos*" which mean "to boil" and "a stone", respectively [23]. The frothy mass A. F. Cronstedt saw, actually was the release of water from the pores of the zeolite crystal. For the next 200 years, zeolites have received many scientific research efforts and attentions. Zeolites have been widely used as commercial and industry materials with different applications.

Natural zeolites formed where volcanic rocks and ash layers react with alkaline groundwater. Currently, the world's annual production of natural zeolite is about nearly three million tones [24]. Beside the natural zeolites, which exploited in nature, some kinds of synthetic zeolites can be manufactured by several procedures. Most zeolites are synthesized by dissolving a source of alumina and a source of silica in a strongly basic aqueous solution. Ultimately, the solubility, the silica-to-alumina ratio, the nature of the cations and the synthesis temperature of the resultant gel determine what structure is formed [25]. Synthetic zeolites hold some key advantages over their natural analogs. And synthetic desirable zeolite structure, which does not appear in nature, also can be formed. Up to now, zeolites have been used in a variety of application with a global market of several million tones per annum because of their unique porous properties. The larges single use for zeolite is the global laundry detergent market. In petrochemical industry, synthetic zeolites are widely used as catalysts, for instance in fluid catalytic cracking and hydrocracking. Zeolites also used as ion-exchange beds in domestic, water purification and in the separation and removal of gases and solvents. Other applications are in construction, agriculture, medical, animal husbandry, nuclear industry and so on.

There are several zeolite materials have been known and each kind of zeolite material have their own name. Zeolites can be named by place of discovery, by people who

found them or by the organization where zeolites were synthesized. Some early synthetic zeolites named by alphabet as zeolite A, X or Y. All of zeolites can be classified according to various schemes, for example by pore openings, by structural subunit, by channel system, by framework density, by the loop configurations, or by coordination sequences. Until now, there are 197 different framework structures. A set of three letters code is assigned to confirmed zeolite structure type by the Structure Commission of the International Zeolite Association according to the rules set up by an IUPAC (International Union of Pure and Applied Chemistry) Commission on Zeolite Nomenclature [26-27]. The codes are normally derived from the name of zeolite or "type material". For example, FAU comes from the mineral faujasite or LTA from Linde Type A. New codes are still approved and will be announced on the web page of IZA (International Zeolite Association) Structure Commission.

Aluminosilicate zeolites have the three-dimensional framework, which consist of two types primary structural units of alumina tetrahedra (AlO_4) and silica tetrahedra (SiO_4). These tetrahdra can be connected to each other by the oxygen-sharing leading to the forming of interconnected voids and channels inside the framework [28]. Water molecules normally occupy in these voids and channel, but they can be removed out of zeolites framework by dehydrated process. Each SiO_4 tetrahedron has neutral charge because of silicon ion has +4 charge and it can be balanced by the charge of four oxygen anions. While each AlO_4 tetrahedron has -1 negative charge due to +3 charge of aluminum, which is not balanced with four oxygen anions's charge. Therefore the framework of aluminosilicate zeolites has the negative charge. Normally, the negative charge of framework can be compensated by cations, which have univalent or divalent as Li^+, Na^+, K^+, Rb^+ or $Mg^{2+}$and Ca^{2+}. With the appearance of these cations, the charge of the framework will be balanced. These cations also can be exchanged by the others due to their mobility, the possible in ion-exchang process of zeolites leads to changing in properties of zeolites. Some special applications of zeolites as waste water treatment of molecular sieves based on this property. A typical chemical formula of aluminosilicate zeolite is given by:

$$\mathbf{M_{a/m}Al_aSi_bO_{2(a+b)}.}w\mathbf{H_2O}$$

where "m" is the valence of cation "M", "w" is the number of water molecules per unit cell and "$(a+b)$" is the total number of tetrahedra per unit cell. The value of "m"

is 1 for the case of Li, Na, K, Rb… and is 2 for the case of Mg or Ca. The Si/Al ratio "*b*/*a*", which represent the relation between the number of Si and Al atoms in zeolite, is normally 1 - 5 but this ratio can be increased to 100 in the case of high silica zeolites.

Information of the zeolite framework type can explain many of the observed properties of a zeolite. The zeolite framework type, which describes the topology of the framework tetrahedral atoms in the highest possible symmetry without reference to chemical composition, defines the size and shape of the pore openings, the dimensionality of the channel system, the volume and arrangement of the cages and the distribution of cation sites. However, the chemical composition of the zeolite framework type, the nature of species within the channels and the type of post-synthesis modification also play as an important role in determining the specific properties of a zeolites material [29]. In this section some kinds of typical zeolites, which relate to this study, will be introduced.

1.2.1 Zeolite A

Zeolite A is a kind of aluminosilicate zeolite, which has the Linde Type A (LTA) framework structure. The synthetic zeolite A has the chemical formula as following:

$$Na_{12}Al_{12}Si_{12}O_{48}.wH_2O \ (w \sim 27)$$

This kind of zeolite A has the Si/Al ratio of 1 and can be called as Na-form. The LTA framework structure is constructed by β-cage as the case of Sodalite (SOD) framework type, which will be shown in the next subsection. In LTA framework structure, β-cages are connected to each other through double 4-membered rings in primitive cubic arrangement, as viewed in Figure 1.1 (a), and producing so-called α-cage at the center, which has the inside diameter of around 11 Å. In a different way, LTA framework structure can also be described by primitive cubic arrangement of α-cage connected through single 8-rings. It has the framework density of 12.9 T-atoms per 1000 $Å^3$. The symmetry group for LTA framework type is $Pm3m$ with lattice constant of 12.3 Å if distinguish the Al and Si atoms. Contrary, the symmetry group will be $Fm\bar{3}c$ and lattice constant of 24.6 Å.

The crystal structure of zeolite A was studied by X-ray diffraction [30], and the results show that there are twelve cations per unit cell of zeolite A. These cations are

distributed at three different cation sites, as seen in Figure 1.1 (b). Eight of them are located at site (1) which near the center of single 6-membered ring window between α-cage and β-cage. Other three of them are located at site (2), the center of 8-membered ring window between adjacent α-cages. And the last one is located at site (3), near the center of single 4-membered ring.

(a)

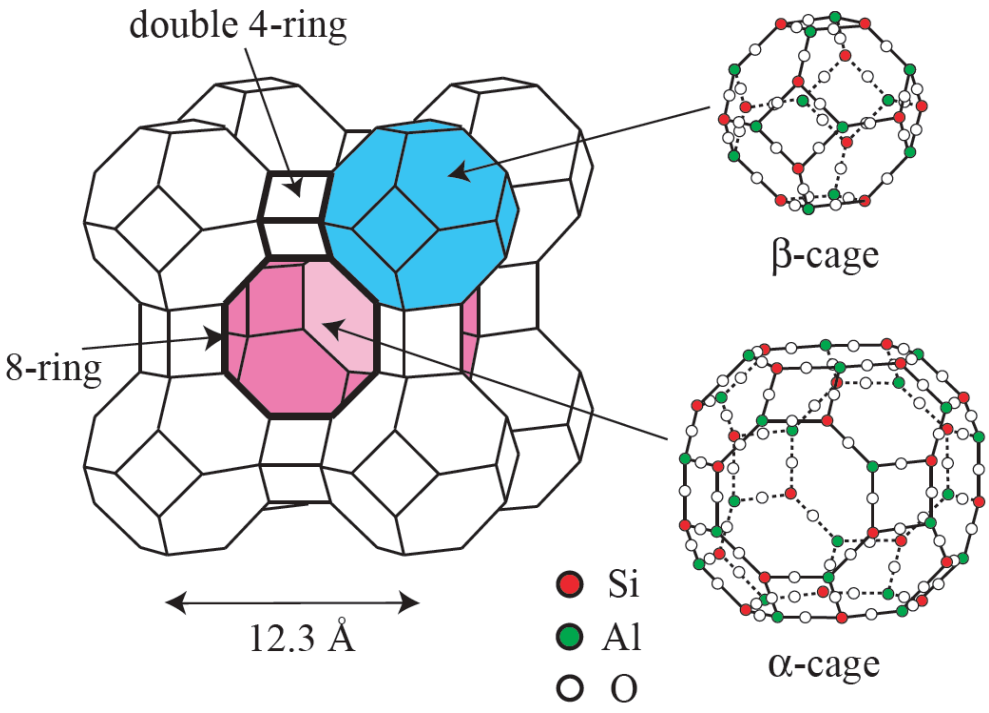

(b)

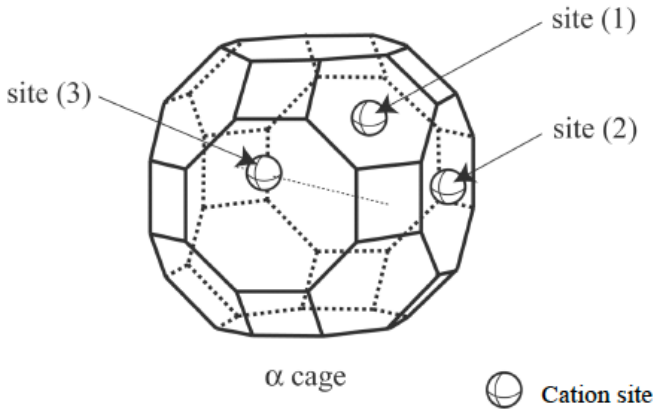

Fig. 1.1. Schematic illustration of the LTA framework structure of zeolite A (a) and typical cation site in α-cage of zeolite A (b).

1.2.2 Sodalite (SOD)

Sodalite is another kind of aluminosilicate zeolite with the SOD framework structure. Sodalite probably has the simplest crystal structure. As seen in Figure 1.2, SOD framework structure consists of a body-centered cubic (bcc) arrangement of β or sodalite cages joined through single 4- and 6-membered rings with the lattice constant of about 9 Å. The β-cage, which shown in Figure 1.2, is a truncated octahedron with 14 faces and 24 vertices. These β-cages can be seen as cubic arrangement, where they connect to each other through 4-rings, and producing another β-cage at the center with inside diameter of ~7 Å. Every β-cages have eight nearest neighbors and six second nearest neighbors, which connected via single 6-membered ring and single 4-membered ring, respectively. Sodalite is also a member of ABC-6 family of zeolites and can be viewed as an ABCABC stacking of hexagonal arrays of single 6-rings in the [111] direction [31]. Similar to all zeolites, sodalite is capable of ion exchange via intercalation. This intercalation occurs through 6-ring windows between any particular β-cage and one of its eight nearest neighbour cages. SOD framework structure has the lattice constant of 8.870 Å and the spacegroup $P4\bar{3}n$ [32]. The framework density, which defined as the number of T-atoms per 1000 Å^3, of SOD structure is 17.2 T-atoms per 1000 Å^3. Because of there are only 6-ring pore openings, sodalite is not called zeolite in strict sense and has very limited sorption capacity.

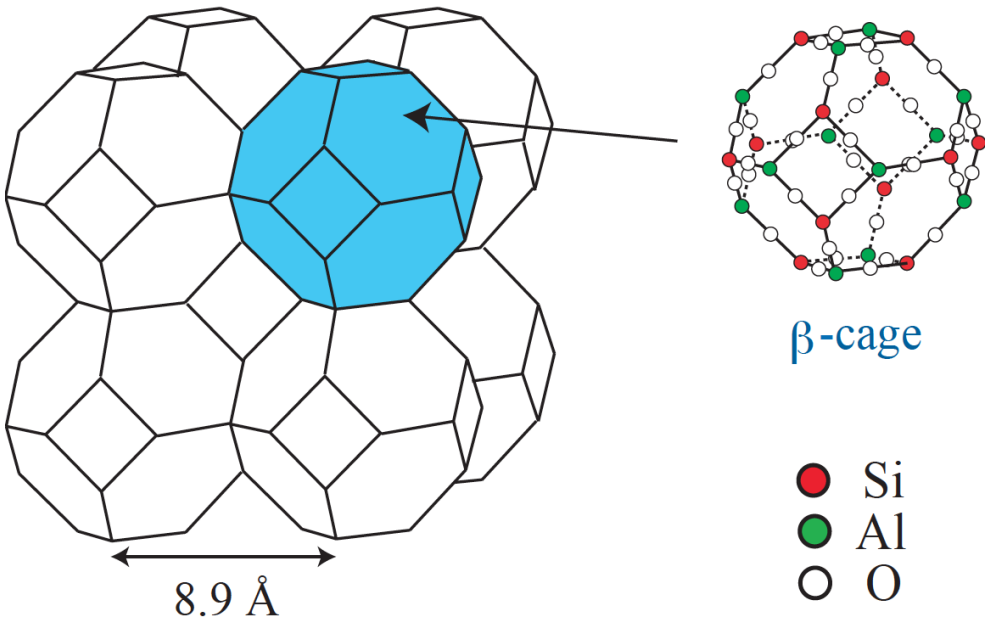

Fig. 1.2. Schematic illustration of the SOD framework structure.

1.2.3 Zeolite X, Y and low-silica X (LSX)

Zeolite X and Y are typical aluminosilicate zeolite with the FAU framework structure. In this structure, supercages and β-cages are arrayed in a double diamond structure with the cage distance of 10.8 Å. FAU framework structure has space group $Fd\bar{3}m$ and lattice constant of about 25 Å. The chemical formula of zeolite X and Y can be given by:

$$M_{8c}Al_{8c}Si_{192-8c}O_{384}.wH_2O$$

This chemical formula expresses that the crystallographic unit cell of zeolite X and Y consists of eight β-cages and eight supercages. If we define the structural unit of β-cage (or supercage), 1/8 of crystallographic unit cell, then the chemical formula will be:

$$M_cAl_cSi_{24-c}O_{48}.wH_2O$$

The Si/Al ((24-c)/c) ratio was usually controlled by the conditions when synthesizing and forming. Zeoiltes with FAU structure are called zeolite X if the Si/Al ratio is lower than 1.5 and are called zeolite Y if the Si/Al ratio is larger than 1.5. In particular, in the case of zeolite X, if the Si/Al ratio is 1, that means c = 12, the name of zeolite changes to zeolite Low Silica X (LSX). This zeolite LSX contains twelve cations in one unit of β-cage (or supercage). The chemical formula of zeolite LSX per β-cage (or supercage) is then given by:

$$M_{12}Al_{12}Si_{12}O_{48}.wH_2O\ (w \sim 30)$$

M_{12} stands for exchangeable extra-framework alkali cations. The framework $Al_{12}Si_{12}O_{48}$ is negatively charged by the number of Al atoms and the neutral charge is compensated by positively charges of M_{12} cations.

The schematic illustration of the FAU framework structure of zeolite LSX and typical cation sites are shown in Figure 1.3. Supercages and β-cages have effective inside diameters of about ≈ 13 and ≈ 7.5 Å, respectively. The β-cages are connected through the double 6-membered rings. Supercages are connected through the 12-membered rings. Each supercage is constructed from four 12-membered rings, four single 6-membered rings and eighteen 4-membered rings. Each supercage is surrounded with four and six β-cages by the sharing of single 6-membered rings and 4-membered rings,

respectively. On the other hands, each β-cage is constructed from eight 6-membered rings and six 4-membered rings, where four of 6-membered rings are shared with supercages via single 6-membered rings and the other four 6-membered rings are connected to neighbor β-cages via double 6-membered rings. The inside diameters of 12-, 6- and 4-membered rings are around ≈ 8, ≈ 2.8 and ≈ 1 Å, respectively. Four 12-membered rings of supercage are widely opened toward neighbor supercages in the T_d symmetry. The inside diameter of 12-membered rings is large enough for moving of guest atoms. Though the inside diameter of single 6-membered ring is narrower than that of 12-membered ring but it allows Na or K cation pass through. The 4-membered ring, however, is too narrow then any cations cannot pass.

In this study, zeolite LSX was used for hosting guest potassium atoms and M^+ are Na^+ and K^+ cations. The chemical formula of used zeolite per β-cage (or supercage), contains $x$$Na^+$ and (12-x)K^+, where x is Na-concentration, will be given as:

$$Na_xK_{12-x}Al_{12}Si_{12}O_{48}.wH_2O \ (w \sim 27)$$

This formula expresses the non-dehydrated zeolite, that means the zeolite still contain water molecules. If we adsorb potassium atoms into zeolite, we need to remove all water molecules out of zeolite in order to avoid the reaction between potassium metal and water. This process is called dehydrated process. After dehydrated process, we obtain the dehydrated zeolite powder and the chemical formula is:

$$Na_xK_{12-x}Al_{12}Si_{12}O_{48}$$

This formula can be abbreviated as Na_xK_{12-x}-LSX hereafter for convenience.

Typical cation sites are also presented in Figure 1.3. Cations are distributed at the center of the hexagonal prism of double 6-membered ring (site I), both sides of double 6-membered ring in β-cage (site I'), near the center of single 6-membered ring in supercage (site II) and at the side of 4-membered ring in supercage (site III') [33]. In dehydrated K_{12}-LSX, K cations occupy site I and I' [34]. Na cations preferably occupy site I' and II without site I in Na-form [35]. In Na-K form, the site I and I' are preferably occupied by Na^+ cations since the close distance to the negative charged framework. In contrast, the site II and III' are preferably occupied by K^+ cations. The occupancy of some cation sites are less than 100% and the final distribution of cations

are determined by the Coulomb interaction with the negatively charged framework as well as other cations.

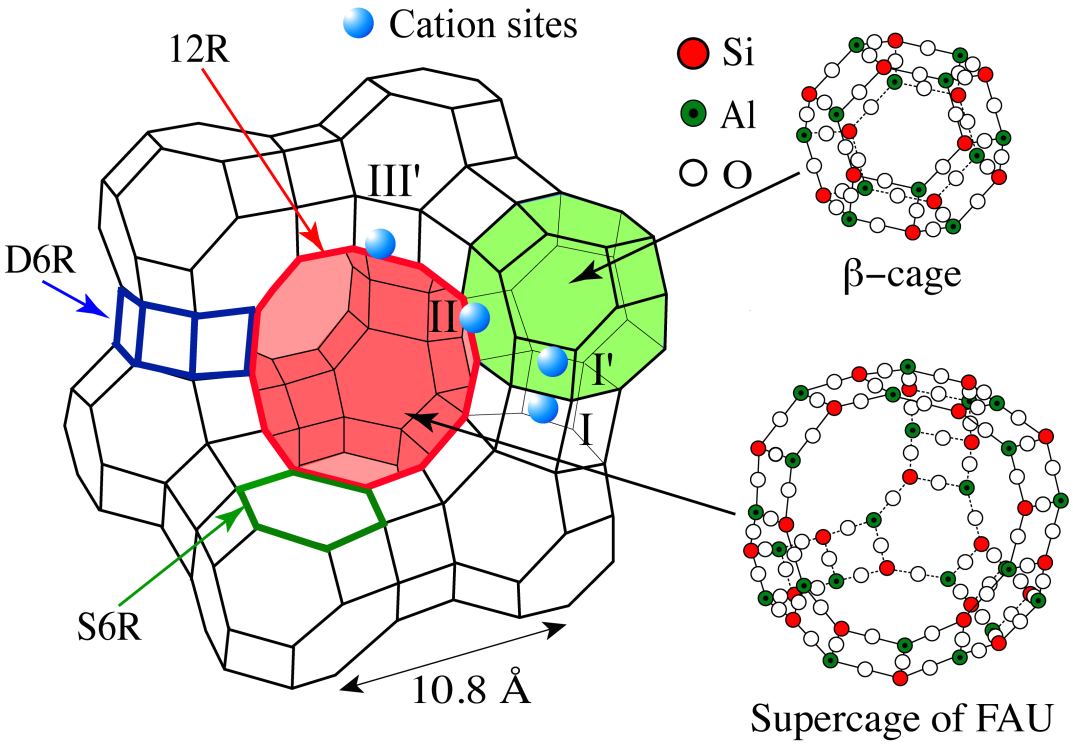

Fig. 1.3. Schematic illustration of the FAU framework structure of zeolite LSX and typical cation sites.

1.2.4 Formation of alkali metal clusters

The electron spin resonance (ESR), optical and neutron powder diffraction measurements have been used to study properties of Na clusters, K clusters and Rb clusters in zeolite Y. In this section an overview of previous studies of alkali metal clusters in zeolite Y, especially the formation of alkali metal clusters in zeolite is given.

The first investigation of alkali metal clusters in zeolite Y was carried out by Kasai and Rabo [47-49]. The dehydrated Na-Y(2.4), where the Na^+ ions occupy cation sites of FAU type framework structure, is a white crystalline powder at normal condition. The factor "2.4" represent the ratio of Si/Al in zeolite framework and this ratio can be varied depending on the sample preparation condition. When the dehydrated Na-

Y(2.4) is exposed to sodium (Na) vapour, it was discovered that that color of powder changes to bright red color. In addition, the ESR measured in this sample show a spectrum with 13 hyperfine components. The changing in color and appearance of hyperfine structures in ESR spectrum are assigned to an electron trapped in supercage. The hyperfine structure observed in the ESR spectrum is consistent with the system, which has hyperfine interaction with four equivalent nuclei possessing nuclear spin of $I = 3/2$, implying the formation of the Na_4^{3+} clusters in supercage. When the exposed Na-Y(2.4) to Na vapour, the situation was described as ionization of Na atom. As a result, the 3s electron of Na atom can be released and shared by four other Na ions, which are tetrahedral distributed in β-cage, through single 6-membered ring. However the information of detailed distribution of Na ions has not been well determined [49].

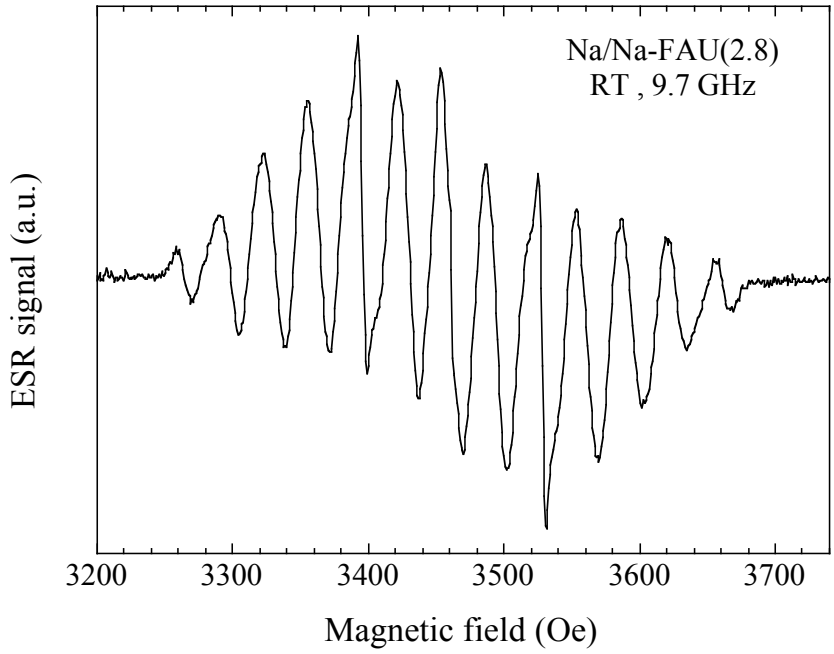

Fig. 1.4. ESR spectrum of Na-loaded Na-Y(2.8) at loading density less than 0.01 measured at rom temperature [50].

An ESR spectrum of sample Na-loaded Na-Y(2.8) with loading density less than 0.01, which is measured by Ikemoto and co-worker, is displayed in Fig. 1.4. As shown in this figure, the hyperfine structure consisting of 13 components are observed. This appearance of 13 lines hyperfine structure suggests the formation of Na_4^{3+} paramagnetic clusters with tetrahedral symmetry in β-cage [50]. The optical

absorption spectrum of Na-loaded Na-Y(2.8) at dilute loading density, which is plotted in Fig. 1.5, obviously exhibit a absorption band at ≈ 2.5 eV. If we assume a spherical well potential to confine the electron in β-cage, the optical excitation energy between 1s- and 1p-quantum states is coincident with the absorption band in absorption spectrum [50]. On the other hand, in other studies on sodium vapour with synthetic Sodalite, a changing in color of sample powder as well as the similar 13 lines hyperfine structure in ESR spectrum are also revealed [51-52]. In the case of Sodalite, the Na_4^{3+} clusters are formed in β-cage.

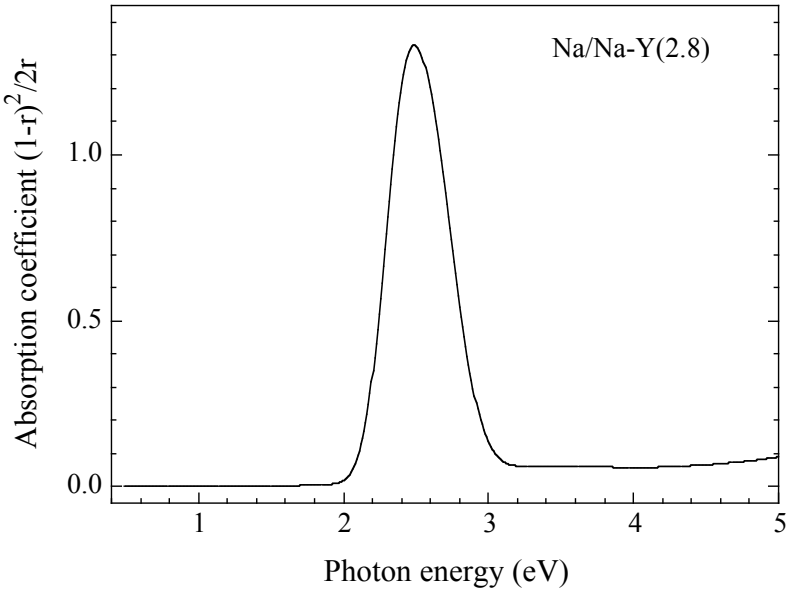

Fig. 1.5. Optical absorption spectrum of Na-loaded Na-Y(2.8) at dilute loading density measured at rom temperature [50].

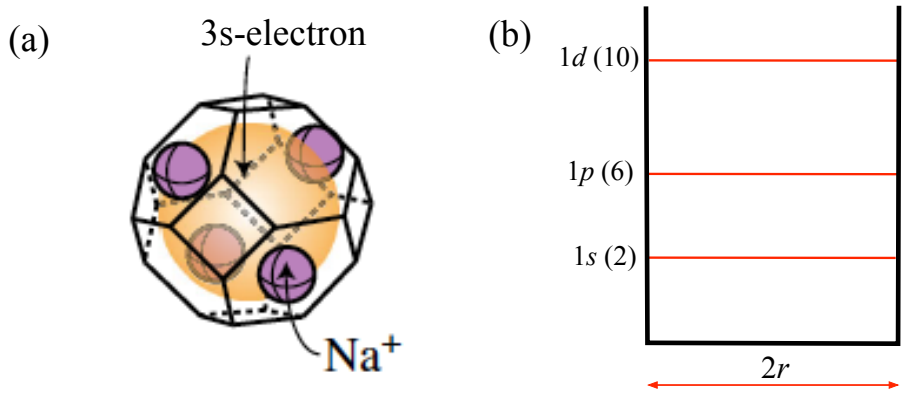

Fig. 1.6. Illustration of Na_4^{3+} cluster (a) and spherical well potential with inner diameter $2r$ and quantum states $1s$, $1p$, $1d$ (b).

These above results clearly point out that the paramagnetic Na_4^{3+} clusters are successively formed in β-cage by introducing Na atoms in to zeolite Y. The 3s-electron of Na atom is shared by four Na^+ cations, which distributed in β-cage. This 3s-electron is assumed to be quantum confined in a spherical potential. The illustration of formation of Na_4^{3+} clusters in zeolite Y and spherical well potential are plotted in Fig 1.6 (a) and (b), respectively.

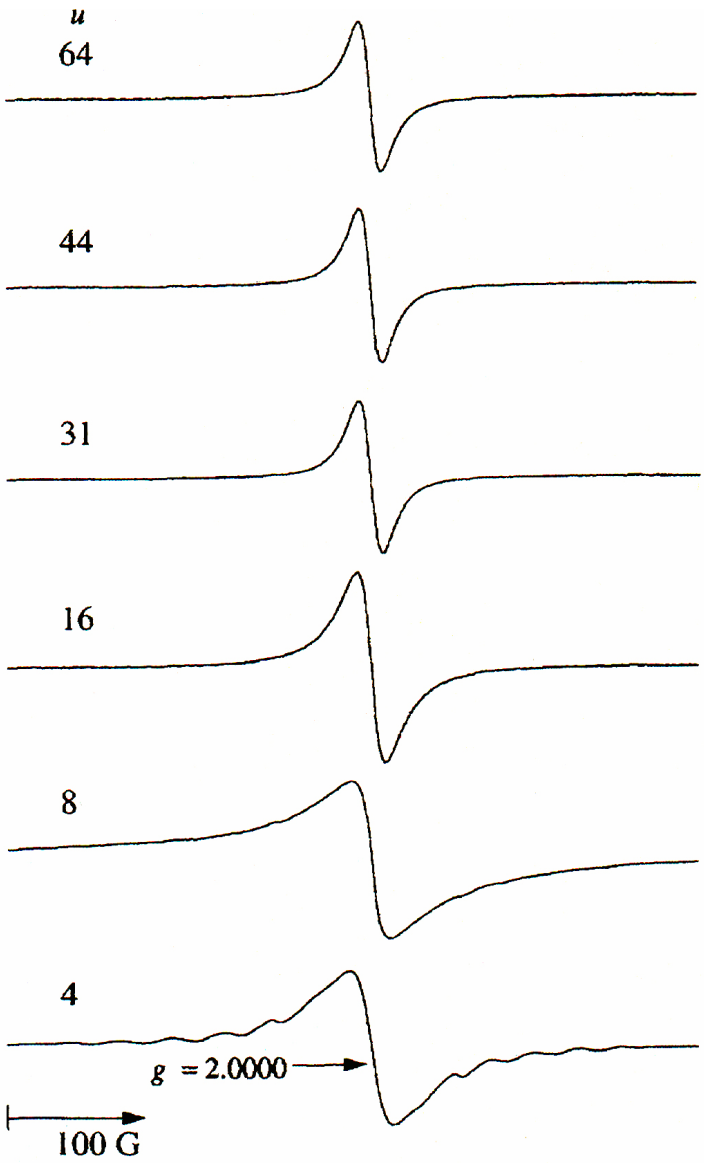

Fig. 1.7. ESR spectra of Na_u/Na_{56}-Y(2.4) measured at room temperature for various value of u [54].

Further studies of Na clusters in zeolite Y have been carried out in Na loaded Na_{56}-Y(2.4) [53-54]. The neutron powder diffraction was used to investigate this sample.

The data of from neutron powder diffraction measurements were refined by Rietveld method. The results show that there is a slight reduction of the occupancy observed at the site II. In addition, the occupancy at the site I exhibit remarkable dropping, while that at site I' increases significantly. This may be assigned to the movement of the Na cations from supercage to β-cage through single 6-membered rings and forming the Na_4^{3+} clusters in β-cage [53].

The results for ESR measurements of Na_u/Na_{56}-Y(2.4) measured at room temperature for various value of u is plotted in Fig. 1.7. At u = 4, the ESR spectrum shows a 13 lines structure of Na_4^{3+} paramagnetic clusters. With increasing u, u > 4, the ESR spectra shows singlet resonance. These ESR spectra eventually originate from the interaction of unpaired electron in neighbor Na_4^{3+} clusters. If the distances between neighbors Na_4^{3+} clusters are small enough, the wave function of these clusters may overlap each other and results to the quantum mechanical exchange interaction [54].

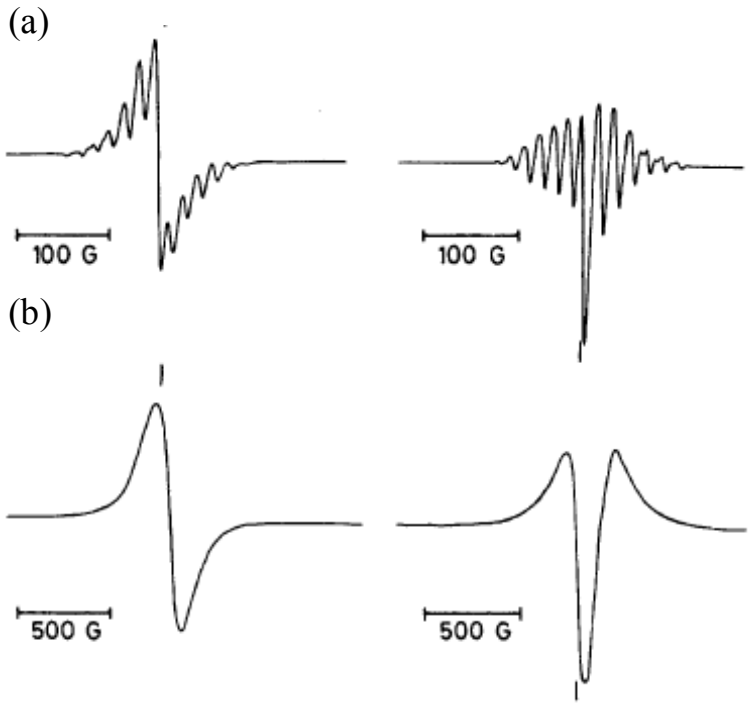

Fig. 1.8. ESR spectra of K cluster in K-Y (a) and Rb metallic cluster in Rb-Y (b) measured at 120 K, the first and second derivative are displayed at the left and right, respectively [55].

Beside of Na cluster, the K cluster and Rb cluster incorporated in zeolite Y were also investigated. Figure 1.8 displays the first and second derivative ESR spectra of K clusters in K-Y and Rb metallic cluster at 120 K. A structure with 13 components is observed in the ESR spectra of K-Y after expose to K vapour. This structure is assigned to the formation of K_4^{3+} clusters in β-cage of zeolite Y, similarly with that of Na_4^{3+} clusters. However there is no evidence of Rb_4^{3+} clusters form in Rb-Y. The Rb_4^{3+} clusters may be intrinsically unstable to generate in Rb-Y. The larger size of Rb atoms is also considered as a reason why the Rb_4^{3+} clusters have not been observed [55].

1.2.5 Formation of alkali metal cluster in zeolite LSX

The framework of zeolite consists of aluminum, silicon and oxygen atoms. These atoms bonded to each other by covalent bonds and created a negative charge framework. This negative charge is normally compensated by cations, which form an extra-framework with no covalent bond. These cations are attracted by negative charge framework and repulsed by their own positive charge. There is an unusually strong net electronic field must exists surround the extra-framework [36]. If alkali metal atoms are introduced there, they will be ionized by this electrostatic field and then release the s-electrons. The s-electron is attracted by extra-framework and repelled by framework simultaneously, since the positive charge of extra-framework the negative charge of framework. If the wave functions of s-electrons of alkali metal overlap each other, the cationic alkali metal cluster can be generated in cages of zeolites. In this study, we loaded potassium atoms into zeolite LSX, which has chemical formula $Na_xK_{12-x}Al_{12}Si_{12}O_{48}$. The extra-framework contains both of Na^+ and K^+ cation. The distribution of these cations was mentioned above. When guest K atoms are introduced into zeolite LSX, the Na-K alloy clusters can be generated in supercages and/or β-cages. The chemical formula of zeolite LSX with loaded K atoms is given by $Na_xK_{12-x+n}Al_{12}Si_{12}O_{48}$, and then can be abbreviated as K_n/Na_xK_{12-x}-LSX, where n is the K-loading density. The schematic illustration for the formation of alkali metal cluster in zeolite LSX is shown in Figure 1.9. According to the structure of zeolite LSX, we can expect the interaction of s-electrons in supercages and β-cages through single 6-membered ring as well as between adjacent supercages via 12-

membered ring. The interaction of s-electrons in adjacent *β*-cages, however, is very rare because adjacent *β*-cages are well separated by double 6-membered ring.

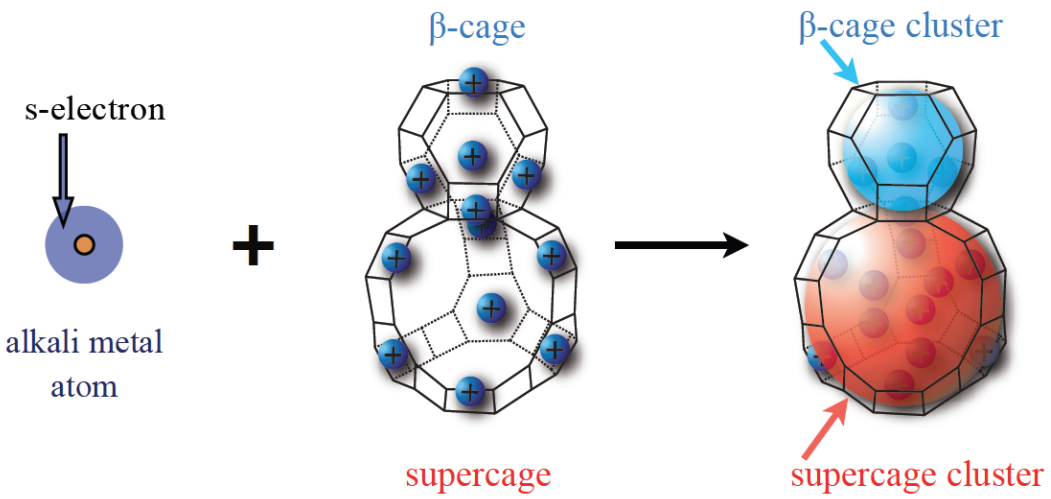

Fig. 1.9. Schematic illustration of the formation of alkali metal clusters in zeolite LSX.

The s-electrons of guest alkali atoms are confined in a spherical well potential. This spherical well potential originates from the combination of attractive force of extra-framework and repulsion force of the framework. According to the model of electronic shell structure, s-electrons of cluster can occupy the primitive quantum state 1*s*, 1*p*, 1*d*, etc…with the degeneracy are 2, 6, 10, respectively. By loading guest alkali atoms, the first two s-electrons may occupy 1*s* state, the next six s-electrons then occupy 1*p*-state and so on. The overlapping of wave function of these s-electrons between adjacent cages in zeolites lead to the formation of arrayed alkali metal clusters in zeolites. Hence, macro phenomenon such as magnetic ordering, insulator-metal transition…can be expected to be observed. The schematic illustration of spherical well potential and overlapping of wave function of s-electrons between adjacent cages is described in Figure 1.10. The energy difference between quantum states is estimated by considering the quantum energy levels, which obtained by solving Schrodinger equation in case of spherical well potential. This energy difference depends on the inside diameter of cages. In the case of zeolite LSX, the effective inside diameter of supercages and *β*-cages are 13 and 7.5 Å, respectively. If we assume the spherical potential, the kinetic energies of a free electron at 1s-state in supercage and *β*-cage clusters are 0.9 and 2.7 eV. On the other hands, the respective kinetic energy of a free electron at 1*p* state in supercage and *β*-cage clusters are 1.8

and 5.5 eV. Therefore, the excitation energies from 1s- to 1p-state of s-electron in supercage and β-cage clusters can be determined are 0.9 and 2.8 eV, respectively. According to the crystal structure of zeolite LSX, the overlapping of wavefunction of s-electron, which confined in adjacent clusters, can be expected between adjacent supercage clusters through large 12-membered ring or between supercage clusters and β-cage clusters via single 6-membered ring. However neighbor β-cage clusters do not have the overlapping due to high barrier potential, which is caused by double 6-membered ring.

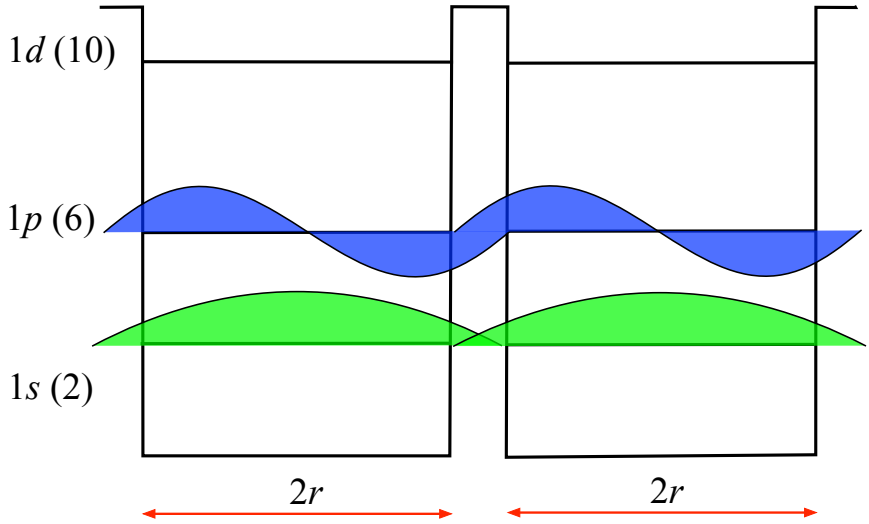

Fig. 1.10. Schematic diagram of spherical well potential with quantum states 1*s*, 1*p*, 1*d* and overlapping of wavefunction of s-electrons between adjacent cages, where 2*r* is inside diameter of cage.

1.3 Alkali metal clusters in zeolites

1.3.1 Alkali metal clusters in zeolite A

Physical properties, such as optical properties and magnetic properites, of K clusters and Rb clusters incorporated in zeolite A have been investigated. The K clusters and Rb clusters are generated into zeolite A by loading of guest K- and Rb atoms, respectively. The ferromagnetism, which is originated from the canting of antiferromagnetically ordered magnetic moments of K clusters in zeolite A, has been found. In the meanwhile, Rb clusters in zeolite A also exhibit spontaneous magnetization. This spontaneous magnetization has been proposed to cause by a model of spin-cant or ferrimagnetism. An overview of previous studies on alkali metal clusters in zeolite A will be described in this section.

A. K clusters in zeolite A

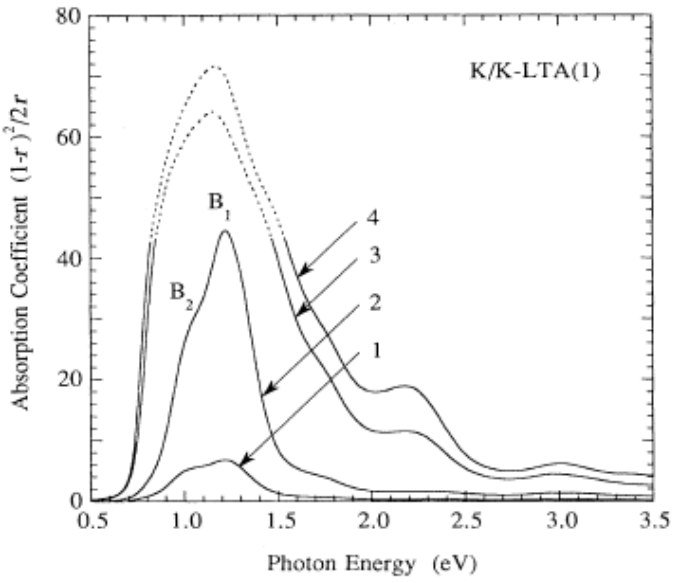

Fig. 1.11. Absorption spectra of dilutely K/K-LTA(1) at room temperature [37].

By loading K metal into K-form zeolite A, 4s electrons of K atoms can be shared by several K^+ cations in α-cage and repulsed by the negatively charged framework. As a result, K clusters are generated in K loaded into K form zeolite A, which is denoted as K/K-LTA(1). Various K loading densities n samples, from dilute $n \sim 0$ to saturated n

~ 7.2, were prepared by adjusting the amount of K metal. Absorption spectra of dilutely K loaded K-LTA(1) at room temperature is shown in Figure 1.11. The K density increases in the order of curves 1-4. Absorption bands are obtained at 1.0, 1.22, 1.75, 2.25 and 3.0 eV. In curves 1 and 2, significant strong absorption bands appear in the infrared region 1.22 eV and there is no absorption at visible and ultra-violet regions. This phenomenon is quite different when compared with that of K atom or bulk K metal. The band at 1.22 eV can be assigned to the excitation of electron between 1*s* and 1*p* state of K clusters formed in the α-cage.

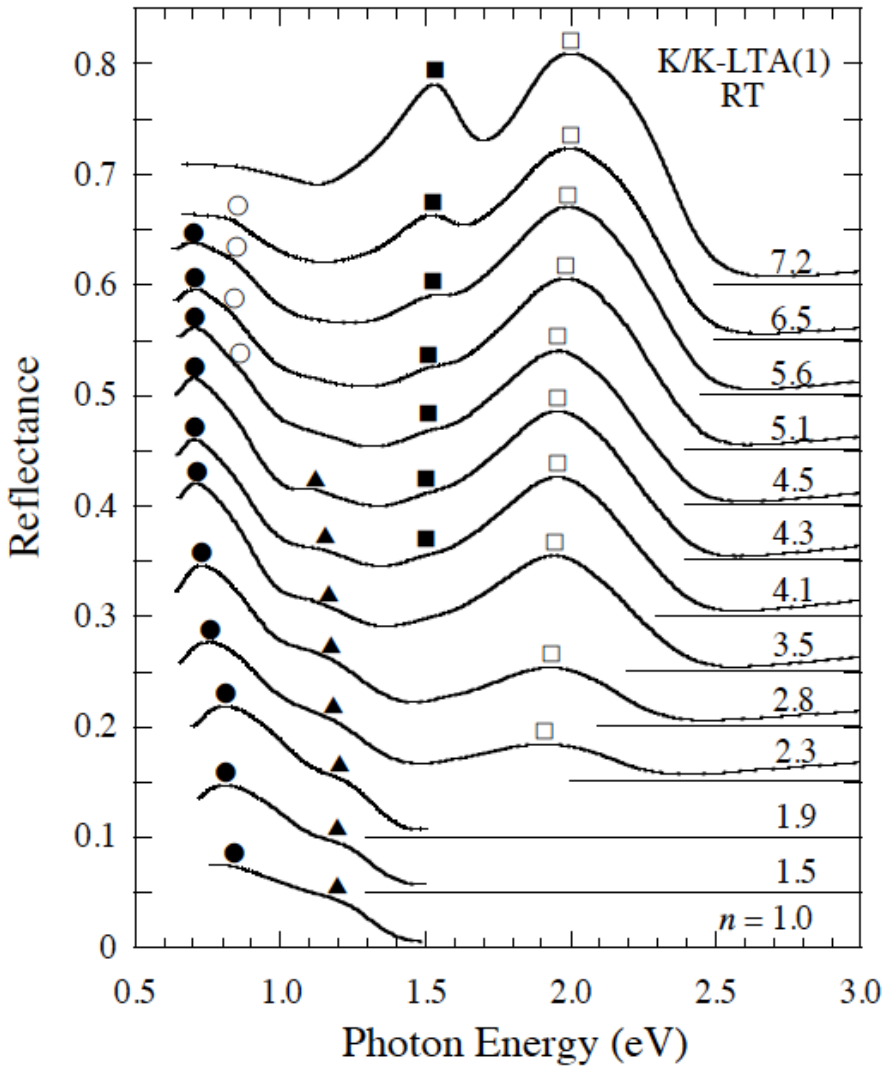

Fig. 1.12. Reflection spectra of K/K-LTA(1) at various loading densities at room temperature [38].

Reflection spectra of K/K-LTA(1) at various loading densities are presented in Figure 1.12. As seen in the figure, reflection bands at 1.5 and 2.0 eV appear at $n > 2$ with increase loading density. These bands are explained by the 1*p*-1*d* transition of K cluster. The reflection band at 2.0 eV is assigned to the surface plasmon-like exicitation, which is the collective motion of electrons confined in clusters. These above results clearly show that 4s electrons successfully occupy 1s and 1p state of K cluster in zeolite A [11]. Further analysis of optical spectra indicated that these samples are Mott-Hubbard type insulator.

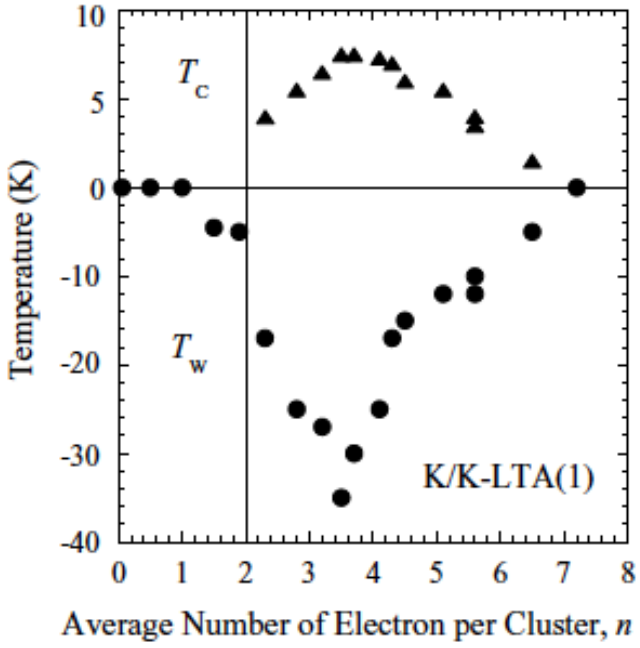

Fig. 1.13. K loading density n dependence of the Curie temperature (T_C) and the Weiss temperature (T_W) for K/K-LTA(1) [11].

In terms of magnetic properties, the spontaneous magnetization has been observed for samples at $2 < n < 6.4$ at low temperature for K/K-LTA(1). The temperature dependence of magnetization curves in these samples resembles ferromagnetic properties. The values of Curie temperature and Weiss temperature are shown in Figure 1.13 as K loading density n dependence. At $n \leq 2$, there is no magnetic ordering observed with temperature down to 1.8 K. At $n > 2$, spontaneous magnetization suddenly appears. Curie temperature increases and shows finite value. At the same time Weiss temperature decreases and has negative value. The n dependence of Curie and Weiss temperature shows the maximum and minimum at 7.5

and -35 K, respectively. At saturated samples, n = 7.2, both of Curie and Weiss temperature approach to 0 K. The negative values of Weiss temperature for samples, where observed spontaneous magnetization, imply the antiferromagnetic coupling between magnetic moments. That means spontaneous magnetization coexist with the antiferromagnetic coupling. Hence, ferromagnetic properties at low temperatures of K/K-LTA(1) might be not assigned to an ordinary ferromagnetism [11].

There are two possible model to explain the coexistence of spontaneous magnetization and antiferromagnetic coupling in K/K-LTA(1). The first one is the ferrimagnetism, where the spontaneous magnetization is realized by antiferromagnetic ordering of two (or more) different magnetic sublattices. However, this model could not well explain the value of spontaneous magnetization and its continuous increase with K loading density [39-40]. Moreover, the spin-flop behavior characteristic of ferrimagnetism is not observed in the magnetization up to 52 T [41]. Hence the model of ferrimagnetism is not applicable to the origin of magnetic properties in K/K-LTA(1). The second model, which is the most plausible to origin of spontaneous magnetization in K/K-LTA(1), is a weak ferromagnetism due to the canting of antiferromagnetically ordered magnetic moments. A simple illustration of spin-cant model is shown in Figure 1.14, the interaction between magnetic moment is provided via the asymmetric exchange interaction (Dzyaloshinsky-Moriya (DM) interaction) [42-44]. The DM interaction is given by the second-order perturbation through the spin orbit interaction in the case of non-degenerated states. Therefore the DM interaction is normally weaker than the isotropic exchange interaction. The DM interaction with small canting angle θ will generate small spontaneous magnetization. However K/K-LTA(1) shown larger spontaneous magnetization, about 30% of the localized magnetic moment at the maximum. An anomalously strong DM interaction is considered in order to explain such larger spontaneous mangetization. According to the theory by Tachiki [45], the DM interaction can be strongly enhanced by the orbital degeneracy up to the value comparable to the isotropic exchange interaction. In K clusters, the orbital degeneracy of the 1p state is realized at low temperature in the ferromagnetic samples with $2 < n < 6$. Hence, the degeneracy may be the origin of the strong DM interaction resulting in the large spontaneous magnetization in K/K-LTA(1). In the saturated sample, n = 7.2, about 70 % of α-cages are occupied by the magnetic moments with the spin quantum number s = 1/2 [39]. It is quite strange that

the magnetic interaction between magnetic moments vanishes, though the value of 75 % exceeds the percolation permit of a simple cubic lattice. In this sample, the orbital degeneracy is though to be quenched. There are seven *s* electrons in a K clusters, a hole state then is generated in 1*p* state. Of the non-degenerate hole orbitals of adjacent clusters are orthogonalized with each other, the exchange interaction between the holes in adjacent clusters may disappear. Hence the paramagnetic properties in this sample can be explained.

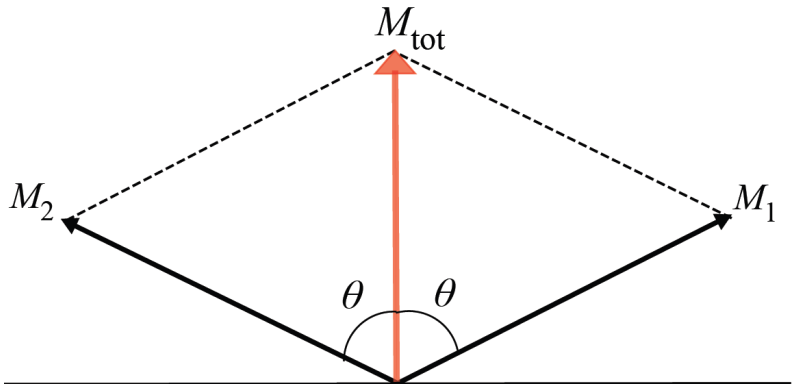

Fig. 1.14. Schematic illustration of a simple spin-cant model.

B. Rb clusters in zeolite A

Rb cluster has also been generated in zeolite A by adsorbing Rb metal into Rb-form of zeolite A. The name of Rb loaded Rb-form of zeolite A is given by Rb/Rb-LTA. Optical and magnetic properties for various Rb loading densities were investigated. Figure 1.15 displays the optical absorption spectra of Rb/Rb-LTA at dilute loading density. Dilute sample of K/K-LTA is also plotted together for comparison. The absorption spectrum of Rb/Rb-LTA shows clearly a strong absorption band at around 1.1 eV, similar to that of K/K-LTA. This strong absorption band can be assigned to the excitation of s electrons from 1*s* to 1*p* state in Rb clusters in zeolite A. The 5s electrons of the guest Rb atoms are shared by several Rb^+ cations in the α-cage and form Rb cluster there [14]. The absorption band in Rb/Rb-LTA does not split into doublet structure as observed in K/K-LTA(1), which is assigned to a band effect under the assumption of metallic phase [10].

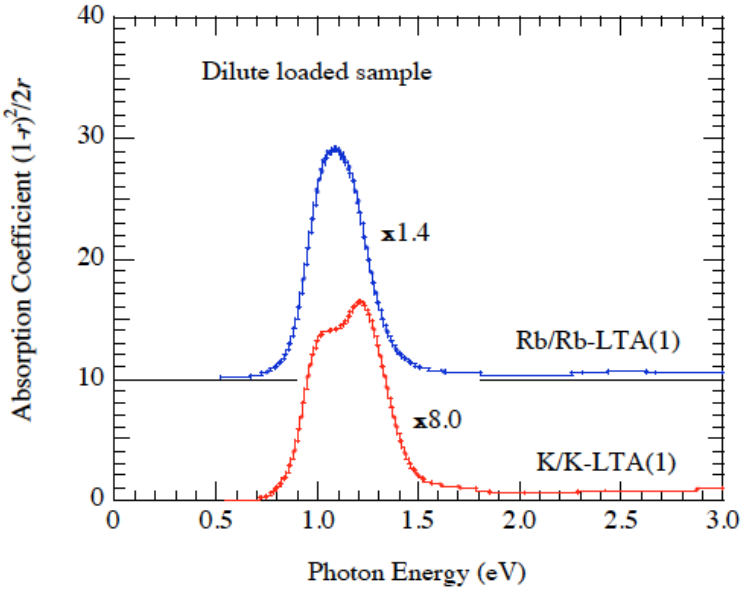

Fig. 1.15. The optical absorption spectra of Rb and K clusters in zeolite A at dilute loading density [14].

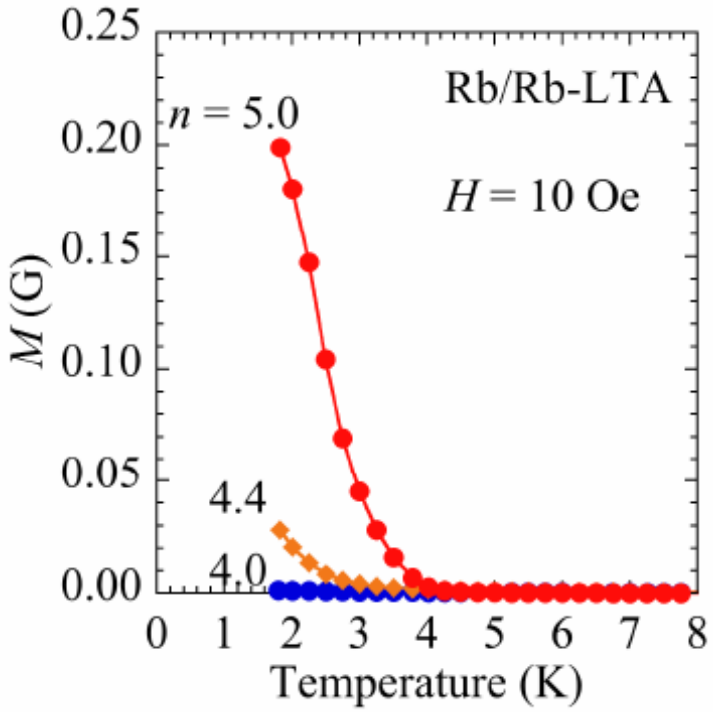

Fig. 1.16. The temperature dependence of magnetization of Rb/Rb-LTA measured under 10 Oe at loading densities n = 4.0, 4.4 and 5.0 [14].

Rb clusters in zeolite A exhibit ferromagnetic properties. Figure 1.16 displays the temperature dependence of magnetization for Rb/Rb-LTA measured at 10 Oe at three different Rb loading densities, n = 4.0, 4.4 and 5.0. At n = 4.0, the sample is paramagnetic and shows a Curie-Weiss temperature between 1.8 K and room temperature. At n = 4.4 and 5.0, magnetization suddenly increases below about 2.4 and 3.8 K, respectively. These results imply ferromagnetic ordering of Rb cluster in zeolite A. At n = 5.0, large value of the Curie constant is obtained and the magnetic moments occupy 108% of cages if we assume magnetic moment with s = 1/2. That means some clusters may be generated in β-cage. At higher temperature, samples at n = 4.4 and 5.0 show Curie-Weiss behavior with negative values of Weiss temperature. The negative value can be assigned to the antifferomagnetic interaction between magnetic moments of Rb/Rb-LTA. Therefore, the ferromagnetic property of Rb cluster in zeolite A may not be assigned to ordinary ferromagnetism. In order to understand the spontaneous magnetization with antiferromagnetic coupling in Rb/Rb-LTA, two possible models are consider. One is the spin-canting antiferromagnetic with orbital degeneracy of 1p-state of cluster, as similar observed in K/K-LTA(1) [11]. The other one is a ferrimagnetism. In the case of Rb cluster, ferromagnetic properties are observed only at n > 4. Hence the loading density dependence of magnetic properties is thought to different with that of K cluster. The degeneracy of the 1p-state may not play an essential role in Rb cluster. The large value of the Curie constant may support the two magnetic sublattices of the ferrimagnetism. On the other hand, the Rb cluster in zeolite A shows strong absorption coefficient at mid-infrared region [15], which might be due to the Drude term. The Rb clusters in zeolite LTA is then possibly in metallic state. If the itinerant-electron ferromagnetic realized in Rb cluster in α-cages and it couples antiferromagnetically with localized magnetic moments of Rb cluster in β-cages, a ferrimagnetic ordering can be realized [13].

1.3.2 Alkali metal clusters in Sodalite (SOD)

The formation of Na_4^{3+} clusters in sodalite (SOD) is generated by loading of guest Na atoms. The measurements in nuclear magnetic resonance and neutron diffraction reveal the antiferromagnetic ordering of magnetic moments, which is localized in Na_4^{3+} clusters in sodalite cage (β-cage) of SOD.

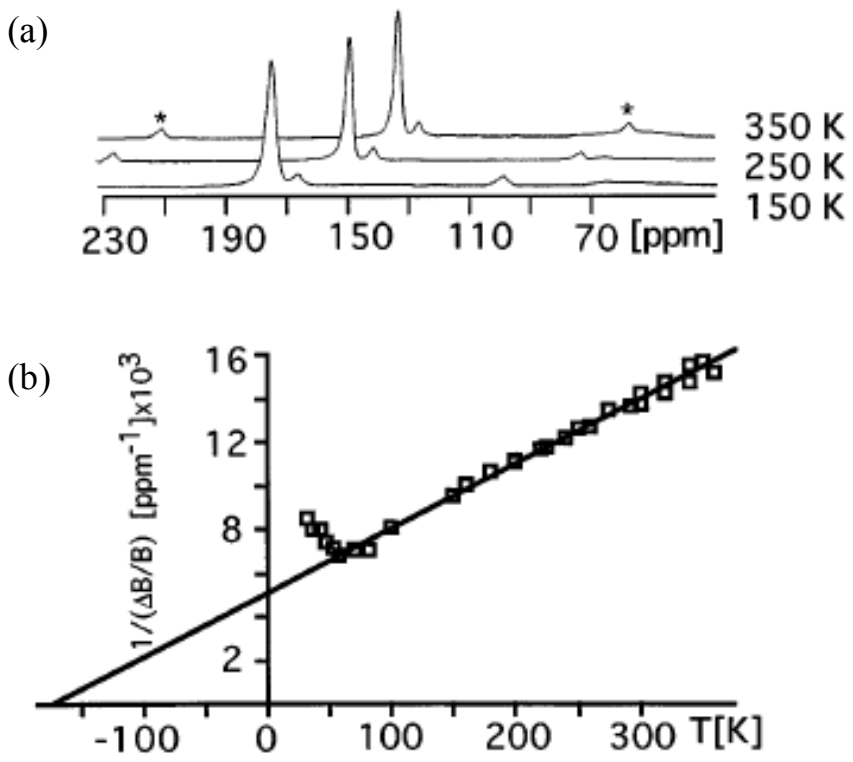

Fig. 1.17. The ^{27}Al magic angle spinning nuclear magnetic resonance (MAG NMR) measured for Na-SOD at selected temperature (a) and the temperature dependence of inverse paramagnetic shift of the main ^{27}Al resonance in Na-SOD (b) [16].

The magnetic properties of alkali metal cluster in Sodalite (SOD) have been received much attraction. In 1998, Srdanov *et al*., perform the investigation on Na_4^{3+} clusters incorporated in SOD [16]. The nuclear magnetic resonance (NMR), electron paramagnetic resonance (EPR) and the magnetic susceptibility measurements were carried out. The Na_4^{3+} clusters are generated in almost all of β-cage of SOD, where the clusters are arranged in a body centered cubic structure. The authors explored the evidence for the antiferromagnetic properties of Na_4^{3+} clusters in Na-SOD.

The paramagnetic shift of ^{27}Al NMR resonance was observed in the NMR spectra of Na-SOD. As seen in Fig. 1.17 (a), this shift increases with decreasing temperature down to 50 K. This result suggests some changes in electronic structure, which is may caused by magnetic phase transition. In addition, the temperature dependence of reciprocal of paramagnetic shift is fitted with the Curie - Weiss law. The result of fitting is shown in Fig. 1.17 (b). The estimated value of Weiss temperature is – 178 ±

8 K. This obviously indicates a strong antiferromagnetic exchange interaction in the paramagnetic phase. On the other hand, the EPR spectra of Na-SOD, which is displayed in Fig. 1.18 (a), exhibit an absence of the Na_4^{3+} hyperfine structure. The peak of Na clusters suppress below 50 K, as seen in the EPR spectra. Fig. 1.18 (b) plots the temperature dependence of magnetic susceptibility for Na-SOD. The data indicates the Pauli-like magnetic susceptibility. An expanded display of magnetic susceptibility behavior at the temperature range between 40 and 90 K is shown in the inset figure of Fig. 1.18 (b). The maximum in the magnetic susceptibility is observed at 55 ± 2 K. The Néel temperature is determined to be 48 ± 2 K.

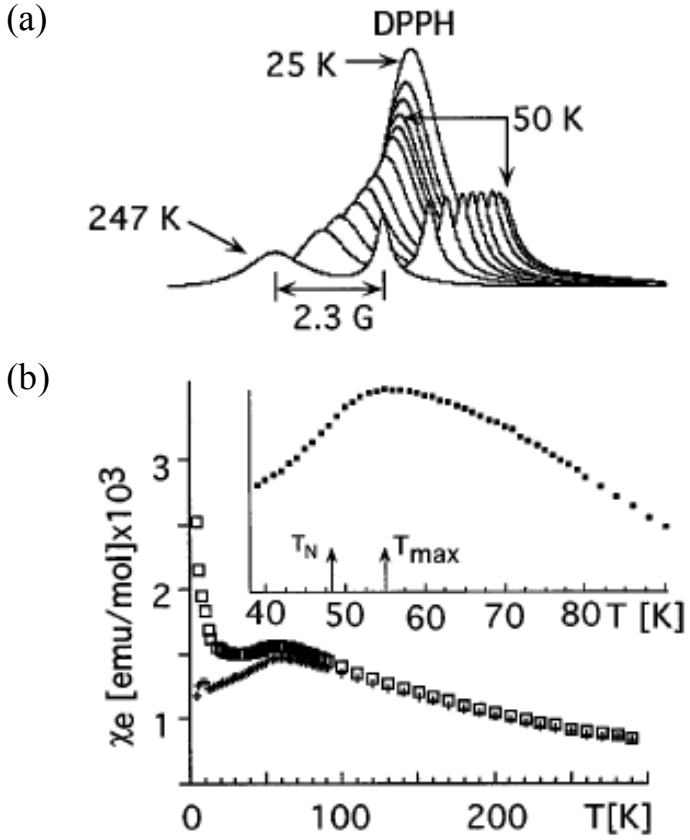

Fig. 1.18. EPR spectra of Na-SOD measure at various temperatures, the EPR spectra of DPPH (paramagnetic solid used as an EPR frequency standard) are also compared (a) and the temperature dependence of magnetic susceptibility for Na-SOD, the inset figure shows an extended plot at low temperature region (b) [16].

These above results have been considered as the evidence for the antiferromagnetic ordering of Na_4^{3+} clusters, which consists of unpaired electrons, below 48 K. The antiferromagnetic properties are realized in Mott insulating state. The electron spin density put Na-SOD near the metal – insulator transition, however no sign of metallic property at room temperature due to the existence of optical gap [46] and no dc conductivity in Na-SOD.

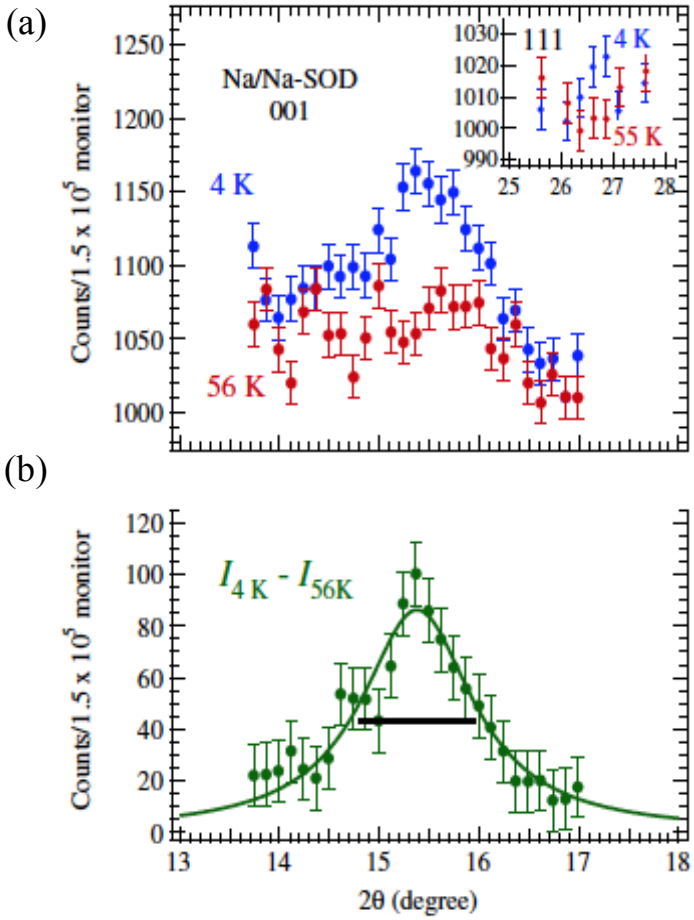

Fig. 1.19. Neutron diffraction at the scattering angle around the 001 reflection collected at 4 K and 56 K for Na/Na-SOD (a) and the difference, $I_{4K} - I_{56K}$, between the data at 4 K and 56 K (b) [17].

Another detailed investigation for magnetic structure as well as the shape of the s-electron wave function in Na clusters in SOD by using neutron diffraction was carried out by Nakano *et al*,. [17]. The authors directly observed the long range magnetic ordering of s-electrons in Na/Na-SOD. The magnetic susceptibility measurements

reveal to reproduce the behavior of temperature dependence as report previously. The neutron diffraction pattern collected at scattering angle around 001 reflection are perform at the temperature of 4 K and 56 K, below and above the Néel temperature, respectively. The results of this measurement are shown in Fig. 1.14, where the neutron diffraction data measured at 4 K and 56 K and differences between them are plotted in Fig. 1.19 (a) and (b), respectively. At low temperature, the 001 reflection is obviously seen. In addition the temperature dependence of the total count of scattered neutrons are also evaluated. As shown in Fig. 1.20, at higher temperature region, the count is nearly constant. However, below 50 K, a suddenly increasing of the count is observed. This results consistent with the value of Néel temperature. A calculation of phenomenological equation is also performed in order to compare with experimental results. The solid curve in Fig. 1.20 show clearly fit between the results observed in experimental and calculation. These results strongly point out that the 001 peak, which was observed at low temperature, comes from the magnetic reflection of antiferromagnetic ordering of s-electrons in β-cage Na clusters.

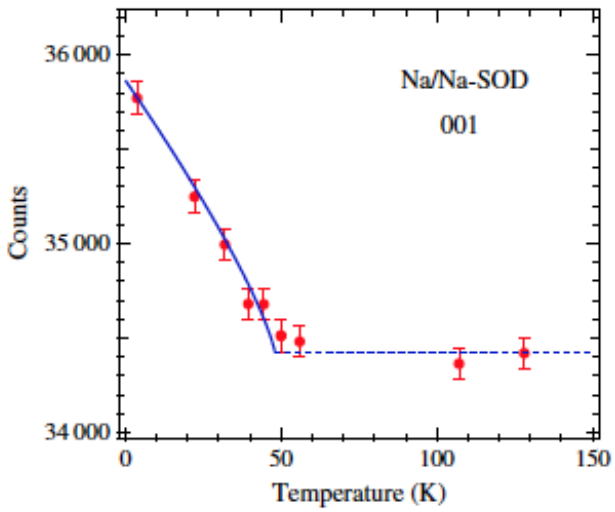

Fig. 1.20. Integrated intensity of the 001 peak plotted as a temperature dependence for Na/Na-SOD [17].

1.3.3 Alkali metal clusters in zeolite X

Zeolite X has the Si/Al ratio smaller than 1.5. That means the number of cations distributed in zeolite framework is larger when compare with that of zeolite Y. It is expected that the alkali metal cluster in zeolite X will show different properties with

clusters in zeolite Y. Some results and discussion in previous investigation of alkali metal clusters in zeolite X will be shown in this section.

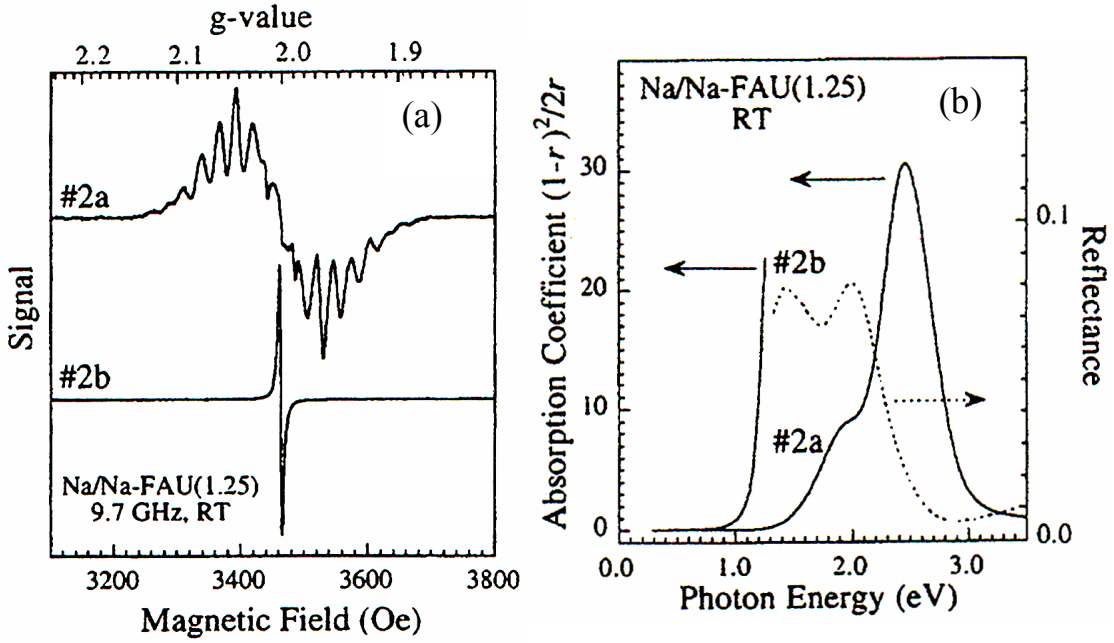

Fig. 1.21. ESR spectra (a) and optical absorption spectra (b) of Na-loaded Na-X(1.25) measured at room temperature for samples with loading densities ~ 0.01 (#2a) and ~ 3 (#2b) [50].

Ikemoto and co-worker have investigated the ESR and optical properties of Na-loaded to Na-X(1.25). The results of ESR and optical absorption measurements are displayed in Fig. 1.21. As seen in Fig. 1.21 (a), ESR signal of the sample #2a, dilute sample, exhibits a hyperfine structure consisting 16 components, which can be explained by assuming Na_5^{4+} clusters. In addition the ESR signal analysis imply that the spectra contain a few percent of 10 lines hyperfine structure with a period of 20 Oe, which is attributed to Na_3^{2+} clusters. The period of 20 Oe is smaller than that of period of 27 Oe observed in 16 lines hyperfine structure. In other words, the electron wave function of Na_3^{2+} is larger than that of Na_5^{4+}. Leading to the understanding that Na_3^{2+} clusters are located in supercage but not β-cage in zeolite X. With increasing loading density, in the sample #2b, the ESR spectrum become narrowing. The optical absorption spectrum of sample #2a show remarkable absorption bands at ≈1.9 eV and ≈ 2.5 eV, whose can be explained by the excitation of s-electrons confined in supercage and β-cage clusters, namely in Na_3^{2+} and Na_5^{4+} clusters respectively. The

Na_3^{2+} cluster has lower excitation energy because larger size of supercage while Na_5^{4+} cluster has higher excitation energy due to smaller size of β-cage. At higher Na-loaded sample #2b, the refelection bands at lower energy < 2 eV (dotted line) can be assigned to originate from excitation of s-electrons confined in supercage. Both of these samples may be in insulating state since the absence of Drude-like absorption at lower energy region.

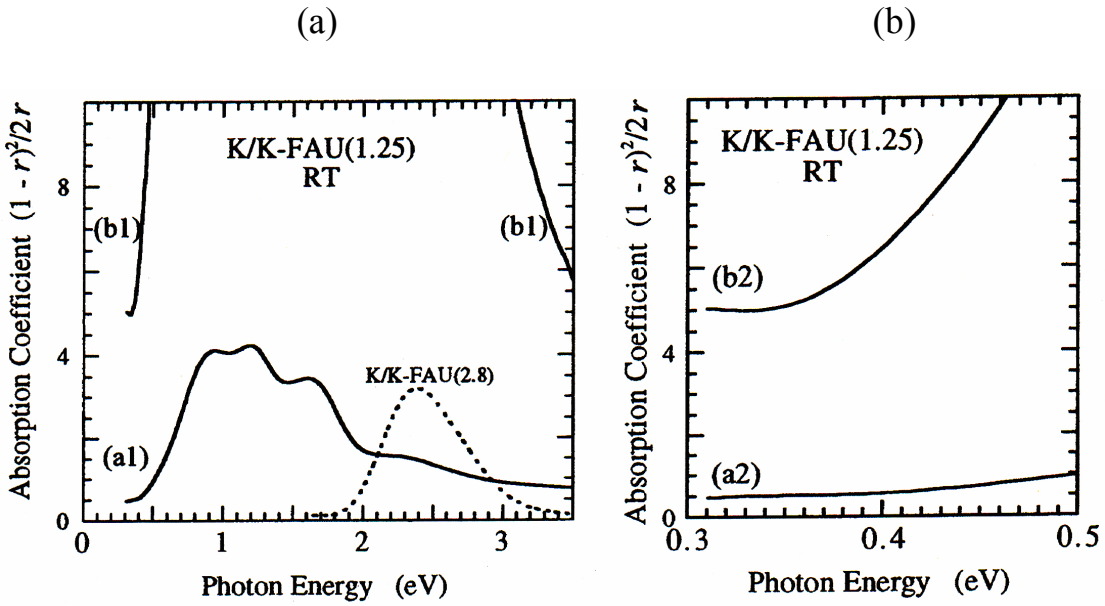

Fig. 1.22. Optical absorption spectra of K-loaed K-X(1.25) for sample at dilute loading density (a1) sample and higher loading density (b1) sample measured at room temperature (a) and a expanded plot at low photon energy region (b) [56].

In 1999, Ikemoto et al. have studied the K clusters of in zeolite X [56]. Figure 1.22 (a) shows the optical absorption spectra of K-loaed K-X(1.25) for dilute sample (a1) and higher loading density sample (b1) measured at room temperature. As we seen in this figure, the optical absorption spectrum of sample (a1) shows continuous absorption band at lower photon energy region < 2 eV. This behavior of absorption spectrum is quite different with that of K clusters in zeolite Y, which is plotted in dotted line in Fig. 1.22 (a) for comparison. Differently from the case of K/K-Y(2.8), the absorption bands at K/K-X(1.25) is assigned to the excitation of electron of clusters in supercage due to lower excitation energy. In addition, in the expanded plot in Fig. 1.22 (b), the authors observed the stronger absorption coefficient in sample (b2) when compare with that of sample (a2). This behavior is typically observed due to Drude term of free

carriers, implying the sample at higher loading density may be in metallic state [56-57]. According to structure of zeolite X, supercages are arranged in diamond structure with tetrahedral symmetry. In addition, supercages share large 12-membered ring window. If the electron wave function between neighboring supercage clusters overlap each other, then the sp^3 hybridization can be expected to realize. Hence the continuous absorption band at lower photon energy region in dilute sample of K/K-X(1.25) can be understand as the inter-band absorption from sp^3 bonding state to sp^3 antibonding state [58].

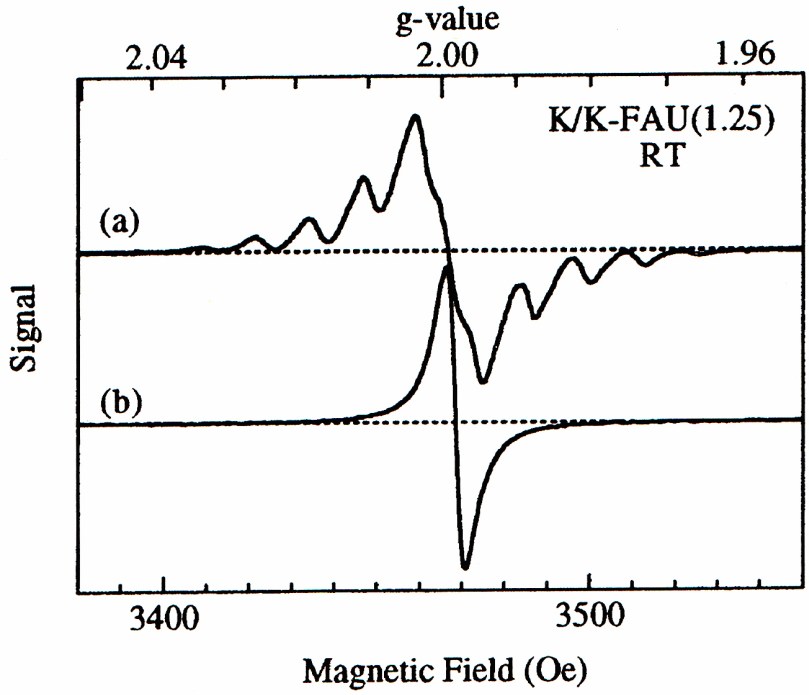

Fig. 1.23. ESR spectra measured at room temperature of K-loaded K-X(1.25) for dilute sample (a) and higher loading density sample (b) [56].

The ESR spectrum of dilute sample K/K-X(1.25) can be seen in Fig. 1.23. A hyperfine structure with 10 components is observed. This hyperfine structure is explained by the K_3^{2+} cluster, which is formed in supercage. This result indicates that the K_3^{2+} clusters are localized in supercage, and consistent with the observed optical absorption spectra. A single narrow line in the ESR spectrum is found at higher loading density sample (b). This kind of ESR spectrum may be originated from the metallic phase transition of K_3^{2+} clusters.

1.3.4 Alkali metal clusters in zeolite LSX

Low silica X (LSX) zeolite has the ratio of Si/Al = 1, this is the lowest Si/Al ratio when compare with those of zeolite X and Y. It also means that zeolite LSX can contain largest number of alkali cations in the FAU framework. In the case of zeolite LSX, there are 12 alkali cations can be distributed in the zeolite framework. In this section an overview of previous studies on Na clusters, K clusters and Na-K alloy clusters incorporated in zeolite LSX will be introduced.

A. Na clusters in zeolite LSX

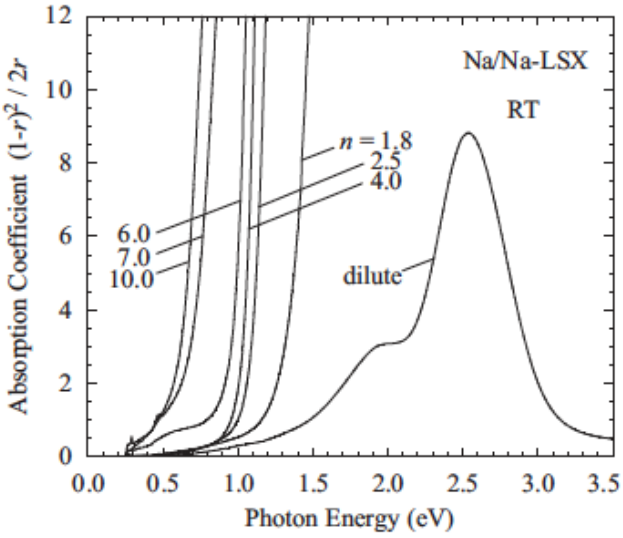

Fig. 1.24. Optical absorption spectra of Na-loaded Na-LSX at various loading densities measured at room temperature [59].

Nakano et al. have studied the physical properties of Na clusters in zeolite LSX by loading Na atoms into Na-type LSX at various loading density [59]. The optical absorption spectra of Na-loaded Na-LSX for dilute sample and higher loading density samples are shown in Fig. 1.24. A significant absorption band is observed at ≈ 2.5 eV. Similar behavior was also observed in the optical absorption spectrum of Na-loaded Na-X(1.25) and Na-loaded Na-Y(2.8) [50]. Considering a cluster in β-cage with the effective inside diameter of ≈ 7.5 Å, the energy excitation of a free electron from 1s- to 1p state will be 2.8 eV. This value is comparable with the energy or absorption bands observed for dilute sample of Na/Na-LSX. The result suggests the appearance of Na cluster in β-cage in this sample. For the samples with $n \leq 10$, the absorption

tails with energy gaps are observed at lower photon energy region, implying insulating phase of samples.

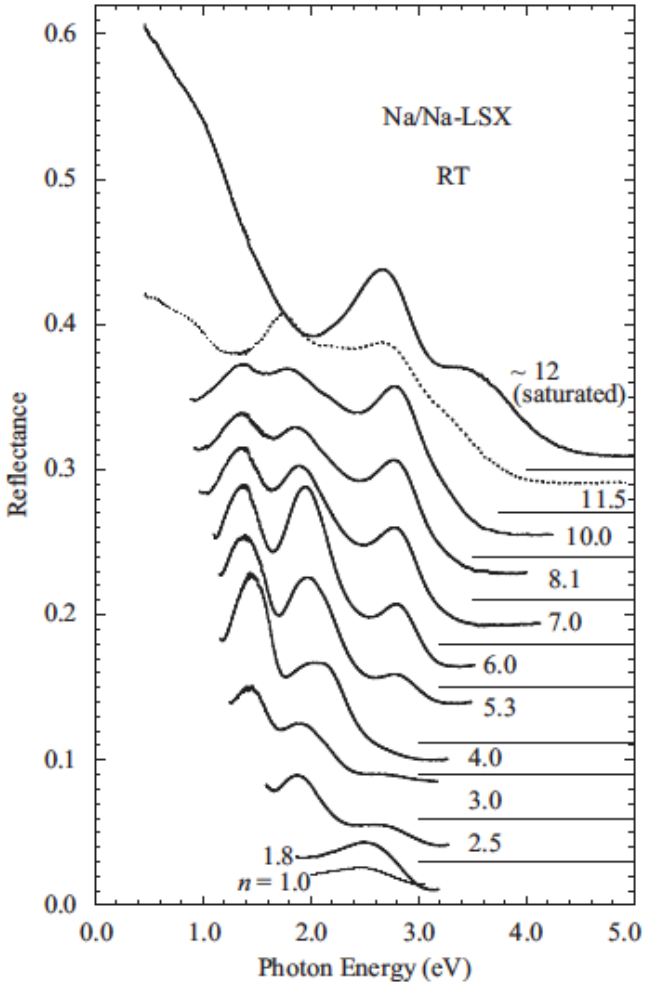

Fig. 1.25. Optical reflectance spectra of Na-loaded Na-LSX at various loading densities *n* measured at room temperature [59].

Figure. 1.25 plots the optical reflectance spectra of Na/Na-LSX measured at room temperature for various loading density samples. At lower loading density sample, n = 1.0 and 1.8, obviously reflection bands at ≈ 2.5 eV are observed. On the other hand, the ESR spectra consisting of 13 lines hyperfine structure are also found in this sample. That means the Na_4^{3+} clusters are generated in β-cage. One should be noted that the ESR spectrum just reflects the unpaired electron. Hence for the case of sample with n = 1.8, it is necessary to assume 80% of β-cage are occupied by spin singlet clusters and the ESR measurement could not detect them. The larger occupancy of singlet clusters may be originated from the larger electron phonon

coupling due to larger ionization energy of Na atoms. With increasing loading density $n \geq 2.5$, the reflection band at ≈ 2.5 eV is suppressed, and new reflection bands at ≈ 1.4, 1.9 and 2.8 eV appear. These bands can be assigned to the surface plasmon excitation of Na clusters, which is generated in supercage. A metal – insulator transition is also suggested from the optical reflectance spectra because the strong reflectance and increasing reflectivity at lower photon energy region, which is assigned to the Drude term due to metallic phase, are found at samples with $n \geq 11.5$. In terms of magnetic properties, the magnetic susceptibility measurements carried out in Na/Na-LSX reveal that all samples with $n \geq 2.5$ obey the Curie – Weiss law below 100 K. The Curie constants of these samples are very small. These results clearly indicate that almost Na clusters are in spin-singlet states [59].

In order to clarify insulating states of Na/Na-LSX at intermediate loading density sample as well as the suddenly appearance of insulator – metallic transition at higher loading density samples, which was suggested from the optical properties, further investigation has been carried out. Nozue et al. have reported the electrical transport properties of Na/Na-LSX at various loading densities [60]. The results of electrical resistivity measurements are plotted in Fig. 1.26. As shown in this figure, the resistivity of samples with $n = 7.9$ and 10.1 are very high, in the order of 10^7 Ω·cm, at room temperature. With decreasing temperature, the values of resistivity quickly increase and excess the value of 10^9 Ω·cm. The activation energy is ≈ 0.4 eV. For higher loading density samples $n = 11.3$, 11.6 and 12, a systematic decrease of resistivity at room temperature is obtained. At $n = 12$, the activation energy nearly vanishes. Although the resistivity at 2 K of this sample is higher than that of ordinary metal, but there is existence of carriers. The sample can be considered to be metallic state. These results are consistent with the insulator – metallic phase transition expected from optical results.

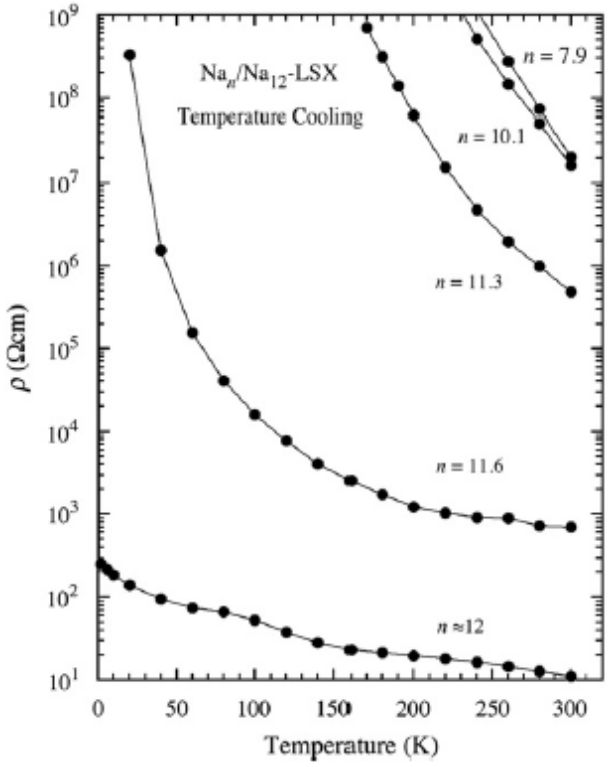

Fig. 1.26. Temperature dependence of electrical resistivity of Na/Na-LSX at various loading densities [60].

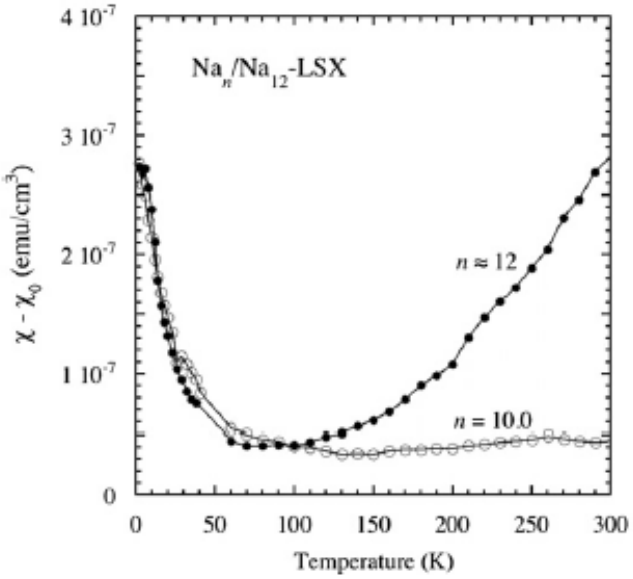

Fig. 1.27. Temperature dependence of magnetic susceptibility of Na/Na-LSX at loading density sample n = 10.0 and ≈12 [60].

In the temperature dependence of magnetic susceptibility measured for the samples with n = 10.0 and ≈12, which is shown in Fig. 1.27, a clear difference in the behavior

of temperature dependence has been observed. At n = 10.0, the magnetic susceptibility seems to be temperature independent above 100 K. In the meanwhile, sample with $n = \approx 12$ exhibits the thermal excitation of paramagnetic moment at similar temperature region. The value of 3 x 10^7 (emu/cm^3) at room temperature corresponds to 30 % of supercage occupied by magnetic moments with spin ½. The model of small multiple bipolarons and large polarons has been proposed to explain the properties of system. According to the theory of self-trapping of electron in deformable lattice, electrons can make deep potentials due to strong electron phonon coupling and can be trapped themselves in these potentials when the deformation potential is deep enough to bound an electron, and so-called small polaron [61]. If two electrons are introduced into the potential well, if the electron phonon interaction is larger enough to against the Coulomb repulsive interaction, then small bipolarons will be realized. They are in spin singlet state and rarely to be moved due to heavy mass. The Na clusters in β-cage at $n \leq 2$ are assigned to be small bipolarons. If larger number of electrons are introduced in the potential well simultaneously, and they can occupy higher quantum states of clusters, then the small multiple bipolarons can be generated. The Na clusters with nonmagnetic and insulating state of samples with $2 \leq n \leq 11$ are attributed to this kind of small multiple bipolarons. According to the experimental results, the metallic phase appear with only one additional Na atom. The small multiple bipolaron states may have a limitation, where the electron cannot be bounded within the potential well. At this limitation, additional electron will be stabilized in large polaron states. The insulator – metallic transition may be occurred in this situation. Figure 1.28 shows a schematic illustration of adiabatic potential of polarons proposed in metallic phase of Na/Na-LSX. The adiabatic potential for polarons is a double minimum as seen in the figure. The larger polaron states are stabilized and many larger polarons create metallic state of sample. In the larger lattice distortion region, electron can be localized in small polaron with paramagnetic moments and thermal excitation of paramagnetic clusters can be occurred at higher temperature region, as experimentally observed in the temperature dependence of magnetic susceptibility of metallic sample with loading density n = 12.

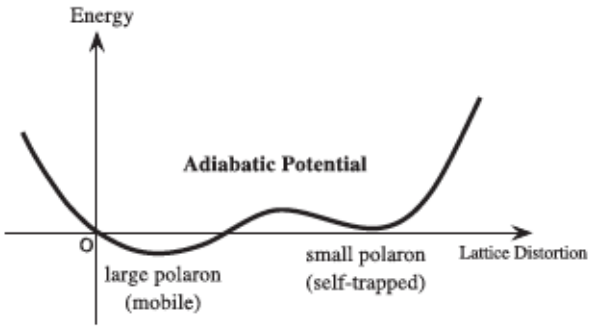

Fig. 1.28. Illustration of adiabatic potential of polarons proposed in metallic phase of Na/Na-LSX [60].

More recently, the crystal structure analysis has been carried for the Na-loaded Na-LSX with the loading density n = 16.7 and 9.4 ($Na_{16.7}/Na_{12}$-LSX and $Na_{9.4}/Na_{12}$-LSX), which are above and below the insulating – metallic phase transition, in order to understand this phase transition [82]. By using the powder X-ray diffraction, the authors have investigated the crystal structure of $Na_{16.7}/Na_{12}$-LSX and $Na_{9.4}/Na_{12}$-LSX in details and determined the Na distribution in Na-LSX.

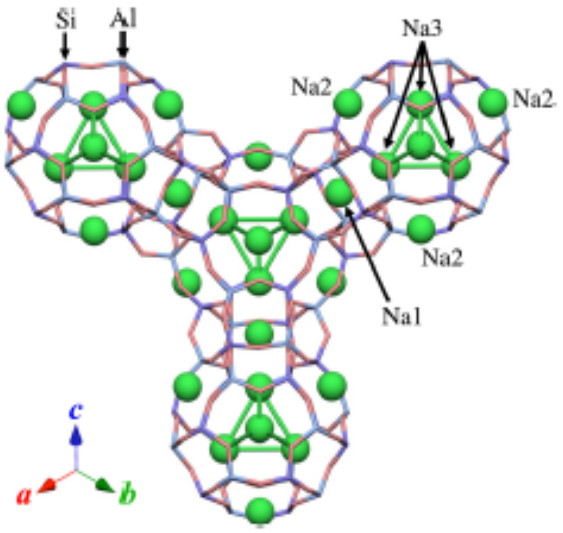

Fig. 1.29. Na cation distribution in β-cage and double 6-membered ring (D6R) at $Na_{16.7}/Na_{12}$-LSX and $Na_{9.4}/Na_{12}$-LSX [82].

For $Na_{16.7}/Na_{12}$-LSX, the results pointed out there are three Na sites, including Na1, Na2 and Na3 as shown in Fig. 1.29, have been detected. The site Na1 is located in the center of hexagonal prism (double 6-membered ring), which connects two neighbor β-

cages. The site Na2 lies at the single 6-membered ring, where is the connection between β-cage and supercage. The Na cations located at site Na2 is slightly shifted to supercage side from the center of single 6-membered ring with T_d symmetry. On the other hand, the site Na3 forms a tetrahedral assembly inside β-cages. The results also show that all of cation sites Na1, Na2 and Na3 are almost fully occupied. Totally there are 77.5 atoms in these three sites in a unit cell. However the number of atoms belongs to the β-cage and double 6-membered ring are normally smaller or equal 64 atoms per unit cell. That means the additional Na cations are located in supercage. Similar distribution of Na cations is also confirmed in $Na_{9.4}/Na_{12}$-LSX. In Na-loaded zeolite Y, the paramagnetic clusters Na_4^{3+} are formed in β-cages, however the clusters formed in Na-loaded Na_{12}-LSX may be mainly singlet clusters because there is no evidence of localized magnetic moments in the measurement of magnetic susceptibility. Therefore Na_4^{2+} clusters with two electrons occupied 1s-state of β-cage have been proposed. In addition the multiple Na sites in supercage considered. From the Rietveld refinement method, additional Na sites, Na5 and Na6, are discovered at the sharing 12-membered ring (12R) between supercages. The site Na5 stays at the center of 12-membered ring, while the site Na6 is located in the plane of 12-membered ring with six equivalent positions, as displayed in Fig. 1.30.

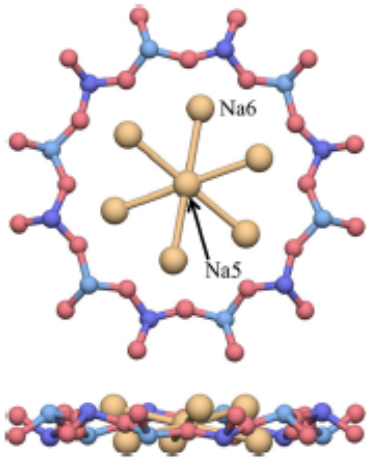

Fig. 1.30. Distribution of Na cations at 12-membered ring in $Na_{16.7}/Na_{12}$-LSX [82].

Moreover, additional Na sites such as Na4, Na7, Na8 and Na9 have been found in supercage in case of $Na_{16.7}/Na_{12}$-LSX. As shown in Fig. 1.31, site Na4 stays at the 4-membered ring, equivalent to site III in the typical cation site of LSX zeolite, and connects two sites Na6 with short atomic distance. The site Na7 is located inside supercage. The results indicate that the sites Na4, Na6 and Na7 will not exist

simultaneously. In the center of supercage, the site Na9 is surrounded by site Na8, and three sites Na7, Na8 and Na9 do also not exist at the same time. The illustration of two neighbor supercage Na clusters is displayed in Fig. 1.32. Two neighbor Na clusters seem to be connected by site Na5 at the center of 12-membered ring.

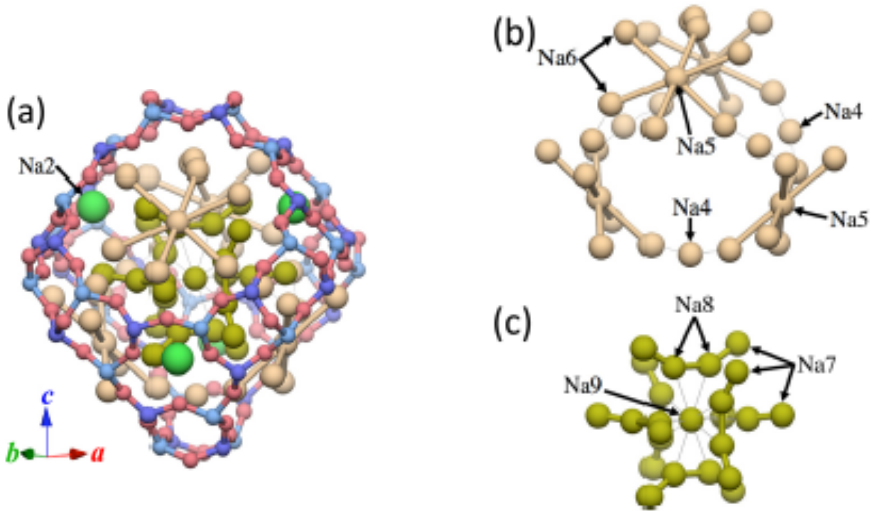

Fig. 1.31. Na cluster in supercage of $Na_{9.4}/Na_{12}$-LSX (a), close to the framework and 12-membered ring (b) sites Na7, Na8 and Na9 at the center of supercage (c) [82].

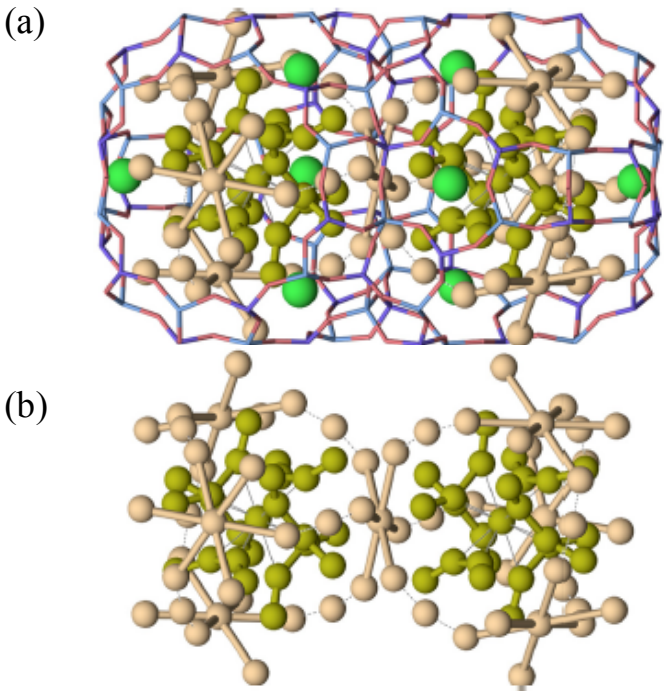

Fig. 1.32. Adjacent supercage Na clusters (a) and the connection by site Na5 between them (b) [82].

For the case of $Na_{9.4}/Na_{12}$-LSX, the distribution of Na cation is almost similar with that of $Na_{16.7}/Na_{12}$-LSX. However, the density of Na cations distributed in supercage is lower in the case of $Na_{9.4}/Na_{12}$-LSX. Although the Na density is lower in the supercage in $Na_{9.4}/Na_{12}$-LSX than $Na_{16.7}/Na_{12}$-LSX but the sites Na1, Na2 and Na3 are still fully occupied. This result suggests that the Na cations are preferred to distribute in β-cage and double 6-membered ring (D6R) rather than supercage in Na loaded Na_{12}-LSX.

In the Na loaded Na_{12}-LSX system, the sites Na1, Na2, Na3 and Na6 are located near the inner wall of zeolite framework. Differently, the sites Na5, Na7, Na8 and Na9 are located at the free space sites, where occupied with increasing loading density. Due to the attraction between the negatively charge of zeolite framework and Na cations, the cation sites at inner wall may be more stable. On the other side, the distribution of Na cation at the free sites in the center of supercage may require the number of s-electrons. These s-electrons and Na cations at large free space can form the large polaron states contribute to the metallic state at $Na_{16.7}/Na_{12}$-LSX. In addition, from the electron density analysis of Na loaded Na_{12}-LSX system, the results indicate that Na clusters forms a large and complex network between second neighboring supercage via 12-membered ring. Near the 12-membered ring, the electron transfer between Na and O atoms is realized. The long Na chain may indicate a trace of diffusion path. The electric conductivity observed in Na loaded Na_{12}-LSX system is strongly related to the number of Na loaded atoms in supercage and Na-Na connectivity [82].

B. K clusters in zeolite LSX

K clusters are generated by loading of guest K atoms into K-type of zeolite LSX. The sample name is denoted as K_n/K_{12}-LSX where n is K loading density. Figure 1.33 presents the temperature dependence of magnetization measured under applied magnetic field of 10 Oe for K_n/K_{12}-LSX at various loading densities. As seen in this figure, the spontaneous magnetization is obviously observed for the samples with loading density $n \approx 9$.

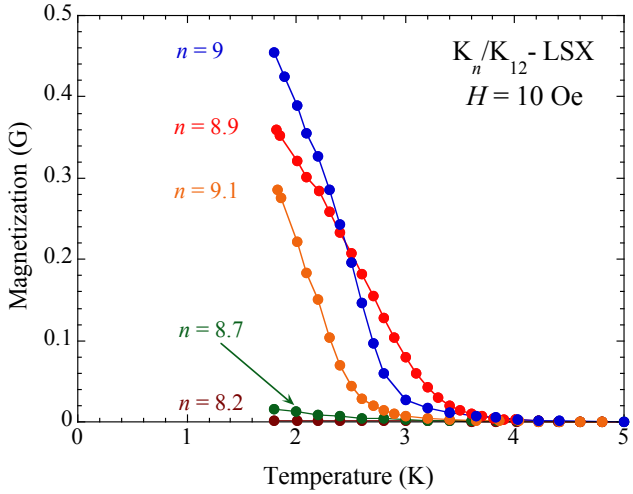

Fig. 1.33. Temperature dependence of magnetization for K_n/K_{12}-LSX at various loading densities measured under a weak applied magnetic field of 10 Oe [62].

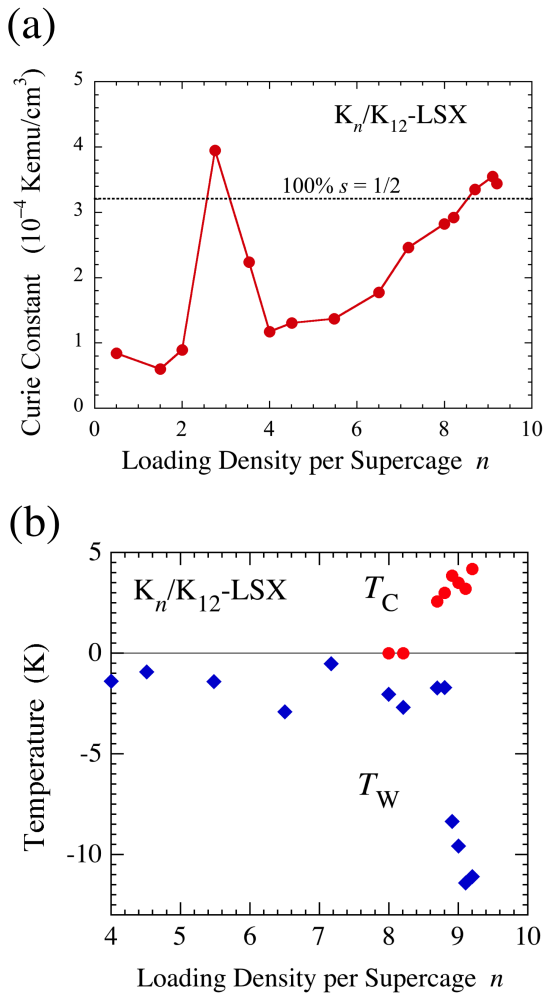

Fig. 1.34. K-loading density n dependence of the Curie constant (a) and Curie, Weiss Temperature (b) for K_n/K_{12}-LSX [63].

From the temperature dependence of magnetization the extrapolated Curie temperature is estimated. The temperature dependence of magnetic susceptibility well obeys the Curie – Weiss law and is used to estimate the Curie constant as well as Weiss temperature [63].

The K loading density dependence of the Curie constant and Weiss temperature, Curie temperature and are plotted in Fig. 1.34 (a) and (b), respectively. At lower loading density sample, $n < 2$, the value of Curie constant corresponds to 20 % of supercage occupied by magnetic moment with spin ½. With increasing loading density, a peak at $n \approx 3$ is obviously observed. Afterward, the Curie constant increases with increasing loading density and reaches the value, which correspond to 100 % of supercage occupied by spin ½. According to the negative values of Weiss temperature, the antiferromagnetic interaction is assigned to dominate the magnetic interaction of samples. The spontaneous magnetization of samples at $n \approx 9$ is then explained by the ferrimagnetism similarly with the case of K_n/Na_4K_8-LSX, in which two nonequivalent magnetic sublattices coupled antiferromagnetically are generated in supercage and β-cage clusters network. The extrapolated Curie temperature exhibits the obtained spontaneous magnetization at higher loading density samples $n \approx 9$. The Weiss temperature shows negative value in all of samples. In addition, Weiss temperature abruptly decreases down to -10 K at highest loading density sample.

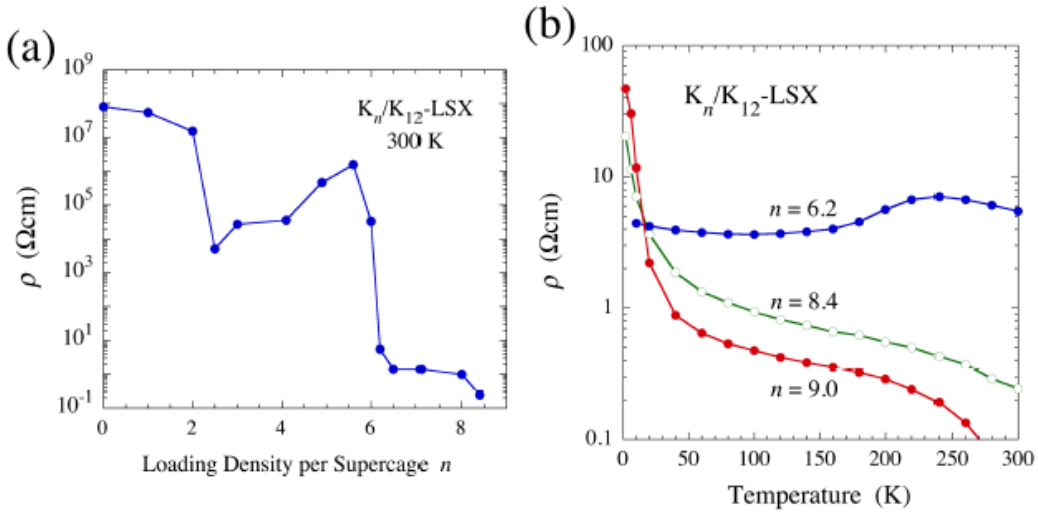

Fig. 1.35. Loading density dependence of electrical resistivity ρ at room temperature (a) and temperature dependence of electrical resistivity at n = 6.2, 8.4 and 9.0 (b) for K_n/K_{12}-LSX [63].

The electric transport properties of K_n/K_{12}-LSX are also carried out. Figure 1.35 (a) displays the loading density dependence of electrical resistivity ρ at room temperature for K_n/K_{12}-LSX. As seen in this figure, the values of resistivity at lower loading density are very high, in the order of 10^7 Ω·cm. A abruptly decrease of resistivity, down to the order of 10^3 Ω·cm, is observed at $n > 2$. With increasing loading density, the resistivity gradual increases and suddenly drops at $n \approx 6$. At higher loading density samples, the values of resistivity are very small. As shown in Fig. 1.35 (b), the temperature dependence of electrical resistivity for K_n/K_{12}-LSX exhibits quite strange behavior. For the sample with n = 6.2, the resistivity are very small in whole temperature range, indicating the contribution of carriers and nearly metallic state of sample. At higher loading density samples, n = 8.4 and 9.0, a decreasing of resistivity at higher temperature region is observed. However at lower temperature region, the resistivity quickly increases, shows a narrow gap and reaches the value nearly 100 times larger than that at higher temperature region. This behavior of temperature dependence of electrical resistivity may be possibly assigned to the Kondo insulator. It should be reminded that these samples are ferrimagnetism. A model, in which the Fermi energy stays at the center of narrow band of supercage clusters network and the energy state of localized magnetic moment in β-cage stays below the Fermi energy, has been proposed. In the case of ferrimagnetism at higher loading densities of K_n/K_{12}-LSX, the magnetic moments are realized in both of supercage and β-cage network then the metallic electrons in supercages have spin polarization. In addition, the polaron effect has been considered to explain the anomaly at $n \approx 3$, where the high Curie constant and the low electrical resistivity have been found.

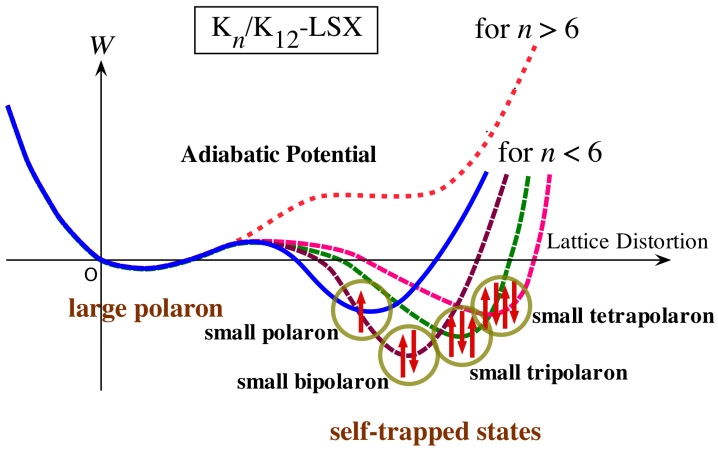

Fig. 1.36. Schematic illustration of polaron effects in K_n/K_{12}-LSX [63].

Figure. 1.36 illustrates an adiabatic potential for polaron effects considered in K_n/K_{12}-LSX. For the samples at lower loading density, $n < 2$, small bipolaron are generated, explaining small values of Curie consant and the insulating phase of samples. With increasing loading density, at $n \approx 3$, one more K atoms are introduced into K-LSX, and one more electron leads to the formation of small tripolaron. This small tripolaron are paramagnetic and affect to the conductivity of system due to open electronic cell. As a result, the high value of Curie constant and the low resistivity are observed at $n \approx 3$. At higher loading density samples, multiple small polarons can be formed but they will be unstable above a certain value of loading density and leading to the formation of large polarons, which contribute to the conductivity of system. A similar situation appears in the case of Na_n/Na_{12}-LSX, which is introduced in the last section. In the case of K_n/K_{12}-LSX, the insulator – metallic transition is observed at $n \approx 6$. The transition appears earlier than that of Na system because of weaker electron phonon coupling due to smaller ionization energy of K metal [63].

C. Na-K alloy clusters in zeolite LSX

In some case FAU type framework of zeolite LSX can contain both of Na^+ and K^+ cations. The chemical formula of dehydrated zeolite LSX then will be given by $Na_xK_{12-x}Al_{12}Si_{12}O_{48}$, where x here is the Na-concentration. The K atoms can be loaded into this kind of zeolite LSX with loading density n and the Na-K alloy clusters can be generated. The chemical formula is now $Na_xK_{12-x+n}Al_{12}Si_{12}O_{48}$ and is abbreviated as K_n/Na_xK_{12-x}-LSX hereafter. The sample K loaded K-LSX [63], which is mentioned above, can be treated as the case $x = 0$. On the other hand, several systems with $x =$ 1.0, 1.5, 2.4 and 4.0 have been prepared and studied [64-67]. The ferrimagnetic properties have been observed in all of these systems at specific region of loading density n. In particular, a clear N-type ferrimagnetism has been found at K_n/Na_4K_8-LSX ($x = 4.0$). According to the experimental results, the ferrimagnetism is strongly varied depending on both of Na-concentration x and K loading density n.

a) N-type ferrimagnetism of K-loaded Na_4K_8-LSX (K_n/Na_4K_8-LSX ($x = 4.0$))

In the case of Na_4K_8-LSX, the FAU type framework of zeolite LSX contains $4Na^+$ and $8K^+$ cations. The Na-K alloy clusters are generated by loading of guest nK atoms, n can be called as K loading density. In Fig. 1.37, we re-plot the optical absorption

spectra for K-loaded Na_4K_8-LSX at dilute loading density from reference [67]. As we can see in this figure, a continuous absorption band is observed. Let consider a spherical potential well for electron confined in supercage clusters. Because the supercages share a larger window of 12-membered ring, therefore we can expect the T_d symmetry for supercage. The optical excitation energies between A_1 ground state to two T_2 states in T_d symmetry are estimated to be ≈ 0.86 and ≈ 1.9 eV with the diameter of 13 Å of spherical potential well. Therefore, the continuous absorption band observed in the optical absorption spectrum of K-loaded Na_4K_8-LSX at dilute loading density can be attributed to this kind of clusters in supercage [67].

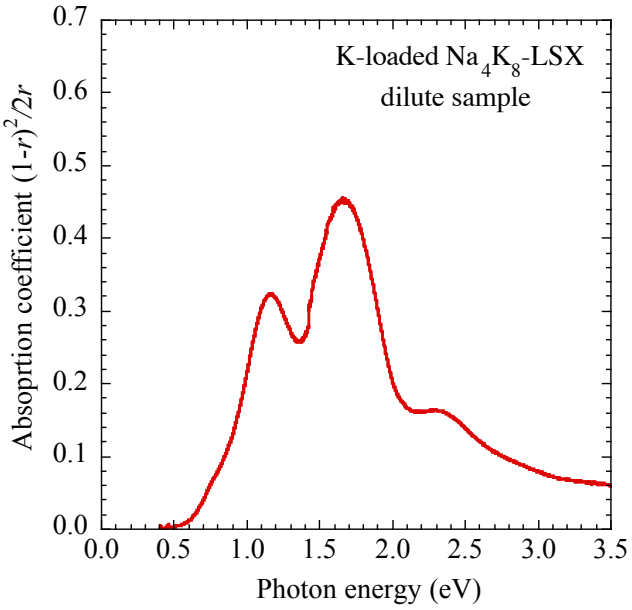

Fig. 1.37. Optical absorption spectrum of K-loaded Na_4K_8-LSX for dilute sample [67].

The measurements of temperature dependence of magnetization reveal the N-type ferrimagnetic properites for K_n/Na_4K_8-LSX (x = 4.0) at loading density $6.7 \leq n \leq 8.0$ [64-65]. A typical temperature dependence of magnetization for N-type ferrimagnetism observed for K_n/Na_4K_8-LSX (x = 4.0) at n = 7.8, measured under a weak applied magnetic field of 10 Oe, is re-plotted in Fig. 1.38 [67]. With decreasing temperature, the magnetization quickly increases below ≈ 20 K. In addition, a clear zero-minimum of magnetization can be seen at ≈ 5 K. Afterward, the magnetization increases and reaches value of ≈ 0.18 G at the lowest temperature of 1.8 K. The

temperature where the magnetization exhibits the zero-minimum is called compensation temperature. This behavior of temperature dependence of magnetization obviously indicate that the sample K_n/Na_4K_8-LSX (x = 4.0) at n = 7.8 is the Néel's N-type ferrimagnetism.

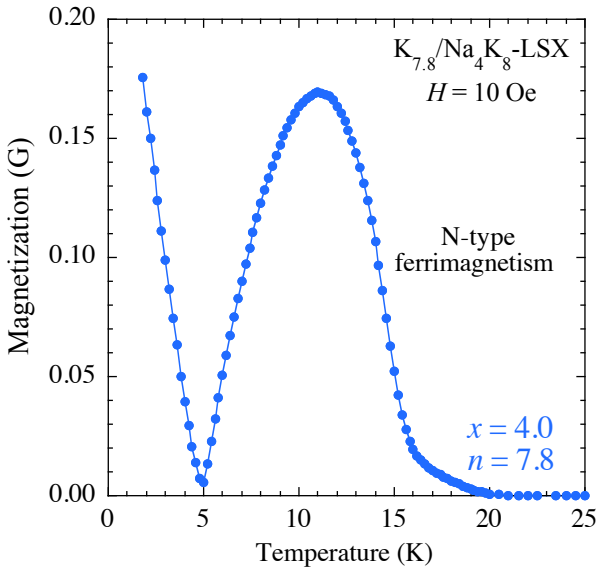

Fig. 1.38. Temperature dependence of magnetization measured under a weak applied magnetic field of 10 Oe for K_n/Na_4K_8-LSX (x = 4.0) at n = 7.8 [67].

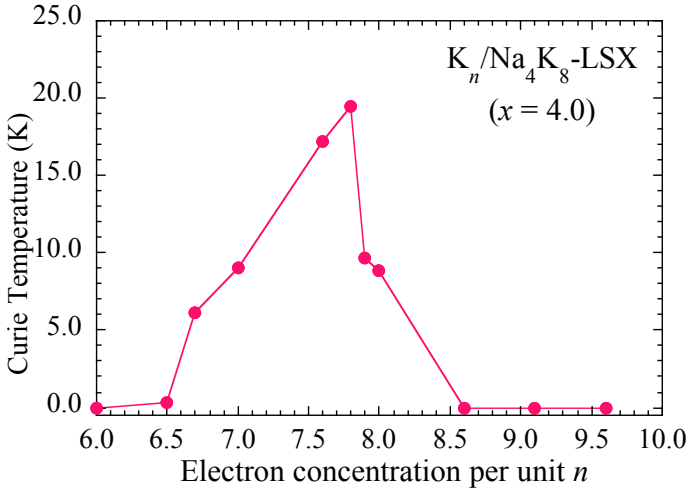

Fig. 1.39. K loading density dependence of Curie temperature of K_n/Na_4K_8-LSX (x = 4.0) [65].

The K loading density dependence of Curie temperature for K_n/Na_4K_8-LSX (x = 4.0) is plotted in Fig. 1.39 [65]. With increasing loading density, the Curie temperature

suddenly appears at n = 6.7. Then a sharp peak of the Curie temperature is observed at higher loading density region. The highest Curie temperature is ≈ 20 K, which is observed for K_n/Na_4K_8-LSX (x = 4.0) at n = 7.8. In addition, the magnetization curve measured at 1.8 K for K_n/Na_4K_8-LSX (x = 4.0) at n = 7.8 shows a spin-flop transition, which is typically observed in a ferrimagnetic materials.

A model of two non-equivalent magnetic sublattices has been proposed to explain the ferrimagnetism observed at K-loaded Na_4K_8-LSX at higher K loading density [64,67]. One sublattice is constructed of clusters in supercage network and forms a diamond structure network of itinerant electron ferromagnetism. Another sublattice is constructed of clusters in β-cage network. The size of the β-cage is much smaller than that of the supercage, but an electron can be trapped in β-cage at higher loading density. The magnetic interaction between β-cage clusters is very weak because of separation of adjacent β-cage cluster by narrow double 6-membered ring. In addition, these two magnetic sublattices have antiferromagntic interaction, but the magnetic moments are not equivalent to each other. The finite antiferromagnetic interaction can be expected through single 6-membered ring window between β-cage and supercage. The schematic illustration of this model is given in Fig. 1.40.

In this system, the supercage magnetic sublattice is in a nearly ferromagnetic state and the itinerant electrons in clusters of supercage cannot order spontaneously. If the bandwidth of electrons in supercage clusters network is wider than that limit of the Mott insulator, we can expect the metallic state for supercage clusters network. Recently the measurement of electrical resistivity for K-loaded Na_4K_8-LSX has revealed the metallic properties of samples at higher K loading density. The density of state at the Fermi energy of the supercage clusters network can be expected to be high enough to stabilize a ferromagnetic or nearly ferromagnetic state in supercage clusters network. In addition, if an electron can be well localized in β-cage cluster, then magnetic moment can be generated in β-cage clusters network. Finally the antiferromagnetic interaction between the localized magnetic moments in β-cage clusters network and electron in supercage clusters network can be provided through the single 6-membered ring. This antiferromagnetic interaction also has the contribution to stabilizing the ferromagnetic sublattice in supercage clusters network.

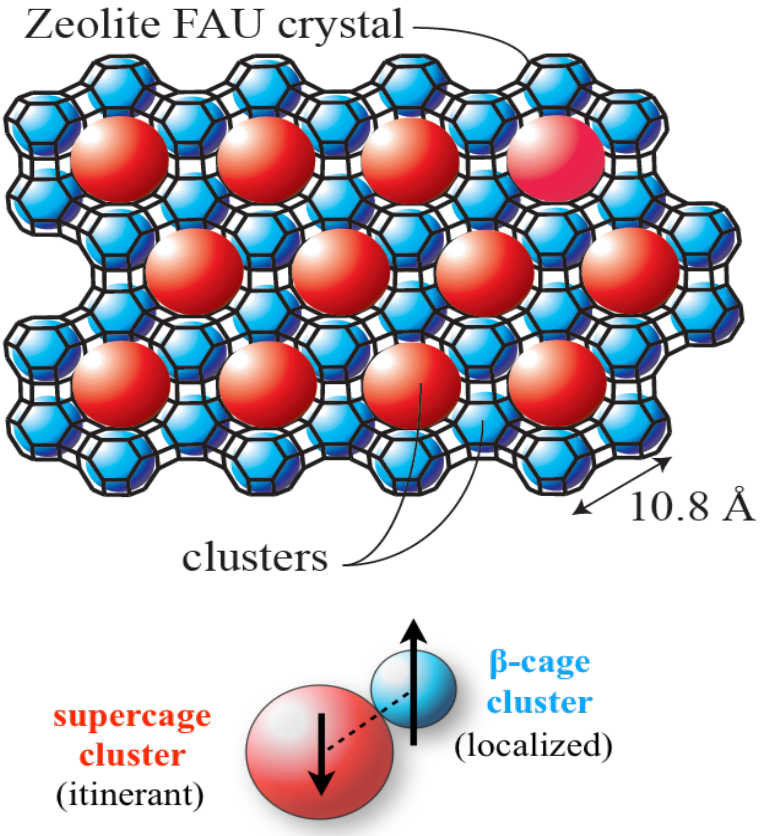

Fig. 1.40. Schematic illustration of a model of two non-equivalent magnetic sublattices in zeolite LSX.

Below the Curie temperature, the magnetic moments in supercage cluster network are expected to be ferromagnetic ordering. The localized magnetic moments in *β*-cage clusters network can be generated simultaneously. With decreasing temperature, magnetic moments in *β*-cage clusters network grow their magnitude equally with magnetization in supercage cluster network at compensation temperature and have opposite spin direction. As a result, the clear zero-minimum is observed. At lower temperature region, the magnetic moments in *β*-cage clusters network continuously grow and dominate the magnetization of system. The picture of localized magnetic moment of in *β*-cage clusters network realized in metallic phase of supercage clusters network is quite similar with the Kondo lattice. However, differently from the ordinary Kondo lattice, electrons in metallic supercage clusters network have spin polarization and strong correlation [65,67].

b) Na-K alloy clusters zeolite LSX of other x systems (x = 1.0, 1.5 and 2.4)

The Na-K alloy clusters in K loaded Na_xK_{12-x}-LSX in other systems at lower Na-concentration x = 1.0, 1.5 and 2.4 have been investigated [65-66]. Figure 1.41 shows the optical absorption spectra of K loaded Na_xK_{12-x}-LSX (x = 1.0, 1.5 and 2.4) at dilute loading density. As seen in this figure, a significant main structure of the absorption spectra is observed at lower photon energy region < 2 eV. These continuous absorption bands are quite similar with those in dilute samples of K loaded Na_4K_8-LSX (x = 4.0) as well as K loaded K_{12}-LSX (x = 0). These continuous absorption bands can be assigned to the optical excitation of electron confined in supercage clusters. And there is no indication for the formation of clusters in in β-cage. The sharp peaks with weak intensity are also seen at ≈ 0.45 eV. These peaks can be attributed to the absorption of small amount of proton H^+ [68], which is remained in zeolite after the ion-exchange processes.

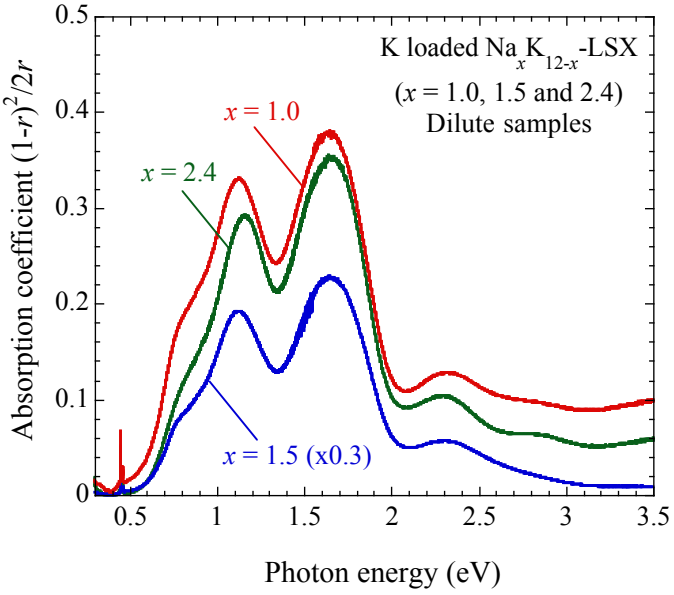

Fig. 1.41. Optical absorption spectra of dilute samples for K loaded Na_xK_{12-x}-LSX (x = 1.0, 1.5 and 2.4) [66].

The typical temperature dependence of magnetization (M-T) curves measured under a weak applied magnetic field of 10 Oe for K loaded Na_xK_{12-x}-LSX (x = 1.0, 1.5 and 2.4) are shown in Fig. 1.42. The data for K loaded Na_xK_{12-x}-LSX (x = 0 and 4.0) is plotted together for comparison. All of samples plotted in Fig. 1.42 have the highest value of the Curie temperature in their system. As shown in this figure, the shape of

M-T curves strongly depend on the Na-concentration *x*. The *M-T* curves for samples with $x = 4.0$, $n = 7.8$ and $x = 2.4$, $n = 8.5$ can be obviously assigned to the N-type ferrimagnetism. On the other hand, although other samples ($x = 1.5$, 1.0 and 0) behave the ferromagnetic properties but they exhibit different shape of *M-T* curves. This can be attributed to the different types of ferrimagnetism, which may be caused by the differences in the balance of magnetic sublattices.

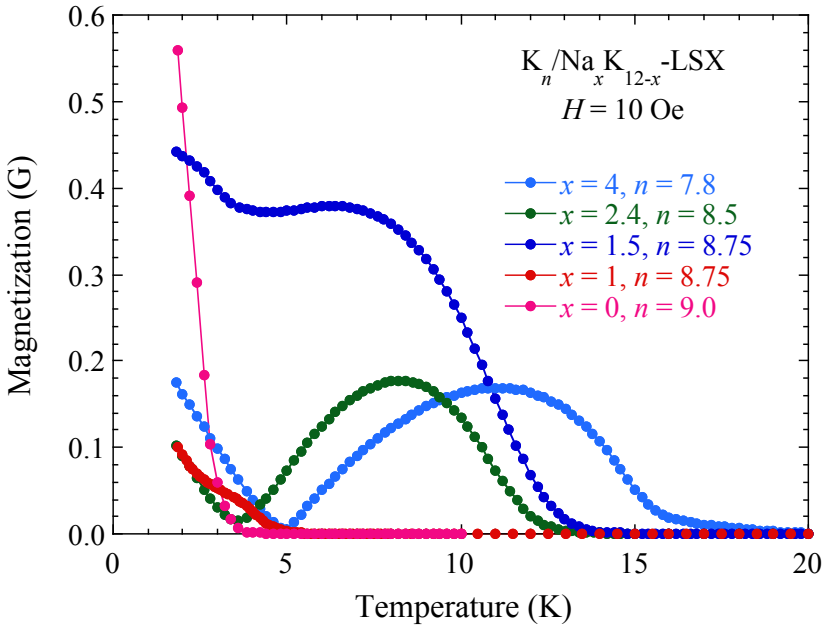

Fig. 1.42. Typical temperature dependence of magnetization of ferrimagnetism in K_n/Na_xK_{12-x}-LSX ($x = 0$, 1.0, 1.5, 2.4 and 4.0) [66].

The loading density dependence of Curie temperature for K_n/Na_xK_{12-x}-LSX ($x = 0$, 1.0, 1.5, 2.4 and 4.0) is displayed in Fig. 1.43. For $x = 4.0$, the Curie temperature has finite values for N-type ferrimagnetic samples $6.7 \leq n \leq 8.0$. In addition, a sharp peak is found at loading density $n = 7.8$. With decreasing Na-concentration *x*, though N-type ferrimagnetism is also observed at $x = 2.4$ but the ferrimagnetic phase shift to higher loading density region. Lower Na-concentration samples $x = 1.5$, 1.0 and 0, the ferrimagnetic phase has the tendency to appear at higher loading density region at $8.0 \leq n \leq 9.2$, $8.25 \leq n \leq 9.2$ and $8.7 \leq n \leq 9.1$ respectively [65-66]. These results indicate that the magnetic properties of samples system K_n/Na_xK_{12-x}-LSX ($x = 0$, 1.0, 1.5, 2.4 and 4.0) is strongly varied by the Na-concentration *x* as well as the K loading density *n*.

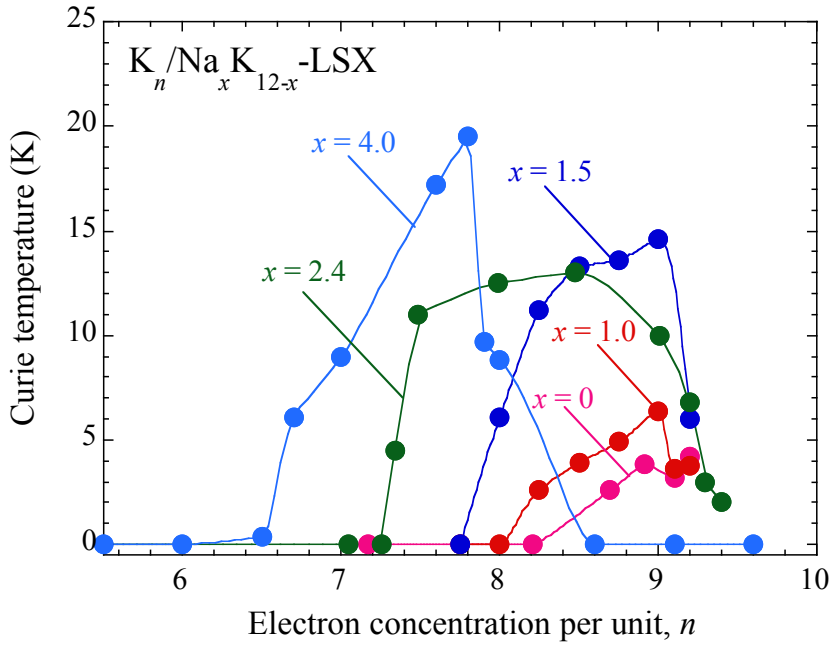

Fig. 1.43. Loading density dependence of Curie temperature for K_n/Na_xK_{12-x}-LSX (x = 0, 1.0, 1.5, 2.4 and 4.0) [66].

In order to discuss the strong dependence of magnetic properties on the x and n values in K_n/Na_xK_{12-x}-LSX samples, it is essential to consider the formation of magnetic moments in β-cage clusters and the interaction of magnetic moments in zeolite LSX. According to the structure of zeolite LSX, the β-cage has an effective inside diameter of ≈ 7.5 Å. It implies that β-cage is quite small, then there is no space for occupation of extra cations but one or two electrons can be trapped inside the β-cage. In the normal condition without electron correlation, the β-cage state is fully occupied by electrons below the Fermi energy and there is no localized magnetic moment. However in the real system the appearance of localized magnetic moment can be expected due to the strong electron correlation, which prevents the formation of two electrons state in β-cage. The electronic model, where the larger density of state (DOS) at the Fermi energy (E_F) supercage has the electron correlation with β-cage states has been proposed to explain the magnetic properties of K_n/Na_xK_{12-x}-LSX system. Figure 1.44 shows an illustration of electronic states for K_n/Na_xK_{12-x}-LSX system at higher and lower Na-concentration x with equivalent K loading density n [65]. In the higher x system, Na-rich, the β-cages may be expected to have deeper

potential than that of Fermi energy and be able to trap electrons. Because small size of *β*-cage then the electron-electron correlation is realized within *β*-cage. The localized electron in *β*-cage now has finite interaction with the metallic electrons in supercage network via single 6-membered ring window, which directly connect supercage and *β*-cage. The situation seems to be similar with the Kondo regime, where the localized magnetic moments have the interaction with itinerant electrons. On the hand, if the hybridization of electrons in supercage and *β*-cage is smaller, the RKKY interaction can be a candidate to provide the magnetic interaction in the system. Differently with the ordinary RKKY model, the supercage clusters network in LSX system is nearly itinerant ferromagnetic network with the magnitude of magnetic moments is comparable with that in *β*-cage. The N-type ferrimagnetic properties observed at higher *x* system (*x* = 2.4 and 4.0) occurs in this scheme [65-66].

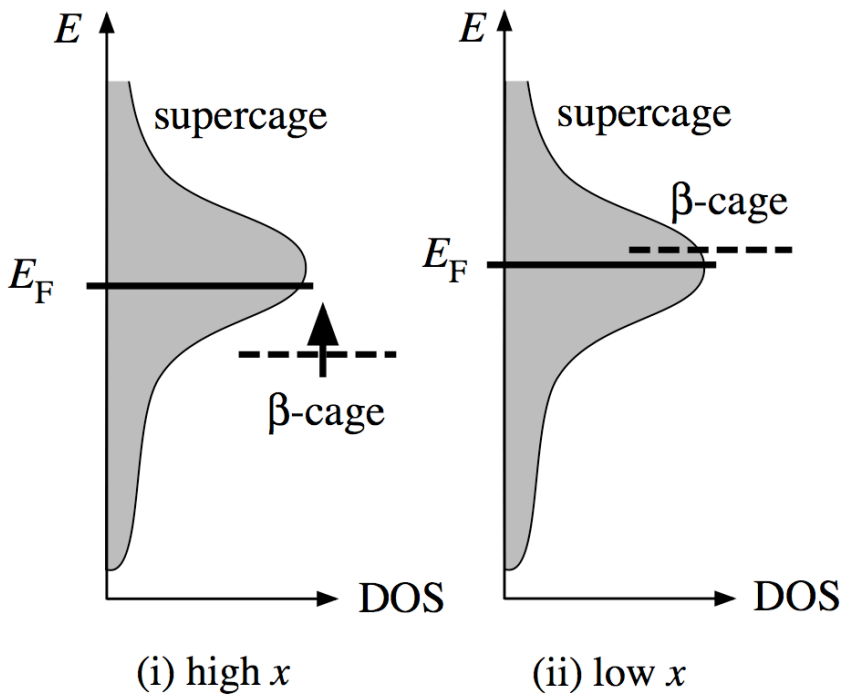

Fig. 1.44. Schematic illustration of electronic model for K_n/Na_xK_{12-x}-LSX at higher Na-concentration *x* (a) and lower Na-concentration *x* (b) at equivalent K loading density [65].

In the lower Na-concentration system (*x* = 1.5, 1.0 and 0), the balance between the *β*-cage and supercage potential will be changed due to the modification from Na-rich clusters at higher *x* system to K-rich clusters at lower *x* system. The *β*-cage potential becomes shallower and has higher energy than that of Fermi energy in supercage.

Therefore the condition of higher K loading density may be required for the occupation of electron in β-cage. Leading to the shift of ferrimagnetic phase with decreasing Na concentration. In addition, the magnetic interaction between electrons in supercage and β-cage as well as the magnitude of magnetic moments are also varied. This possibly changes in the magnetization of samples.

1.4 Superexchange interaction

The magnetic properties observed in materials can be considered as quantum phenomenon. According to the quantum mechanics, Heisenberg proposed the ordinary Coulomb interactions of electrons and the Pauli principle results to an exchange effect, which strongly coupling electrons spins and leading to the ferromagnetism. In the ferromagnetic materials contain Fe, Ni or Co atoms there is existence of the localized *d* electrons. The energy of direct ferromagnetic exchange interaction of the atoms *i* and *j*, whose have the spin S_i and S_j, is given by the form of:

$$V = -2J_{ij}S_i \cdot S_j \qquad (1.1)$$

With J_{ij} here is the exchange integral. This exchange integral essentially relating to the overlapping of the charge distribution of atoms *i* and *j*. In the other word, it relates to the interaction of electrons between neighbor atoms. The equation 1.1 is now called Heisenberg model for the magnetism of localized spins [68].

In 1949, by investigating the neutron diffraction of a pattern of MnO, Shull and Smart have found that MnO is an antiferromagnetic material [69]. The situation of magnetic exchange interaction in the case of MnO is quite different when compare with that of Heisenberg model. In MnO, the nearest neighbor Mn^{2+} ions are well separated by O^{2-} ions. On the other side, the Curie point of MnO is 122 K. This suggests the exchange coupling between individual ions is more than tenth of the ordinary exchange integral. That means the large magnitude of the exchange coupling seems to be extraordinary in terms of direct magnetic interaction. Therefore, the antiferromagnetic interaction between nearest neighbor Mn^{2+} ions is then proposed to have the indirect magnetic exchange interaction, which is now known as superexchange interaction, through the O^{2-} ligands [70].

The term of "superexchange interaction" is firstly mentioned by Kramers in 1934 [71]. In his idea, there is a possibility of the exchange spin coupling through the overlap of the wave functions between magnetic ions and intervening nonmagnetic ions. By using the perturbation theory, he found the exchange effect, which can transmit over a long distance. Afterward, the general formalism, which is proposed by Kramers, of superexchange interaction is improved by Anderson in 1950 [70]. According to the approaches of Anderson, the superexchange antiferromagnetic interaction and

superexchange ferromagnetic interaction are realized between cations with more than half filled of *d*-orbital and less than half filled of *d*-orbital, respectively. He chose the substance MnO to illustrate the superexchange interaction. Two Mn^{2+} magnetic ions and one O^{2-} nonmagnetic ion are assumed to have the arrangement in which the dumbbell shapes of *p*-orbitals in O^{2-} ion join the same direction with that of d-orbitals in Mn^{2+} ions. In other words, we have an 180^0 arrangement of Mn^{2+} - O^{2-} - Mn^{2+}. In the ground state, Mn^{2+} magnetic ions have five electrons in 3*d*-orbitals. Among these electrons, three of them localize at t_{2g} states, the remaining two electrons stay at e_g states. In the meanwhile, 2*p*-orbital of O^{2-} nonmagnetic ion is occupied by two electrons with spin-up and spin-down states. In the excited state, because of the overlaps between 3*d*-orbitals and 2*p*-orbital, one electron in 2*p*-orbital of O^{2-} nonmagnetic ion can have a virtual hopping to the neighbor 3*d*-orbital of Mn^{2+} magnetic ions. The remaining unpaired electron in 2*p*-orbital of O^{2-} nonmagnetic ion then has a direct exchange with the electrons in 3*d*-orbital of the other Mn^{2+} magnetic ions. The hopping of electron in 2*p*-orbital leads to the decreasing of total energy of system if the spin of Mn^{2+} magnetic ions are coupled antiparallel. The final interaction between Mn^{2+} magnetic ions will be strong superexchange antiferromagnetic interaction via intervening O^{2-} nonmagnetic ion. The schematic illustration for the ground state and excited state is given in Fig. 1.45 (a) and Fig. 1.45 (b), respectively. The effective exchange integral can be denoted by value of *J*. In order to estimate the magnitude of *J*, two parameters are needed to be considers. The first one is the energy matrix element *t* for hopping electron in 2*p*-orbital of O^{2-} nonmagnetic ion to the 3*d*-orbital of Mn^{2+} magnetic ions. The second one is increasing of energy $E_{pd} = E_d - E_p$ for hopping electron from 2*p*-orbital of O^{2-} nonmagnetic ion to the 3*d*-orbital of Mn^{2+} magnetic ions. The probability of the hopping process is given by the value of $(t/E_{pd})^2$. The total exchange energy, which is caused by the mixture of ground state and excited state, is then $J(t/E_{pd})^2$. The similar process is also taken into account for the other electron in 2*p*-orbital of O^{2-} nonmagnetic ion. Hence the resultant exchange energy will be $2\,J(t/E_{pd})^2$. If the two Mn^{2+} magnetic ions have the spin S_1 and S_2, the superexchange interaction will be given by follows equation [72-73]:

$$E_{ex} = -2J' \, S_1 \cdot S_2, \text{ where } J' = J(t/E_{pd}S)^2 \qquad (1.2)$$

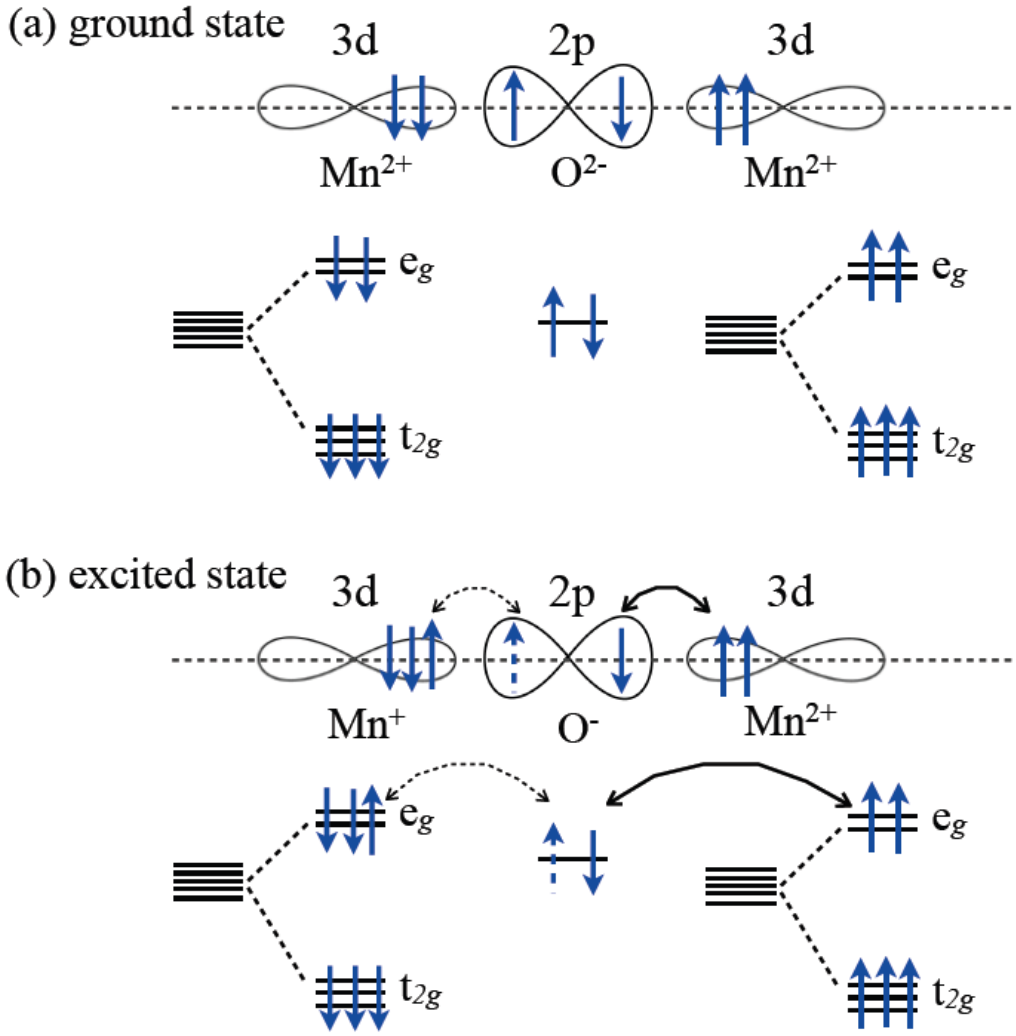

Fig. 1.45. Schematic illustration for the ground state and the excited state in the model of superexchange antiferromagnetic interaction in case of MnO.

This kind of approach is pointed out that still contains uncertainties and complexities. In this approach, the exchange effect realizes in the third order of perturbation theory and the magnitude of this exchange effect implies that this perturbation theory cannot convergent rapidly and the early terms which do not contribute to magnetic effect become rather large. In respond to this difficulty, several other distinct perturbation effects such as double transfer, single transfer integrals and so on have been taken into accounts. However all of these approaches show similar results in the sign and rough order of magnitude and modifications of the wave functions usually bring one of

above effects into the other. These results imply that the physical effect may be rather simpler than expected from the above theories approaches. Another difficulties are the orthogonality dilemma and the choice of wave functions. Normally the calculation starts form a wave function of free ion and the solid is simply put together. The condition of overlap in wave function between ions orbitals is also essential in order to find the antiferromagnetic sign for exchange. However the calculation on overlaps is quite complicated and the reality shows that the set of function on overlap calculation does not work well in some cases. In addition the wave function of a free ion is considered to have modification when put in the solid. This leads to some large arbitrary parameters in the theory approaches [74].

In 1959, Anderson proposed another theory approach for magnetic superexchange interaction in order to solve the difficulties mentioned above [75]. Instead of considering the overlaps of individual ion orbitals, he propose a model in which the molecular orbitals of the combination between *d*-orbitals of magnetic ions and *p*-orbital of nonmagnetic ion can be generated. There are two molecular orbital as the bonding orbital and the antibonding orbital can be expected to be forming. At this stage, it is necessary to consider the mixing of *d*-orbital and *p*-orbital. If we assume there are a localized electron in $3d(z^2)$ orbital (magnetic ion) and electron in $2p(z)$ orbital (nonmagnetic ion), and they behave mixture. We can expect the covalent bonding of $3d(z^2)$ orbital and $2p(z)$ orbital along the z axis. The energy level of $2p(z)$ orbital is thought to be lower than that of $3d(z^2)$ orbital. Hence the bonding function is given by [72]:

$$\varphi_{bonding} \approx \varphi_{p(z)} + \alpha\varphi_{d(z^2)} \qquad (1.2)$$

where α is the mixture parameter. In this case, the value of the mixture parameter is small since the lower energy level of 2p(z) orbital. Two electrons in p-orbital are both expected to stay in this bonding state. The antibonding state then consist of localized magnetic electron of 3d(z^2) orbital. The antibonding function is then:

$$\varphi_{antibonding} \approx -(\alpha + \beta)\varphi_{p(z)} + \varphi_{d(z^2)} \qquad (1.3)$$

where β represents the overlap integral:

$$\beta = \int \varphi_{d(z^2)} * \varphi_{p(z)} dr \qquad (1.4)$$

The bonding function has the lower energy than that of antibonding function and they are orthogonal. The hopping of localized magnetic electron appears from $3d(z^2)$ orbital to antibonding state. The energy difference between the $3d(z^2)$ orbital and antibonding state can be obtained by following estimation [72]. Let us consider a simple eigenvalue problem of non-degenerate case.

The Hamiltonian of the mixture between $3d(z^2)$ orbital and $2p(z)$ orbital are:

$\widehat{H}|p\rangle = E_p|p\rangle + t|d\rangle$ and $\widehat{H}|d\rangle = E_d|d\rangle + t|p\rangle$

The eigenvalue is given by the equation $\widehat{H}|\psi\rangle = E|\psi\rangle$, where the matrix of Hamiltonian is $\widehat{H} = \begin{bmatrix} E_d & t \\ t & E_p \end{bmatrix}$, then the energy of eigenvalues can be determined from below equation:

$$(E_d - E)(E_p - E) - t^2 = 0 \qquad (1.5)$$

The bonding sate is expressed as:

$$|\psi_{bonding}\rangle = |p\rangle - \frac{2t}{E_{pd} + \sqrt{4t^2 + E_{pd}}}|d\rangle = |p\rangle - \frac{t}{E_{pd}}|d\rangle \qquad (1.6)$$

with energy of eigenvalue:

$$E_{bonding} = E_p + \frac{E_{pd}}{2} - \frac{1}{2}\sqrt{E_{pd}^2 + 4t^2} = E_p - \frac{t^2}{E_{pd}} + \frac{t^4}{E_{pd}^3} + \cdots \qquad (1.7)$$

In the meanwhile the antibonding state is given by:

$$|\psi_{antibonding}\rangle = |d\rangle + \frac{2t}{E_{pd} + \sqrt{4t^2 + E_{pd}}}|p\rangle = |d\rangle + \frac{t}{E_{pd}}|p\rangle \qquad (1.8)$$

and the energy of eigenvalue is:

$$E_{antibonding} = E_d - \frac{E_{pd}}{2} + \frac{1}{2}\sqrt{E_{pd}^2 + 4t^2} = E_d + \frac{t^2}{E_{pd}} - \frac{t^4}{E_{pd}^3} + \cdots \qquad (1.9)$$

Therefore the difference of energy is:

$$\Delta E = E_{antibonding} - E_d = \frac{t^2}{E_{pd}} - \frac{t^4}{E_{pd}^3} + \cdots \approx \frac{t^2}{E_{pd}} \quad (1.10)$$

This energy is also equal to the difference of energy between bonding state and 2*p*(*z*) orbital. According the theory approach of Anderson with the model of combination of 3*d*-orbital and 2*p*-orbital, the localized magnetic electron can hop from 3*d*-orbital to the antibonding state. The localized magnetic electron then can have direct magnetic interaction with the other localized magnetic electron in the other antibonding state. The magnetic ordering finally can be realized in the system. The group of three electrons in the admixture of 3*d* orbital and 2*p* orbital can be treated in terms of Slater wave function. The Slater determinant is used to represent the quantum state of group of three electrons [76]:

$$\psi(1,2,3) = \frac{1}{\sqrt{N}} \begin{bmatrix} d_\uparrow(1) - \lambda p_\uparrow(1) & d_\uparrow(2) - \lambda p_\uparrow(2) & d_\uparrow(3) - \lambda p_\uparrow(3) \\ p_\uparrow(1) + \lambda' d_\uparrow(1) & p_\uparrow(2) + \lambda' d_\uparrow(2) & p_\uparrow(3) + \lambda' d_\uparrow(3) \\ p_\downarrow(1) + \lambda' d_\uparrow(1) & p_\downarrow(2) + \lambda' d_\uparrow(2) & p_\downarrow(3) + \lambda' d_\uparrow(3) \end{bmatrix} \quad (1.11)$$

Here *p* and *d* denote the orbitals and the arrows indicate the spin up and spin down states. The numbers 1, 2 and 3 represent the position of electrons and spin coordinates. N is the normalization factor and λ is the arbitrary constant. The value of $\lambda' = \lambda - \beta$, where β is the overlap integral as mentioned earlier. The value of arbitrary constant λ is determined by the orthogonal condition of antibonding and bonding states, which are given by $|d\rangle - \lambda|p\rangle$ and $|p\rangle + \lambda'|d\rangle$, respectively.

The superexchange interaction between localized magnetic electron in 3d-orbital can be described by:

$$-2 J_{eff} S_1 \cdot S_2 \quad (1.12)$$

where the effective exchange interaction $J_{eff} = 2\lambda^2(J_{direct} - t^2/U)$. The term J_{direct} represents the direct exchange interaction between electrons in antibonding states. The term t^2/U describes the charge transfer, where U is the Coulomb repulsive interaction which appear to prevent the transfer of localized magnetic electron to the neighbor sites. The equation 1.12, which describes the superexchange interaction,

seems to have similar spin dependence with the Heisenberg exchange interaction however the difference comes from the term t^2/U.

Some semiempirical rules have been considered by Goodenough, Kanamori and Anderson in order to describe the features of superexchange interaction [70, 74, 75, 77, 78]. These rules perform important application because they can be used to explain magnetic orderings, which relate to superexchange interaction, observed in experimental results of various magnetic compounds. The rules were proposed by Goodenough and Kanamori, and then slightly modified by Anderson. Nowadays these rules are known as Goodenough-Kanamori-Anderson (GKA) rules. These rules are given as bellows [74]:

1. When the two ions have lobes of magnetic orbital pointing toward each other in such a way that orbitals would have a reasonably large overlap integral, the exchange is antiferromagnetic. There are several subcases.

a) When the lobes are $3d(z^2)$ type orbital in the octahedral case, particular in the 180^0 position in which these lobes point directly toward a ligand and each other, one obtains particular large superexchange.

b) When $3d(xy)$-orbitals are in 180^0 position to each other, so that they can interact via $2p(x)$-orbital on the ligand, one again obtains antiferromagnetism.

c) In a 90^0 ligand situation, when one ion has a $3d(z^2)$ occupied and the other a $3d(xy)$, the $2p(x)$ for one is the $2p(z)$ for the other and one expects strong overlap and thus antiferromagnetic exchange.

2. When the orbitals are arranged in such a way that they are expected to be in contact but to have no overlap integral – most notably, a $3d(z^2)$ and a $3d(xy)$ in 180^0 position, where the overlap is zero by symmetry - the rule gives ferromagnetic interaction (however, not usually as strong as the antiferromagnetic one).

There are two important consequences is obtained from these rules. Firstly, in the case of angle formed between two magnetic ions, where have localized magnetic electron in $3d$-orbital, and nonmagnetic ion is 180^0 the strong superexchange antiferromagnetism is observed. Secondly if the angle is 90^0 then it results to superexchange ferromagnetism. This superexchange ferromagnetic interaction is weaker when compared with that of the first case. A simple schematic illustration is

plotted in Fig. 1.46. In the case of 180^0 superexchange interaction, because the overlap of 3*d*-orbitals with 2*p*-orbital realizes in the same orbital (the same direction) then the kinetic energy, which is caused by the virtual transport of magnetic electron, will dominate strong antiferromagnetism. On the other hand, if the 3*d*-orbital overlap with 2*p*-orbital in different direction (one overlaps 2*p*(*x*)-orbital and the other overlaps 2*p*(*y*)-orbital) there is no kinetic energy in this situation. In this case the potential energy gives rise of a weak ferromagnetism.

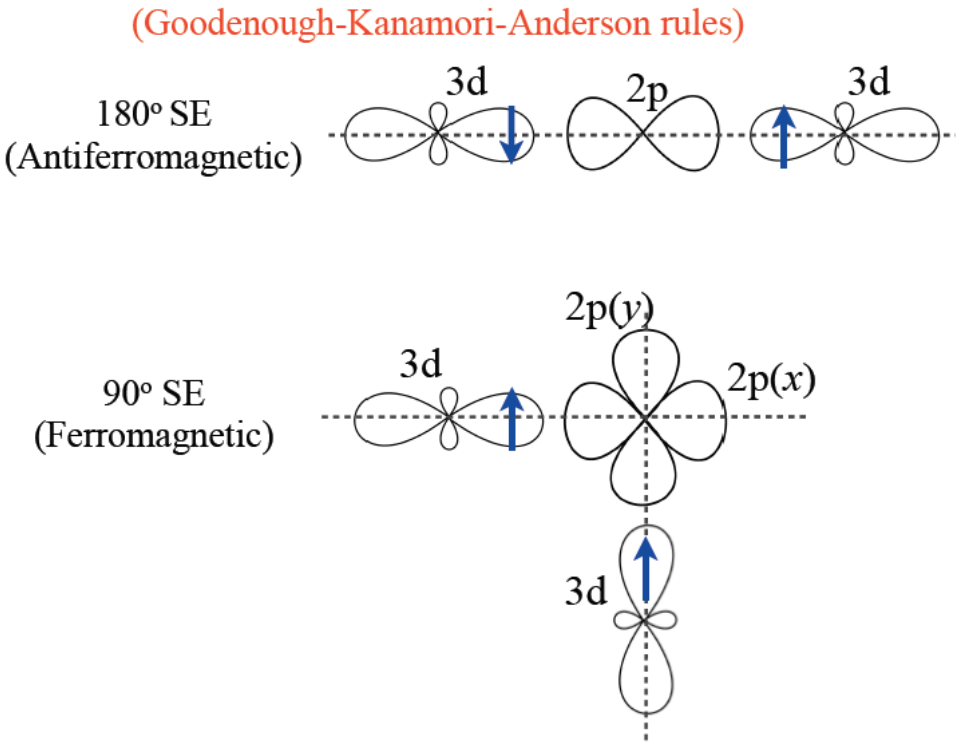

Fig. 1.46. Schematic illustration of 180^0 and 90^0 superexchange interaction (SE stands for superexchange).

1.5 Motivation and purpose of the present studies

In the previous studies, magnetic properties of Na-K alloy clusters in K loaded Na_xK_{12-x}-LSX for lower Na-concentration x (K-rich) samples ($x \leq 4.0$) at various loading density n. As mentioned earlier, the ferrimagnetic properites have been observed in samples K_n/Na_xK_{12-x}-LSX, with x = 4.0, 2.4, 1.5, 1.0 and 0, at specific region of K loading density n. This exhibit the strong dependence of magnetic properties in these samples on the Na-concentration x as well as K loading density n. In particular clear N-type ferrimagnetic properites have been observed for K_n/Na_4K_8-LSX at $6.7 \leq n \leq 8.0$. A model of two non-equivalent magnetic sublattices has been proposed to explain the N-type ferrimagnetic properties at x = 4.0. In this model, one sublattice is expected to realize in supercage clusters network with nearly itinerant ferromagnetic state. The other sublattice is generated by localized magnetic moments in β-cage clusters network. Electrons in supercage and β-cage clusters network can have the antiferromagnetic interaction through the single 6-membered ring window, which connect supercage and β-cage. On the other hand, at lower Na-concentration samples ($x < 4$), the phase of ferrimagnetic properties has a tendency of shifting to higher loading density n. For instance, the ferrimagnetic properites in the samples with Na-concentration x = 2.4, 1.5, 1.0 and 0 appear at K loading density $7.5 \leq n \leq 9.4$, $8.0 \leq n \leq 9.2$, $8.25 \leq n \leq 9.2$ and $8.7 \leq n \leq 9.2$, respectively. The K loading density dependence of ferrimagnetism can be understand by the population of localized magnetic moments in β-cage clusters [65-66].

A phase diagram, which shows the x and n dependence of magnetic properties of K_n/Na_xK_{12-x}-LSX system with x = 4.0, 2.4, 1.5, 1.0 and 0, is plotted in Fig 1.46. According the previous studies, the electronic model, where all of Na^+ cations are assumed to stay in β-cage, has been proposed. The balance of potential between β-cage and supercage, therefore, can be changed with increasing Na concentration. At lower x samples, the β-cage potential is shallow when compare with that of supercage. Higher loading density may be required for the occupation of localized electron in β-cage cluster for the appearance of ferrimagnetic properties. At higher x samples, however, the β-cage potential become deeper due to the larger number of Na^+ cations, the electrons can enter β-cage at lower loading density and the magnetic interaction between localized magnetic electrons in β-cages and itinerant electrons in supercages can be expected. The magnetic properties of sample system systematically vary

depending on both x and n. At higher Na-concentration ($x > 4.0$), the number of Na^+ and K^+ cations will increase and decrease, respectively. How the addition Na^+ cations will influent to the properties of sample system still a question.

In the present study, we have prepared a new sample with Na-concentration $x = 7.3$ ($Na_{7.3}K_{4.7}$-LSX) and $x = 5.1$ ($Na_{5.1}K_{6.9}$-LSX). We have loaded K metal into these samples at various loading density n and generate the Na-K alloy clusters. The magnetic, optical and electrical resistivity measurements have been performed. The sensitivity of magnetic properties depending on Na concentration and how physical properties of system change are expected to clarify.

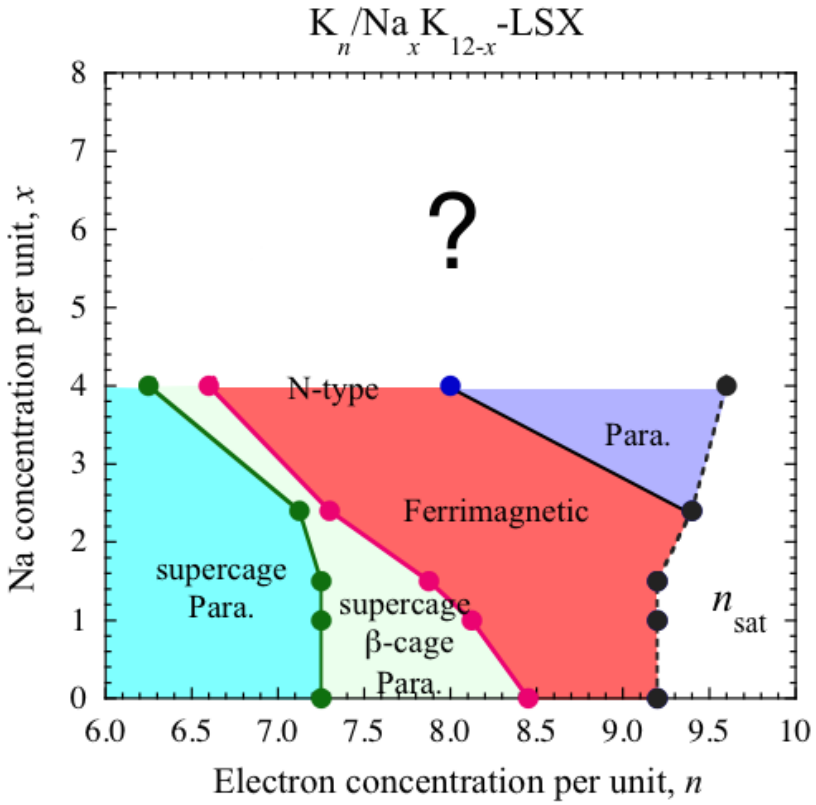

Fig 1.47. Phase diagram of K_n/Na_xK_{12-x}-LSX ($x = 4.0$, 2.4, 1.5, 1.0 and 0).

Chapter II
Experimental procedure

In this chapter, the sample preparation procedure, including the ion-exchange procedure and the alkali metal absorption will be described. In addition, the principle and setup of magnetic, optical and electrical resistivity measurements are also mentioned in details.

2.1 Sample preparation

2.1.1 Ion-exchange procedure

In the present studies, we used the zeolite powder, which has the chemical formula is $Na_xK_{12-x}Al_{12}Si_{12}O_{48}$. ~$w$$H_2O$ (w = 27), where x = 7.3. The sample preparation will be briefly described as follows. We started with a calculated amount of the synthetic zeolite LSX powder, which has the chemical formula per unit of $Na_9K_3Al_{12}Si_{12}O_{48}$. ~$w$$H_2O$ (Na_9K_3-LSX), in order to producing the desired zeolite powder. This starting zeolite powder contains $9Na^+$ and $3K^+$ cations. The number of each kind of cations can be changed by a process called ion-exchange. We put the starting zeolite powder and aqueous solution of KCl in to a glass cup. The Na^+ cations can be partly exchanged by K^+ cations in aqueous solution of KCl. We also adjust the concentration of aqueous solution of KCl in this process in order to obtain the zeolite powder with desired Na concentration. The sample solution in glass cup is stirred many times in few weeks to replace the Na^+ cations in starting zeolite powder by K^+ in KCl. Then we remove the solution, which contains the residual KCl and NaCl after the ion-exchange process. The remaining wet zeolite powder is washed by deionization water couple times in order to ensure that there is no residual KCl and NaCl in final zeolite powder. This wet zeolite powder is then dried at room temperature for a couple weeks. Afterward we obtain the final zeolite powder. The chemical formula of this powder is checked by means of inductively coupled plasma optical emission spectrometry (ICP-OES). The results from chemical analysis show that we obtained zeolite powder with Na concentration to be 7.3, $Na_{7.3}K_{4.7}Al_{12}Si_{12}O_{48}$. ~$w$$H_2O$ (x = 7.3). The diagram of the ion-exchange process is illustrated in Fig. 2.1.

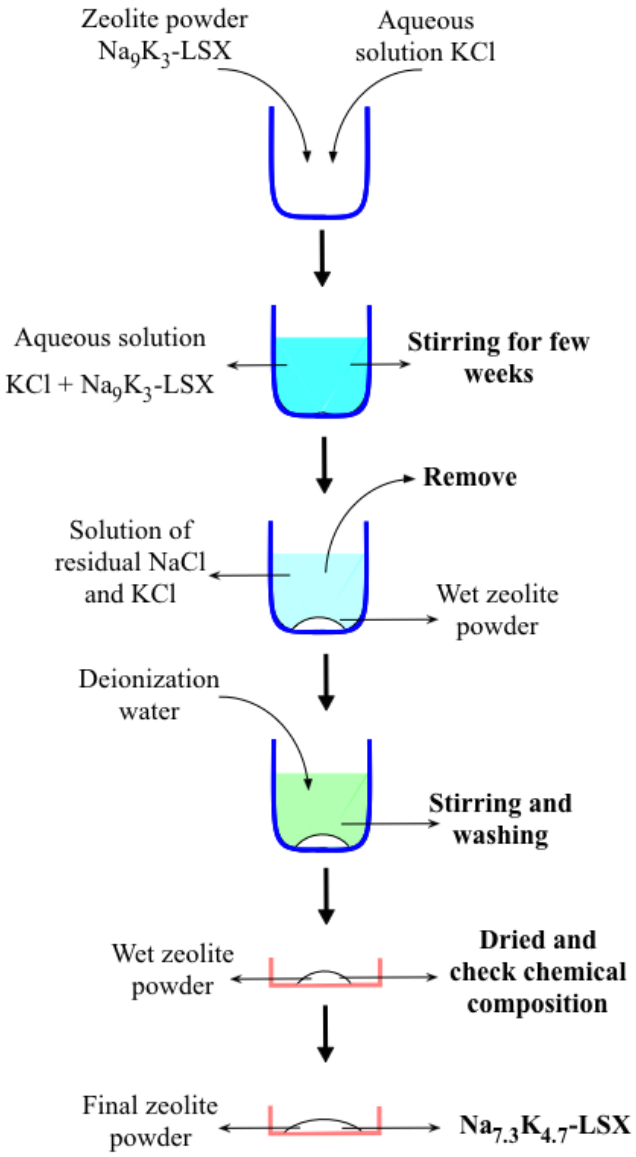

Fig. 2.1. Diagram of the ion-exchange process for zeolite powder with Na concentration $x = 7.3$.

In the case of sample powder or $Na_{5.1}K_{6.9}Al_{12}Si_{12}O_{48}$. ~$w$$H_2O$ (x = 5.1), the ion-exchange process is a bit different. We also started with the powder of Na_9K_3-LSX. However, we remove all of Na^+ cations in this power by KCl to produce the powder of K_{12}-LSX. Afterthat, an amount of NaCl is adjusted together with the powder of K_{12}-LSX to replace the K^+ cations. Finally we obtained the sample powder, which is confirmed by the ICP-OES, with chemical formula of $Na_{5.1}K_{6.9}Al_{12}Si_{12}O_{48}$. ~$w$$H_2O$ (x = 5.1).

2.1.2 Alkali metal adsorption

When the ion-exchange processes finished we obtained the zeolite powders, which contain a lot of water molecules. In the present studies, the potassium was used as guest alkali metal atoms and adsorbed into zeolite powder. Therefore the zeolite powder need to be dehydrated in order to avoid the reaction between alkali metals and water molecules. Afterward alkali metal atoms are adsorbed into dehydrated zeolite powder, the sample then can be abbreviated as Na_xK_{12-x+n}-LSX, where n is the number of the alkali metal atoms loaded in to zeolite LSX, or also called as the K-loading density per β-cage (or supercage). The sample then can be denoted as K_n/Na_xK_{12-x}-LSX hereafter. The sample making procedure can be divided to four steps (a) dehydration, (b) potassium distillation, (c) sample making and (d) potassium adsorption. These steps of sample making procedure will be briefly described in detailed in next section.

Firstly, the ion-exchanged zeolite powder needs to be dehydrated. LSX zeolite powder at this time still contains a lot of water molecules, in order to adsorb potassium we need to remove all water molecules out of LSX zeolite powder to avoid strongly reaction between water and potassium. That is why the dehydration step was carried out. The schematic illustration of the dehydration step is shown in Fig. 2.2 (a). A weighted amount of ion-exchanged zeolite powder was put into a glass tube. This tube was connected with a turbo-molecular pump (TMP) via a rubber tube and liquid nitrogen trap. When the vacuum level displayed on TMP approached to $1x10^{-5}$ Torr, the glass tube was put into an electric furnace. The electric furnace was programmed to increase the temperature up to 500^oC and the glass tube was kept at this temperature for nearly 30 hours. During this time, the water molecules into ion-exchanged zeolite powder were gradually removed. Afterward the glass tube was cooled down to room temperature and sealed off by torch. Then the dehydrated zeolite powder could be stored in glass tube under high vacuum condition. Dehydrated zeolite powder also was measured by Fourier transform infrared spectrometer (FTIR), according to the adsorption strength of water in FTIR spectrum the degree of dehydrated zeolite powder was confirmed.

Fig. 2.2 (b) illustrates the potassium distillation step. The starting potassium is commercial potassium, which is stored into kerosene and partly reacted. This kind of

potassium contains an amount of impurities and cannot be used to load into dehydrated zeolite powder. Hence we must distilled potassium to obtain the high-purity potassium. An amount of commercial potassium was put into a glass tube and connected to a rotary pump through a rubber tube and liquid nitrogen trap. The distillation was carried out by heating potassium with a torch while pumping out with rotary pump. The torch increased the temperature of amount potassium inside the glass tube leading to the vaporization of potassium. The vaporized potassium would move to cooler place inside the glass tube with leaving the impurity behind. A part of glass tube where store the impurity was sealed off by torch and these above steps was repeated for a couple times. Finally, the distillation potassium with high-purity was collected by sealing off the glass tube.

At that time, the ion-exchanged zeolite powder was dehydrated and distillation potassium was also ready to be absorbed into zeolite. They were put into a glove box filled with helium gas. A quartz glass tube was used to keeping the sample. An amount of dehydrated zeolite powder and distillation potassium was put into the quartz glass tube, called sample tube, and connected to another quartz glass tube via a rubber tube. Amount of dehydrated zeolite powder and distillation potassium were also weighted carefully before putting into quartz glass tube in order to obtain the desired K-loading density n. After that the sample tube was brought out of glove box and sealed off by torch with embedding the second quartz glass tube into liquid nitrogen to keep low pressure inside the tubes. Then we obtained the sample tube, which contains a weighted amount of dehydrated zeolite powder and distillation potassium. The schematic illustration of sample making step was shown in Fig. 2.2 (c).

The sample tube was put inside an electric furnace to start the adsorption of distill potassium into dehydrated zeolite powder, as seen in Fig. 2.2 (d). The temperature was set to 150^{o}C and the sample tube was kept under this temperature for 3 to 4 weeks. During this time, the sample was mixed many times to ensure that quite homogeneous K-loaded zeolite is obtained. Depending on the weight of distillation potassium and dehydrated zeolite powder the value of n can be changed from dilute value ($n \sim 0.01$) to saturation value.

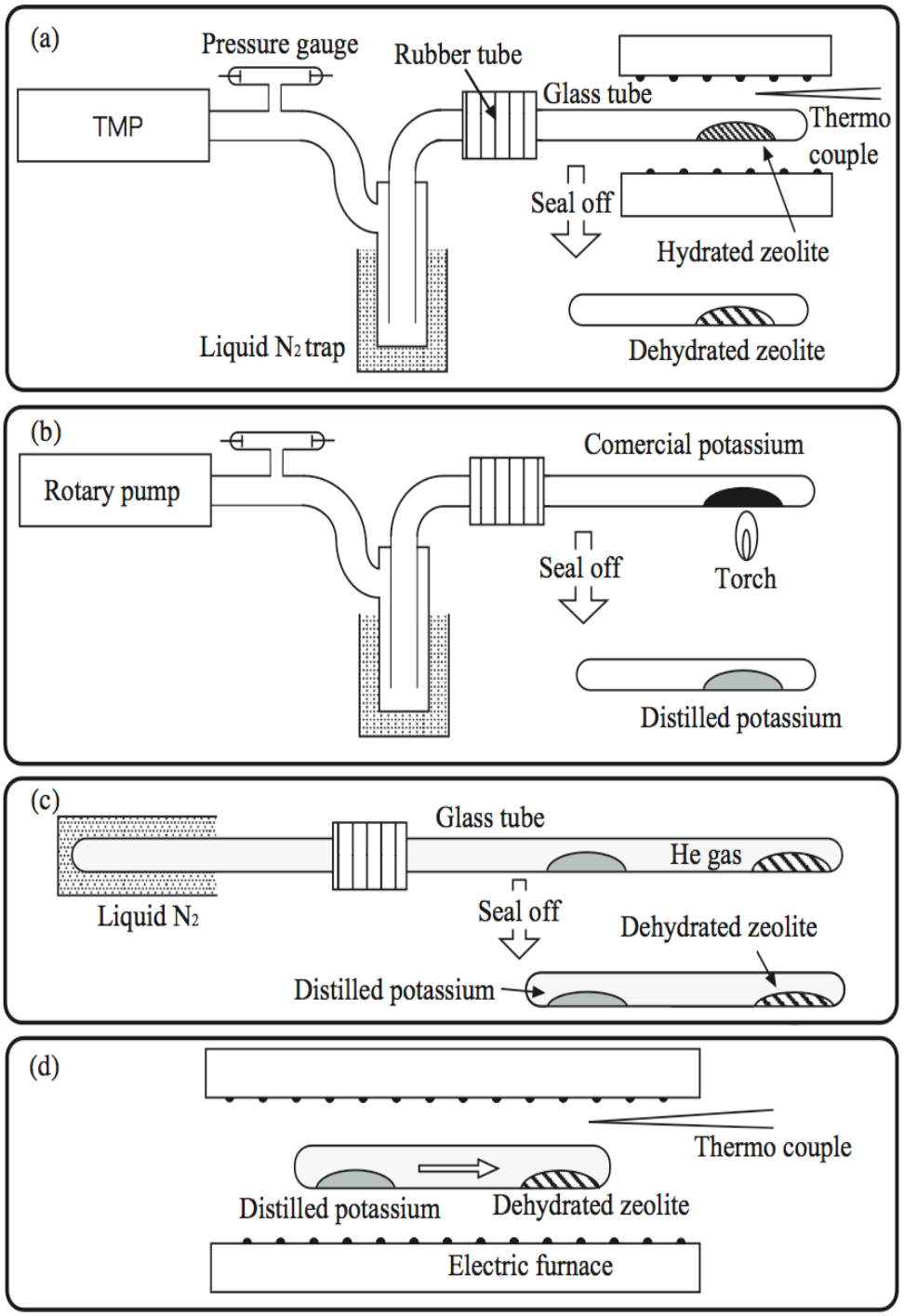

Fig. 2.2. Schematic illustration for sample making procedure: (a) dehydration, (b) potassium distillation, (c) making sample and (d) potassium adsorption.

2.2 Measurements

2.2.1 Magnetic measurement

The magnetization of samples was measured by using the Magnetic Property Measurement System (MPMS) XL, with the applied magnetic field up to 5 Tesla and temperature range of 1.8 – 300 K, made by Quantum Design Company. The MPMS-XL uses Superconducting Quantum Interference Device (SQUID) magnetometer for the measurements. Beside the existence of traditional DC magnetization and SQUID-AC capability, the MPMS-XL was also featured the Reciprocating Sample measurement system. The movement of the sample results in an oscillating AC signal, which is detected by the SQUID sensor. This technique is the combination of the higher sensitivity of performing phase sensitive measurement and the DC SQUID magnetometry to improve the overall sensitivity and noise rejection for DC magnetization measurements.

The SQUID magnetometer consists of a superconducting magnet, a superconducting detection coil, which is coupled inductively to the sample, and a SQUID device connected to the detection coil. The principle of SQUID magnetometer was displayed in Fig. 2.3. The superconducting magnet is a solenoid, which made from superconducting wire, and must be kept at liquid helium temperature in a liquid helium dewar. The applied magnetic field was produced along the axial cylindrical bore of the coil and basically the magnitude of magnetic field can be changed within 5 – 18 Tesla for commercial devices. The superconducting detection coil is a single piece of superconducting wire and placed in the applied magnetic field region of the superconducting magnet. The SQUID device has high sensitivity due to its response to a fraction of the flux quantum. This SQUID device was made from a thin film, which functions as an extremely sensitive current-to-voltage converter.

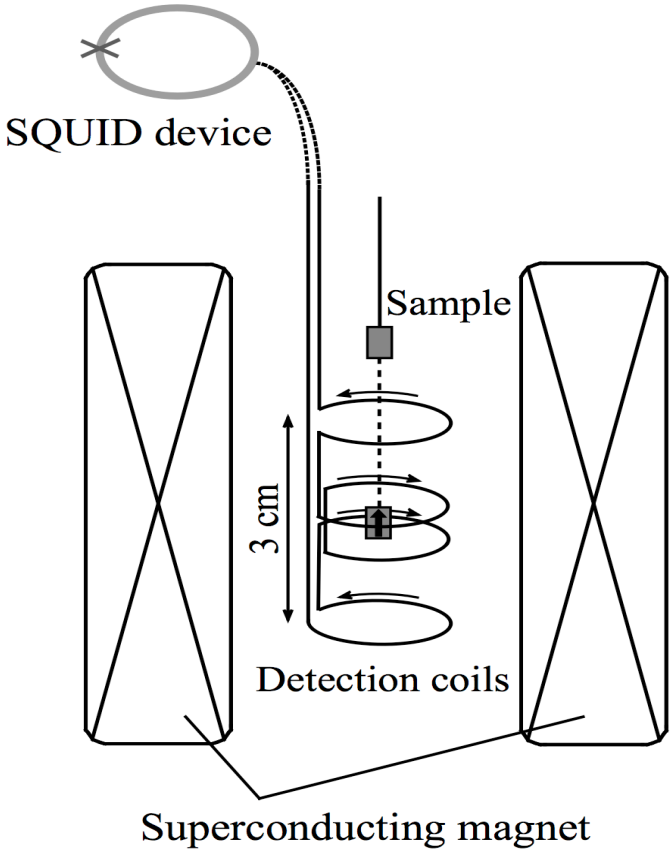

Fig. 2.3. Schematic illustration of principle of SQUID magnetometer.

In order to determine the magnetic moment of the sample, it was oscillated long the symmetry axis through a region of the detection coil. The magnetic moment of samples induces an electric current inside the detection coil. This leads to the changing of magnetic flux in the detection coil. The persistent current in the detection coil was changed and causes the variation of out put voltage, which proportional with the magnetic moment of the samples. The observed data was fitted with the expected curve of a dipole moment by software, in order to determine the dipole strength, and estimate the magnetic moment. This means the sample should be small enough to be approximated as a point magnetic dipole. The ideal response signal from output SQUID voltage has the symmetrical shape about the center of detection coil as seen in Fig. 2.4.

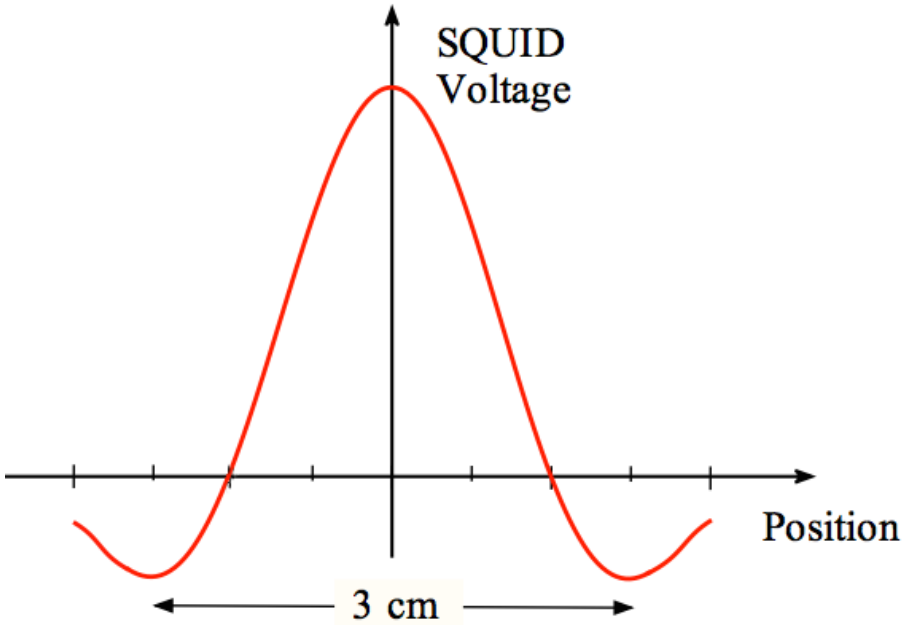

Fig. 2.4. The ideal SQUID response signal.

The measurement was carried out by the Reciprocating Sample Option (RSO) mode. The advantage of the RSO measurement is performed using a servo motor, which rapidly oscillates the sample. While in the DC measurements, sample is moved through the detection coil in discrete steps. Therefore the RSO measurement has the sensitivity of about 5 x 10^{-9} emu [79]. The RSO measurement has two configurations: Center or Maximum modes, all magnetic measurements in this thesis were done using the Center mode. Center mode used large oscillations around the center point of the detection coil. This mode also takes a long time but the sample always remains properly located and a large number of measurements are observed.

An *i*Helium 3 option attached to MPMS can be used to measure the properties of samples at lower temperature below 2K. The lowest temperature can be obtained down to 0.5 K.

The sample powder is usually stored in a quartz glass tube. It needs to be mounted to the sample rode with the compatible length before inserting into the MPMS. The mounting principle was shown in Fig. 2.5.

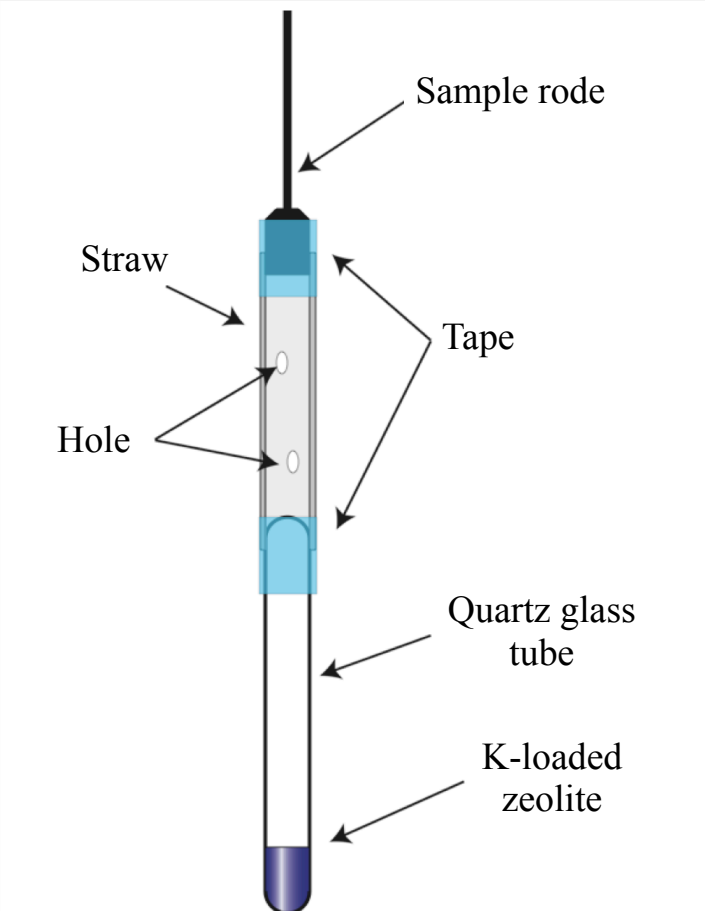

Fig. 2.5. Schematic illustration of sample mounting step in the magnetic measurement.

2.2.2 Optical measurement

In the present studies, the diffuse reflection spectrum of samples was measured by using an FTIR spectrometer and a UV-VIS-NIR spectrometer. The photon energy range of FTIR spectrometer and UV-VIS-NIR spectrometer are 0.3 - 0.5 eV and 0.5 – 6.0 eV, respectively. All measurements were carried out at room temperature and the samples were stored in a quartz glass tube because of their air sensitively.

In near infrared region, where photon energy of 0.3 – 0.5 eV, the spectra were measured by Fourier transform infrared (FTIR) spectrometer. Its model is MAGNA 550 and delivered by Nicolet Instrument Corporation. FTIR spectrometer consists of three basic components: infrared source (halogen lamp), interferometer and detector. The detector of FTIR spectrometer is mercury cadmium telluride (MCT). It is a

photon detector that depends on the quantum nature of the radiation and also exhibits very fast responses. In general, MCT detector must be maintained at liquid nitrogen temperature. The schematic diagram of FTIR spectrometer was illustrated in Fig. 2.6.

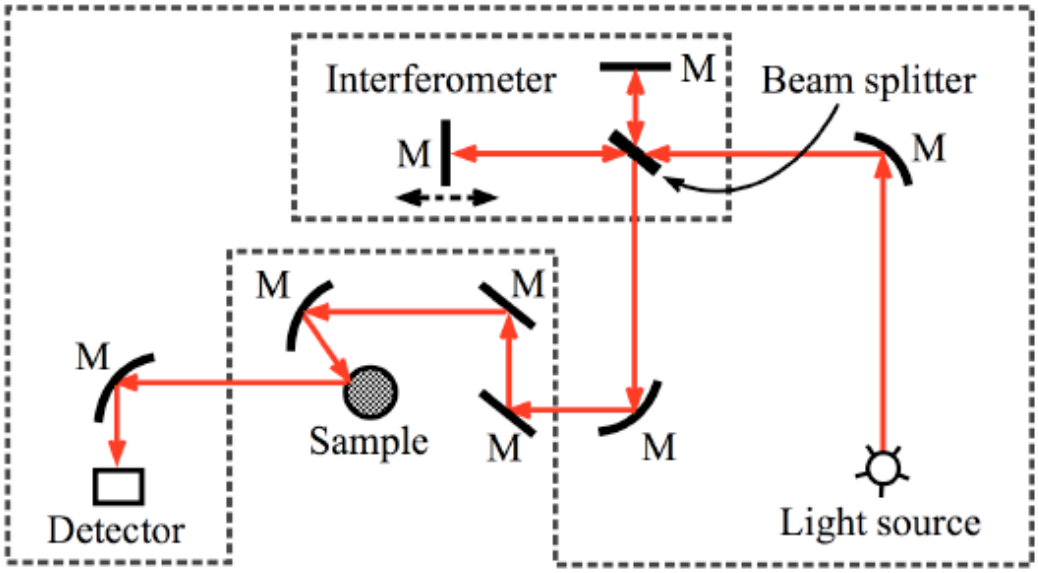

Fig. 2.6. Schematic illustration of Nicolet FTIR spectrometer.

The infrared source emits a broad band of different wavelength of infrared radiation. This infrared radiation passes through an interferometer, which modulates the infrared source. The used interferometer is a Michelson type plane mirror interferometer. It consists of three active components: a fixed mirror, a moving mirror and a beamsplitter. Fixed mirror and moving mirror are perpendicular to each other. Infrared radiation from the source is collected and collimated before it strikes the beamsplitter. The beamsplitter will transmits one half of the infrared radiation and reflects the other half. After that, both transmitted and reflected beams strike mirrors, where these beams are reflected back to the beamsplitter. That means one half of the infrared radiation has first been reflected from the beamsplitter to the moving mirror and then back to the beamsplitter. The other half of infrared radiation has first gone through the beamsplitter and then reflected from the fixed mirror back to the beamsplitter. When these two optical paths are reunited, the interference will occur at

the beamsplitter because of the optical path difference cause by the scanning of the moving mirror. The resulting beam then passes through the sample and is eventually focused on the detector. The optical path length difference between the two optical paths of Michelson interferometer is two times the displacement of the moving mirror. The interference signal, which measured by the detector, is a function of the optical path length difference and called the interferogram. This interferogram contains information over the entire infrared region to which the detector is responsive. A mathematical operation named Fourier transformation will convert the interferogram to the final infrared spectrum.

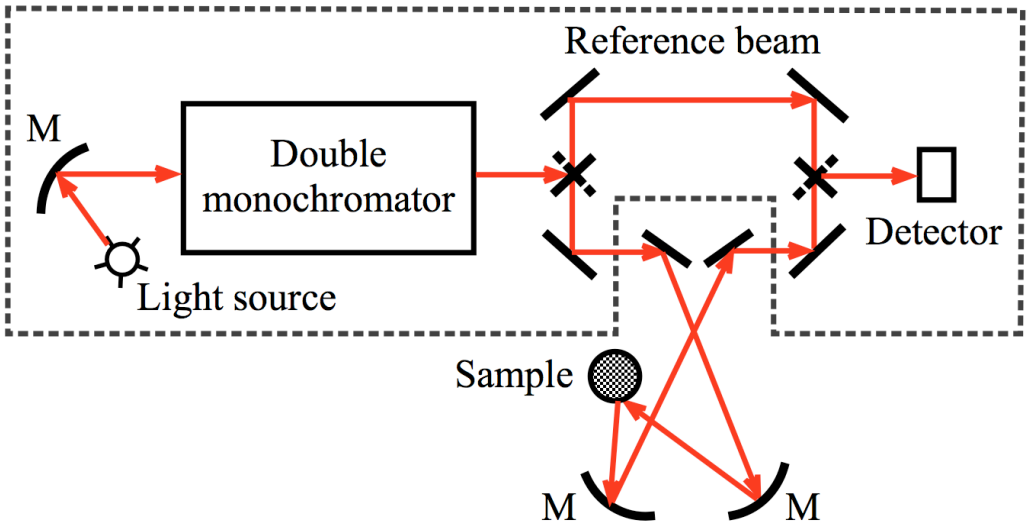

Fig. 2.7. Schematic illustration of Varian Cary 5G spectrometer.

The measurement in UV-VIS-NIR region with photon energy range of 0.5 – 6 eV was carried out by Cary 5G spectrometer, which manufactured by Varian company. It also consists of three basic components: light source, double monochromator and detector. Not similar as in the case of FTIR spectrometer, the light source of Varian Cary 5G spectrometer contains a deuterium lamp and a halogen lamp with filament made from tungsten, which is UV and VIS-NIR radiation source, respectively. The detector is photomultiplier for UV-VIS and lead sulfide for NIR. Firstly, the radiation from light source is directed to the mirror and then reflected to the double monochromator. Only narrow band of light is passed the double monochromator. Then the light will go through a mirror system in order to focus on the sample before reflected to the

detector. The observation data can be used to calculate the absorption or reflectance spectrum of the sample. The schematic illustration of Varian Cary 5G spectrometer was shown in Fig. 2.7.

The reference samples for Nicolet FTIR and Varian Cary 5G spectrometer are ground KCl or KBr powder, they are also kept into the same quartz glass tube as the samples. In order to obtain the absolute value of the diffuse reflection of sample, the reference samples were measured. The illustration for direction of the reflected light from sample, when it is measured, was shown in Fig. 2.8.

Optical adsorption spectra were obtained by using the Kubelka – Munk function [80]. It is used as a method to convert the diffuse reflectance spectra obtained from weakly absorbed sample. That means the Kubelka – Munk function is applicable when the transmitted light is sufficiently stronger than the reflected light by each powder particle. The Kubelka – Munk function is given as follows:

$$\frac{K}{S} = \frac{(1-r)^2}{2r} \qquad (2.1)$$

Where K is absorption coefficient; S is scattering coefficient and r is diffuse reflection.

For the middle to high absorbed samples, the sum of reflection R and transmission T is given as following formula:

$$R + T = \frac{4r}{(1+r)^2} \qquad (2.2)$$

Equation (2.2) is valid in any case of powder material with isotropic absorption coefficient and the particle size is greater than the wavelength. If the absorption is strong, then the transmitted light of each powder particle is extremely weak compared with the reflected light. Therefore, the obtained spectrum can be assigned for the reflection [37], and the left hand side in equation (2.2) should be replaced by R.

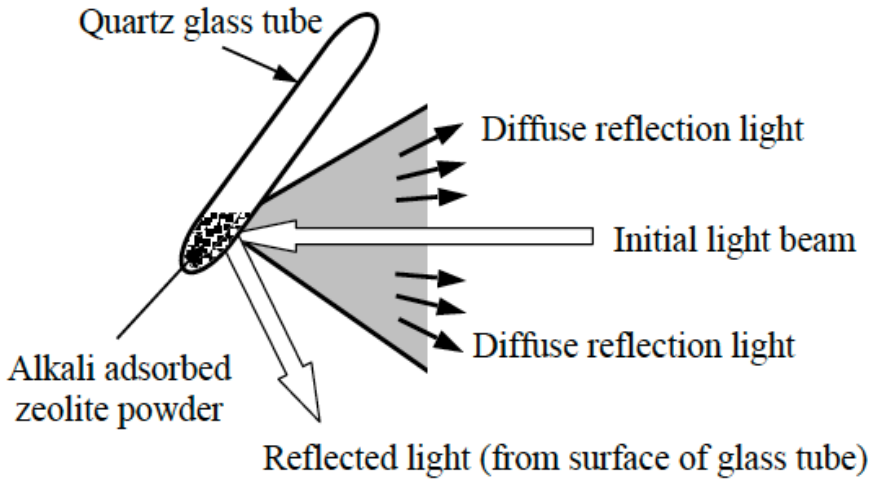

Fig. 2.8. Schematic illustration of the direction of the reflected light from sample.

2.2.3 Electrical resistivity measurement

2.2.3.1 Measurement setup

For the electrical resistivity measurement, the sample powder is put into a sample space between two gold electrodes with the diameter of 4 mm and cover by a quartz glass tube with diameter around 5 mm. The gold electrodes are connected to the coaxial wire and base made from zirconium. Afterward all above parts are put into a sample cell, which made of BeCu alloy, and pressed at a compression force of ~ 1 MPa as displayed in Fig. 2.9.

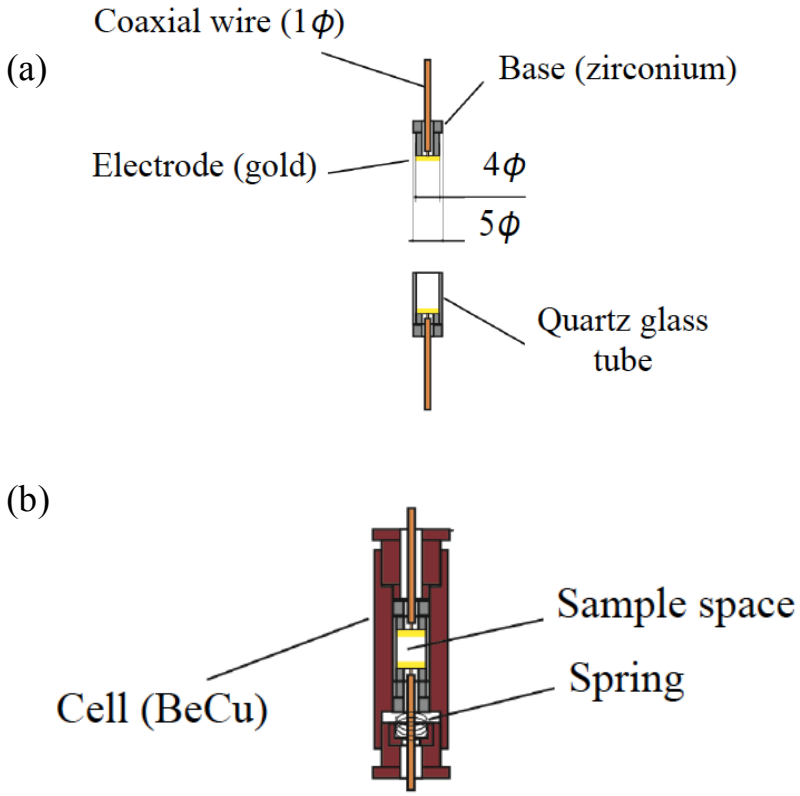

Fig. 2.9. Schematic illustration of the setup of sample space (a) and sample cell (b) for electrical resistivity measurements.

The sample cell is then sealed into a handmade airproof cell because the sample powder is extremely air sensitive. The schematic illustration of sample cell setup in handmade airproof cell is shown in Fig. 2.10. Above procedures are carried out inside a glove box filled with pure He gas containing less than 1ppm of O_2 and H_2O. The cell is then set in a sample chamber of Physical Property Measurement System (PPMS, Quantum Design). The sample temperature is controlled between 10 and 300 K. Impedance measurements of the cell involving the sample is performed by using

the 4-terminal method with an Agilent E4980A LCR meter in the frequency range from 20 Hz to 2 MHz and Dc. The value of resistivity is obtained by multiplying the dimensional factor (area/thickness) of compressed powder.

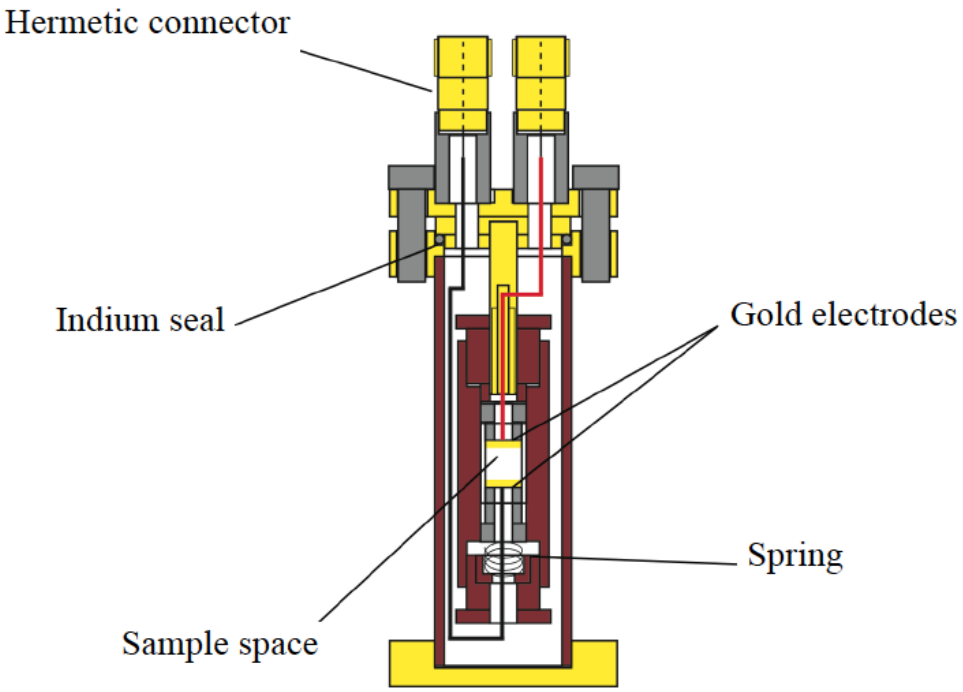

Fig. 2.10. Schematic illustration of the setup of sample cell inside a handmade airproof cell in electrical resistivity measurements.

2.2.3.2 Analysis method

The reliability of DC resistivity can be confirmed by analyzing the frequency dependence of the complex impedance by using Cole – Cole plots. Cole – Cole plot displays the real and imaginary parts of impedance depend on frequency. For example, if we have a circuit contains a resistor (resistance value R) paralleled with a capacitor, Cole – Cole plot will draw a semicircle of radius $R/2$. The illustration for the resistor capacitor parallel circuit with correspond impedance is shown in Fig. 2.11 (a). In addition and example of Cole – Cole plot for the resistor capacitor parallel circuit with the value R = 100 kΩ and C = 50 pF is shown in Fig. 2.11 (b), the blue arrow indicates the frequency increasing direction. By using Cole – Cole plot the DC resistivity can be confirmed by comparison with the real part of complex impedance

when imaginary part down to zero by extrapolating the semicircle at low frequency region.

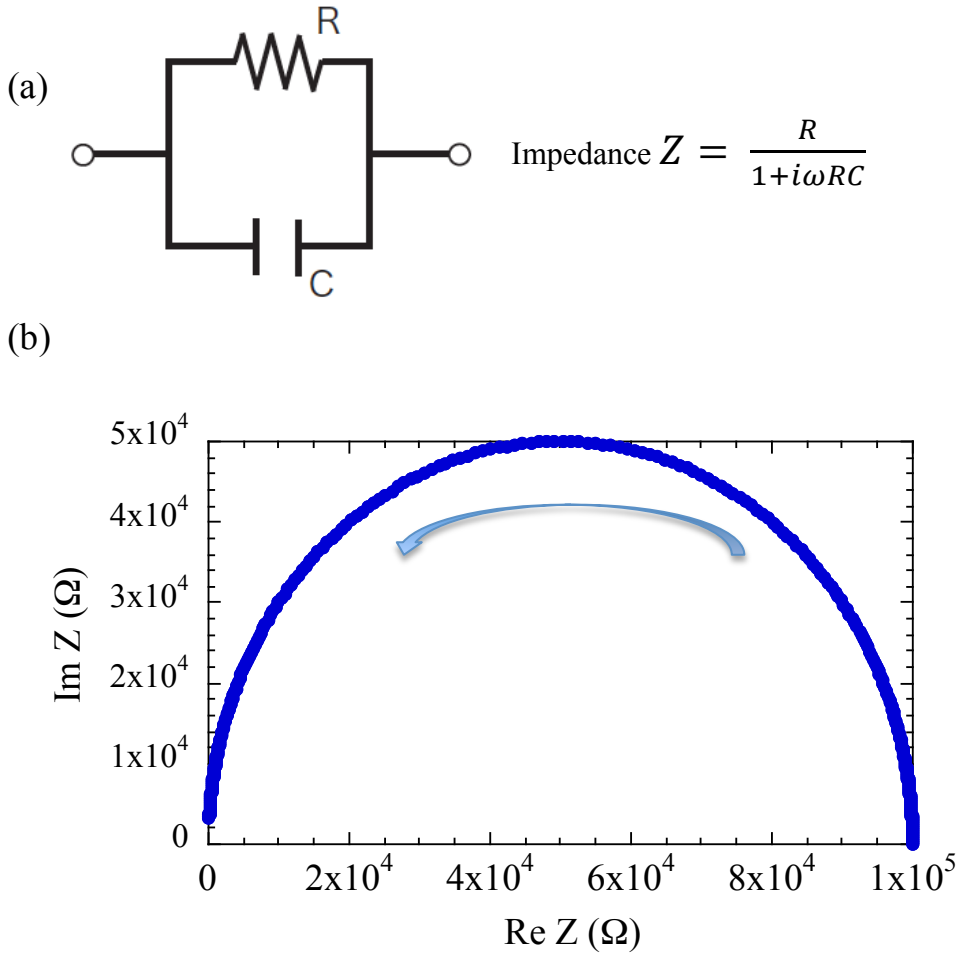

Fig. 2.11. Parallel circuit of a resistor with resistance R and a capacitor with capacitance C (a) and an example of the Cole – Cole plots show semicircle shape (b).

From the experimental results, in some cases Cole – Cole plots do not show the perfect shape of semicircle. This behavior may be caused by the failure in display the real component over wide frequency range, which comes from the natural distribution of real component or relaxation time distribution. In this case the frequency dependence can be seen as a series connection of an equivalent circuit, as seen in Fig. 2.11 (a). The function of impedance corresponds to the relaxation element may be used to fit the data:

$$Z = \frac{\mathrm{R}}{1+ (i2\pi\tau f)^{\phi}} \quad (2.9)$$

Z: Impedance

R: Resistance

τ: relaxation time (τ = RC: C is capacitance)

ϕ: parameter for the distribution of relaxation time

The parameter for the distribution of relaxation time dependence of the shape of semicirle in Cole – Cole plot is displayed in Fig. 2.12. When ϕ = 1, Cole – Cole plot draws perfect semicircle. While the shape of semicirle changes when ϕ takes values between less than 1.

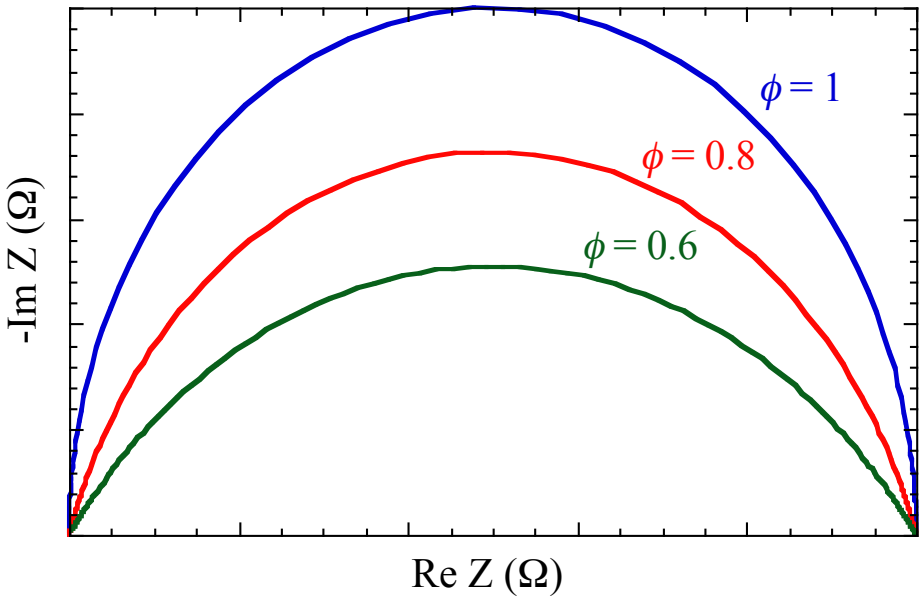

Fig. 2.12. Cole – Cole plots depend on the parameter for the distribution of relaxation time in equation 2.9.

The observed value of resistivity is about one or two orders of the magnitude higher than the actual value due to the constriction resistance at the connection between powder particles. Let assume that we have two powder particles, with cubic shape and length is A, which connect to each other particles through a thin area by length a. The powder particle has the resistivity ρ. Hence, the constriction resistance is given by $R_C = \rho/a$ ($a << A$). An equivalent circuit, which contains resistor parallel to a capacitor, in the case of constriction resistance is shown in Fig. 2.13 (a). In whole system we have

several powder particles as well as connection. The constriction resistance will dominate the system. Hence the system can be seen as a series of equivalent circuits as illustrated in Fig. 2.13 (b). According to above assumption, the total DC resistivity may be approximation as (R_C x $1/A$) / ($1/A^2$) = ρ x A/a, where $1/A$ is the number of connection per unit length and $1/A^2$ is the number of chains in the powder particles system. The observed total DC resistivity A/a times higher than the actual value.

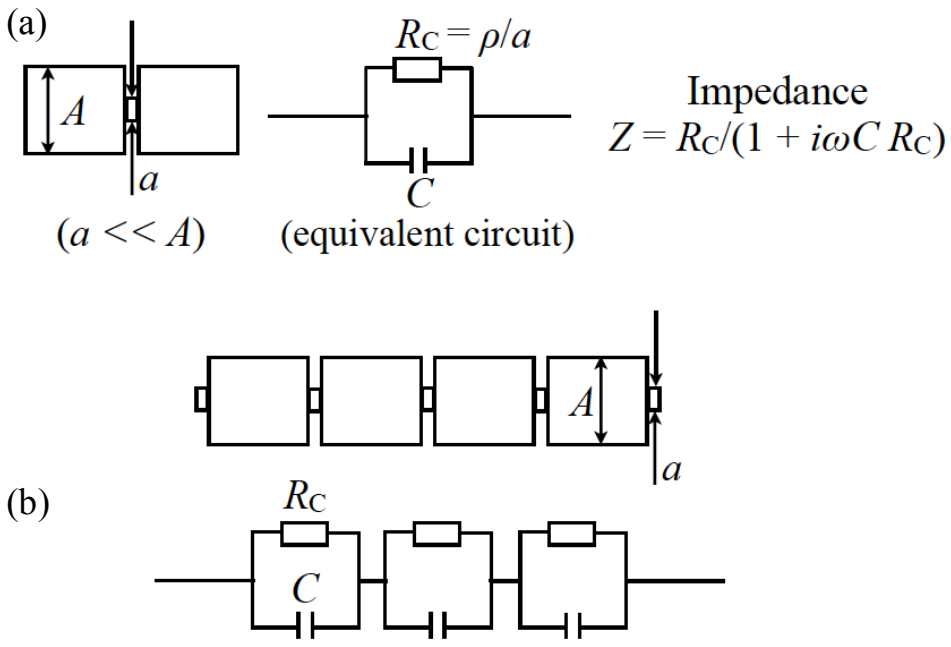

Fig. 2.13. Simple illustration for constriction resistance and equivalent circuit (a) and series of equivalent circuits correspond to the real case (b).

Chapter III

Experimental results and discussion on $K_n/Na_{7.3}K_{4.7}$-LSX (x = 7.3)

The samples of K-loaded $Na_{7.3}K_{4.7}$-LSX (x = 7.3) have been successful prepared at various loading densities from dilute one to the saturated value. The physical properties of these samples have been investigated by the optical, magnetic and electrical resistivity measurements. In this chapter, the experimental results and discussion on $K_n/Na_{7.3}K_{4.7}$-LSX (x = 7.3) will be introduced.

3.1 Experimental results of $K_n/Na_{7.3}K_{4.7}$-LSX (x = 7.3)

3.1.1 Optical properties

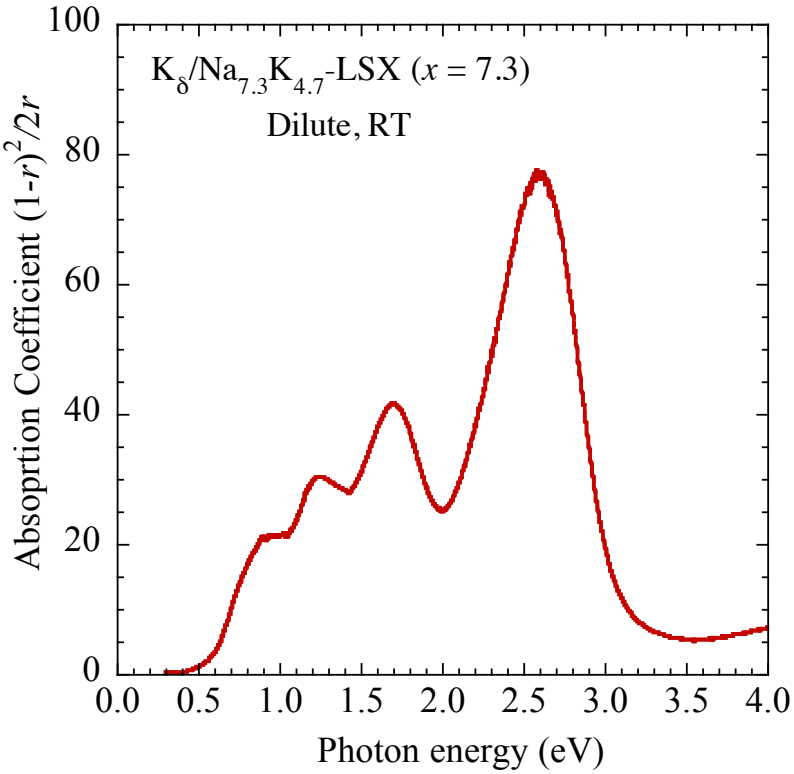

Fig. 3.1. Absorption spectrum measured at room temperature for dilute sample $K_\delta/Na_{7.3}K_{4.7}$-LSX (x = 7.3).

The optical excitation processes from ground state to excited sates are normally observed in the optical absorption and reflectance spectra. From these spectra, the reliable information of electronic states can be extracted. In the case of zeolite, the optical absorption and reflection spectra are usually exhibit the optical excitation of electron confined in clusters. The excitation processes of these electrons appear in the IR-VIS-UV region. Another electrons, which are located in the zeolite framework, also behave the optical excitation. The optical excitation of these electrons and cation cores, however, appear in the vacuum UV region and is not displayed in the present spectra at IR-VIS-UV region.

The diffuse reflectivity for the dilute sample of $K_\delta/Na_{7.3}K_{4.7}$-LSX (x = 7.3), where the loading density δ is much lower than unity (δ << 1), was measured at room temperature and then transformed into absorption coefficient by Kubelka – Munk function (equation 2.1). The absorption spectrum of this sample is shown in Fig. 3.1. At lower photon energy region < 2 eV, we observed a structure with continuous absorption bands. In these continuous absorption bands, we can see a small shoulder at ≈ 0.9 eV. In addition two clear absorption bands appear at ≈ 1.1 and ≈ 1.7 eV. At higher photon energy level, there is a significant absorption band at ≈ 2.6 eV.

In order to understand the absorption spectrum of $K_\delta/Na_{7.3}K_{4.7}$-LSX (x = 7.3) at dilute K-loading density, it is necessary to consider it together with the other systems of zeolite LSX. The comparison of the absorption spectra between dilute samples of K_δ/K_{12}-LSX (x = 0), $K_\delta/Na_{4.0}K_{8.0}$-LSX (x = 4.0), $K_\delta/Na_{7.3}K_{4.7}$-LSX (x = 7.3) and Na_δ/Na_{12}-LSX is plotted in Fig. 3.2. The values of δ are not common in these samples. The similar continuous absorption bands at the photon energy < 2 eV are observed in K_δ/K_{12}-LSX (x = 0), $K_\delta/Na_{4.0}K_{8.0}$-LSX (x = 4.0) and $K_\delta/Na_{7.3}K_{4.7}$-LSX (x = 7.3).

Another significant absorption band appears at ≈ 2.6 eV for the case of $K_\delta/Na_{7.3}K_{4.7}$-LSX (x = 7.3). This band can be compared with that of Na_δ/Na_{12}-LSX. The observed absorption band at ≈ 2.5 eV for the case of Na_δ/Na_{12}-LSX can be explained by the resonant optical excitation of s-electron of the clusters, which is formed in β-cages [59]. If we consider a spherical infinite well potential with diameter of 7.5 Å for β-cage, there is an allowed optical excitation of a free electron from 1s- to 1p-state with energy of 2.8 eV. This value is quite comparable with the observed absorption band at ≈ 2.5 and ≈ 2.6 eV for Na_δ/Na_{12}-LSX and $K_\delta/Na_{7.3}K_{4.7}$-LSX (x = 7.3), respectively.

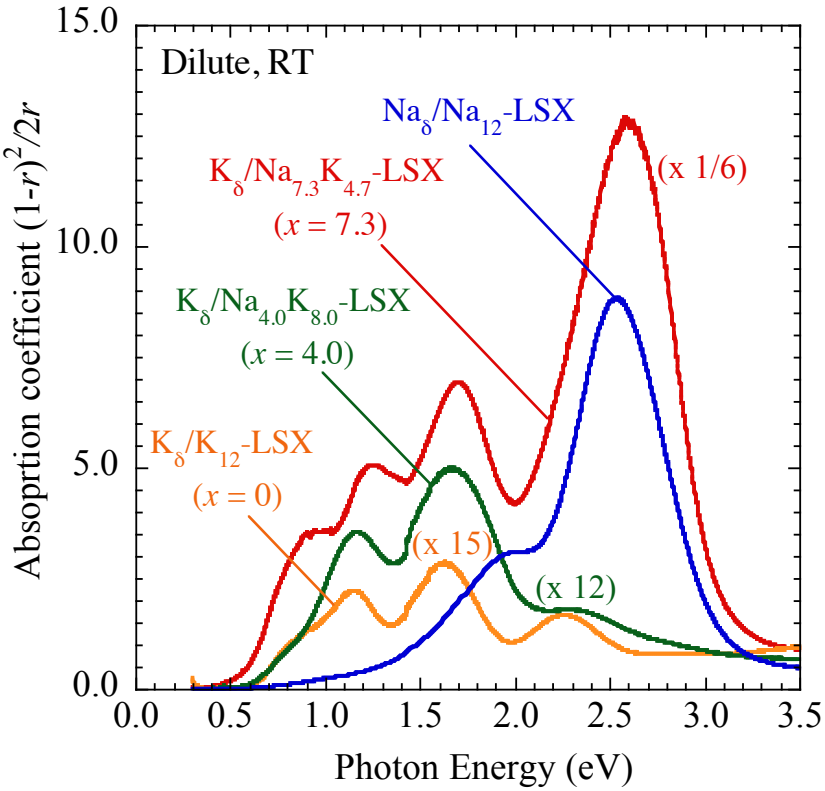

Fig. 3.2. Comparison of optical absorption spectrum measured at room temperature for dilute sample K_δ/K_{12}-LSX (x = 0), $K_\delta/Na_{4.0}K_{8.0}$-LSX (x = 4.0), $K_\delta/Na_{7.3}K_{4.7}$-LSX (x = 7.3) and Na_δ/Na_{12}-LSX.

Moreover, an energy of 0.9 eV is estimated for an allowed optical excitation of a free electron from 1s- to 1p-state if we assume a spherical infinite well potential with diameter of 13 Å for the case of supercage. Because the supercages are connected to each other by wide window of 12-membered ring then the electronic potential can be largely deformed form the spherical symmetry to the T_d-symmetry, which does not have inversion symmetry at the center of cage. Therefore, 1s, 1p and 1d states are expected to have the hybridization. This leads to the appearance of optical excitation from the A_1 (s-like) ground state to two T_2 (p- and d-like) states in the T_d-symmetry. If an unbalanced distribution of cations is assumed in supercages, the effective potential for s electrons has symmetry lower than T_d. At this stage E-like state can be excited form the A_1-like ground state. The E-like and T_2-like state also will be split

into more numbers. The origin of continuous absorption bands observed in K_δ/K_{12}-LSX (x = 0), $K_\delta/Na_{4.0}K_{6.9}$-LSX (x = 4.0), $K_\delta/Na_{7.3}K_{4.7}$-LSX (x = 7.3) at lower photon energy region, < 2 eV, can be assigned to the formation of those clusters in supercages. Base on the experimental results of absorption spectrum of $K_\delta/Na_{7.3}K_{4.7}$-LSX (x = 7.3) at dilute loading density and also the comparison with other systems, clusters are thought to be formed in both supercages and β-cages in the case of $K_\delta/Na_{7.3}K_{4.7}$-LSX (x = 7.3) because we observed the structure with continuous absorption bands at lower photon energy region, < 2 eV, and the other absorption band at ≈ 2.6 eV simultaneously.

The optical reflectance spectra for $K_n/Na_{7.3}K_{4.7}$-LSX (x = 7.3) at various K-loading densities n measured at room temperature is displayed in Fig. 3.3. At low loading density samples, there is no remarkable reflection band. However, with increasing the loading density, reflection bands at ≈ 2.4 eV are observed at samples with n = 4.0 and 7.6. At higher loading density sample with n = 8.2, a new reflection band appears at ≈ 2.8 eV. This reflection band grows and exhibits similar spectral intensity at higher loading density samples $8.4 \leq n \leq 9.5$. For the highest loading density sample with n = 9.7, the reflection band at ≈ 2.8 eV shows a slight increasing in its spectra width. In addition, we also observed reflection bands at ≈ 0.7 eV for all samples with $4.0 \leq n \leq 9.7$.

These reflection bands at < 2 eV are mainly assigned to the excitation of s-electron in clusters at supercages, which similarly observed in the optical absorption spectra of dilute sample but the number of s-electron in supercage of samples in the present reflectance spectrum is larger than unity. On the other hand, the reflection bands at ≈ 2.4 and ≈ 2.8 eV can be basically attributed to the optical excitation of s-electron from 1s to 1p state of β-cage clusters with different cation distributions. Detailed discussion on this issue will be given later in this chapter. In addition, the sharp structures are also observed in higher loading density samples at ≈ 0.45 eV is caused by an undesired OH absorption of the quartz glass tube.

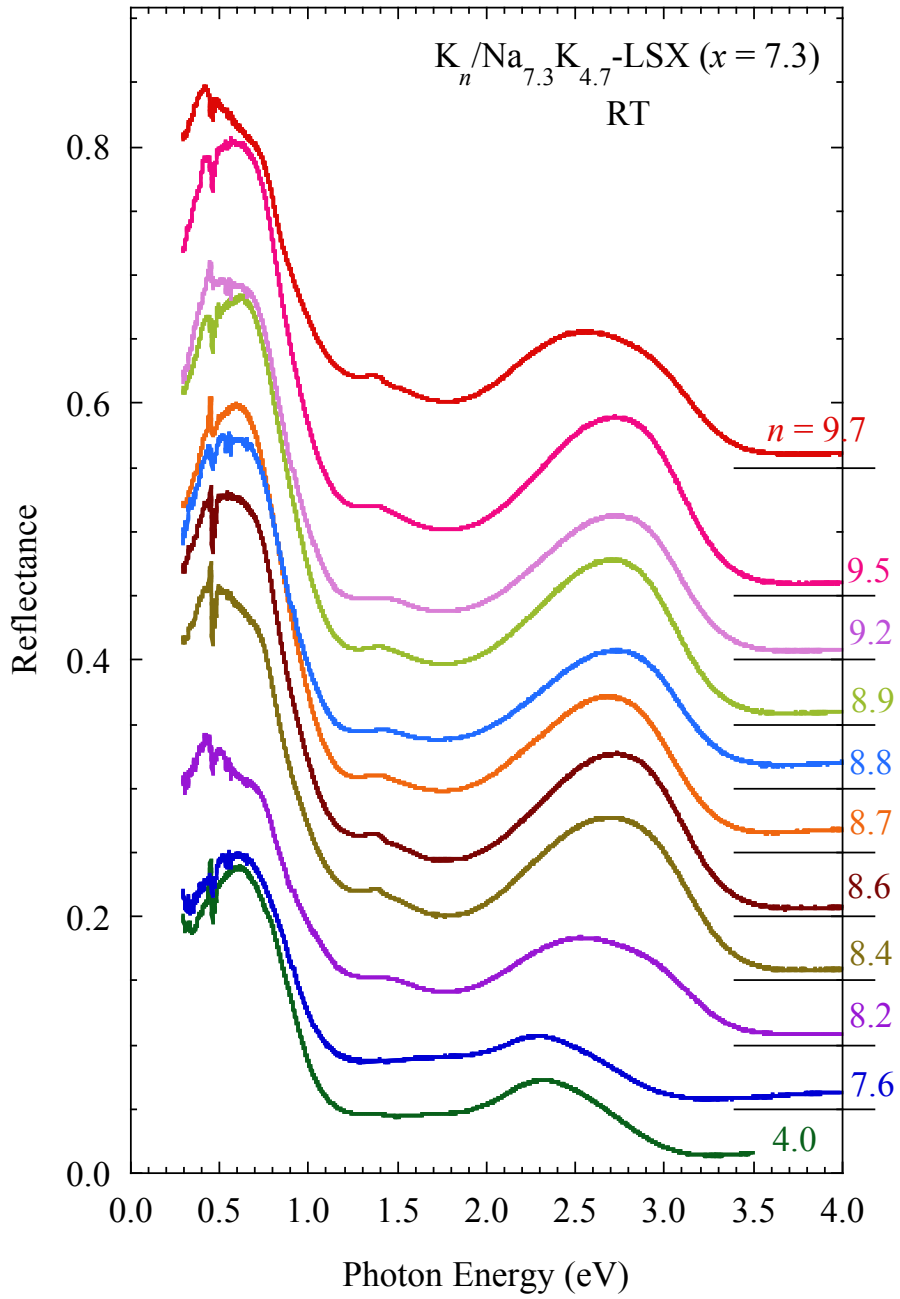

Fig. 3.3. Optical reflectance spectra of $K_n/Na_{7.3}K_{4.7}$-LSX (x = 7.3) measured at room temperature for various loading densities n.

3.1.2 Magnetic properties

The measurements of the temperature dependence of magnetization under a weak and strong applied magnetic field, the magnetization curves have been carried out for $K_n/Na_{7.3}K_{4.7}$-LSX (x = 7.3) at various K loading density n.

The temperature dependence of magnetization measured under a weak applied magnetic field of 10 Oe for $K_n/Na_{7.3}K_{4.7}$-LSX (x = 7.3) at lower K-loading densities n is plotted in Fig. 3.4. As seen in the figure, these samples, $0.4 \leq n \leq 8.4$ and $n = 9.7$, exhibit paramagnetic behaviors of the temperature dependence of magnetization. The magnetization shows paramagnetic values, in the order of 10^{-4} G, in whole temperature range. These results indicate that the samples at $0.4 \leq n \leq 8.4$ and $n = 9.7$ are paramagnetic samples.

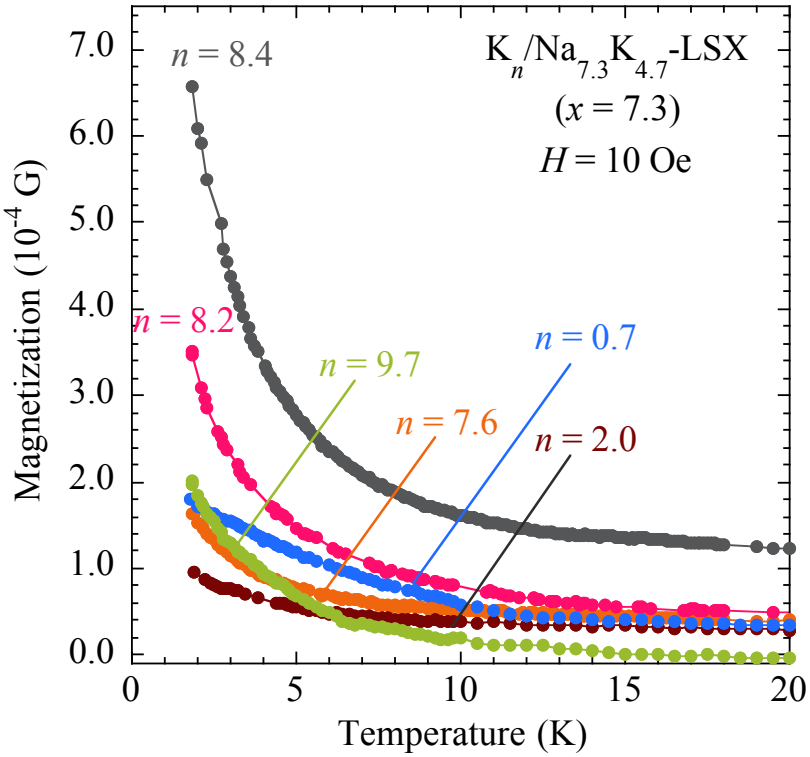

Fig. 3.4. Temperature dependence of magnetization in $K_n/Na_{7.3}K_{4.7}$-LSX (x = 7.3) measured under applied magnetic field of 10 Oe for paramagnetic samples $0.4 \leq n \leq 8.4$ and $n = 9.7$.

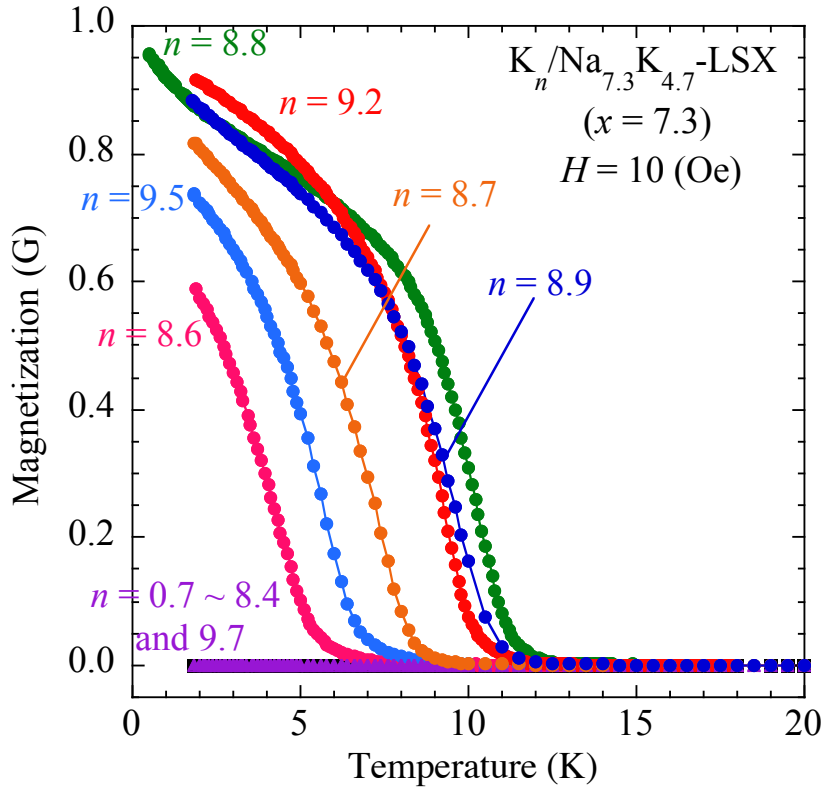

Fig. 3.5. Temperature dependence of magnetization in $K_n/Na_{7.3}K_{4.7}$-LSX (x = 7.3) measured under applied magnetic field of 10 Oe at $8.6 \leq n \leq 9.5$.

For higher loading density samples $8.7 \leq n \leq 9.5$, the behavior of the temperature dependence of magnetization, however, is quite different when compare with those at lower loading density. Figure 3.5 displays the temperature dependence of magnetization curves of $K_n/Na_{7.3}K_{4.7}$-LSX (x = 7.3) at $8.6 \leq n \leq 9.5$. The paramagnetic samples have very small magnetization in the scale of Fig. 3.5. At the samples with n = 8.6, the behavior of the temperature dependence of magnetization abruptly changes. With decreasing temperature, the magnetization steeply increases below ≈ 5 K and reaches a ferromagnetic value of 0.6 G at lowest temperature of 1.8 K. This results clearly show that the samples with n = 8.6 has the ferromagnetic property. For higher loading density samples, $8.7 \leq n \leq 9.5$, we observed similar behaviors of the temperature dependence of magnetization. For samples with n = 8.7 and 8.8, the magnetization starts to increasing below ≈ 9 K and ≈ 12 K, respectively. These samples also show larger ferromagnetic values at temperature of 1.8 K when

compare with that of samples with n = 8.6. Increasing loading density, the samples at 8.7 ≤ n ≤ 9.5, the ferromagnetic temperatures go down to below ≈ 11 K, ≈ 10.5 K and ≈ 7 K for samples with n = 8.9, 9.2 and 9.5, respectively. An additional measurement by using ^{3}He refrigerator are carried out to measure the temperature dependence of magnetization for the sample with n = 8.8 down to the temperature of 0.5 K. The result indicates that below ≈ 1.8 K the magnetization of the sample with n = 8.8 increases continuously with decreasing temperature down to 0.5 K. The value of magnetization at 0.5 K is observed of ≈ 0.9 G for this sample. The temperature dependence of magnetization for the sample with n = 9.7, the highest loading density sample, does not show ferromagnetic but paramagnetic behavior. This result implies that the ferromagnetic properties suddenly suppress between sample with n = 9.5 and 9.7. As we can see in the behavior of the temperature dependence of magnetization for $K_n/Na_{7.3}K_{4.7}$-LSX (x = 7.3) at 8.6 ≤ n ≤ 9.5, there is no zero-minimum magnetization as observed in the ferrimagnetic samples of $K_n/Na_{4.0}K_{8.0}$-LSX (x = 4.0). These above experimental results clearly show that the samples of $K_n/Na_{7.3}K_{4.7}$-LSX (x = 7.3) at 8.6 ≤ n ≤ 9.5 behave the ferromagnetic properties.

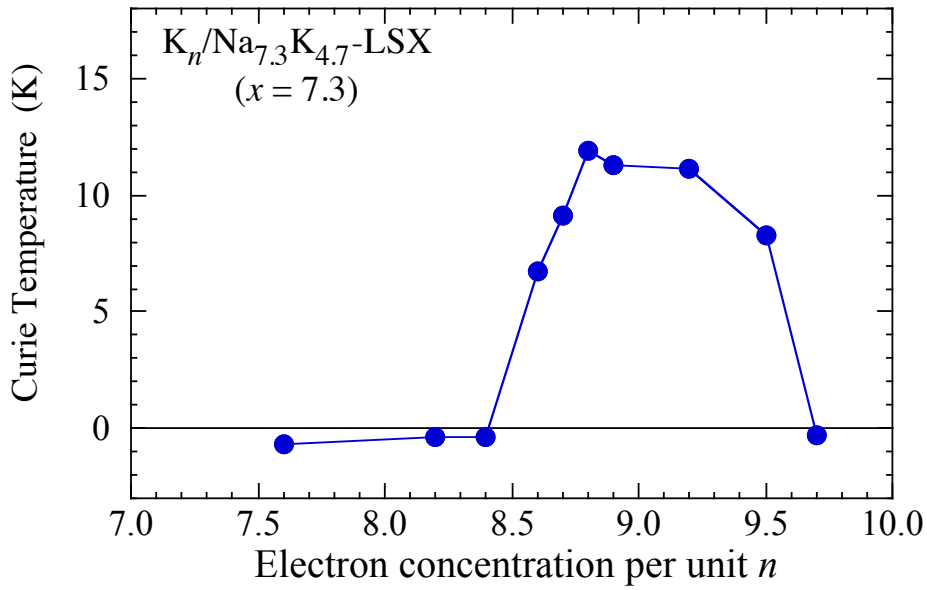

Fig. 3.6. K-loading density (Electron concentration per unit) n dependence of the asymptotic Curie temperature for $K_n/Na_{7.3}K_{4.7}$-LSX (x = 7.3).

Figure 3.6 displays the K-loading density n dependence of the asymptotic Curie temperature, which is estimated from the temperature dependence of magnetization in measured for $K_n/Na_{7.3}K_{4.7}$-LSX (x = 7.3) samples. With increasing the loading density, a finite values of Curie temperature are suddenly observed at sample with n = 8.4. For higher loading density samples, 8.6 ≤ n ≤ 9.5, the Curie temperature increases and decreases. As we see in this figure, a broad peak of the Curie temperature of ≈ 12 K at loading density n ≈ 9. A quickly decreasing of the Curie temperature is seen at higher loading density, between the samples with n = 9.5 and 9.7, where is the boundary of ferromagnetic properties.

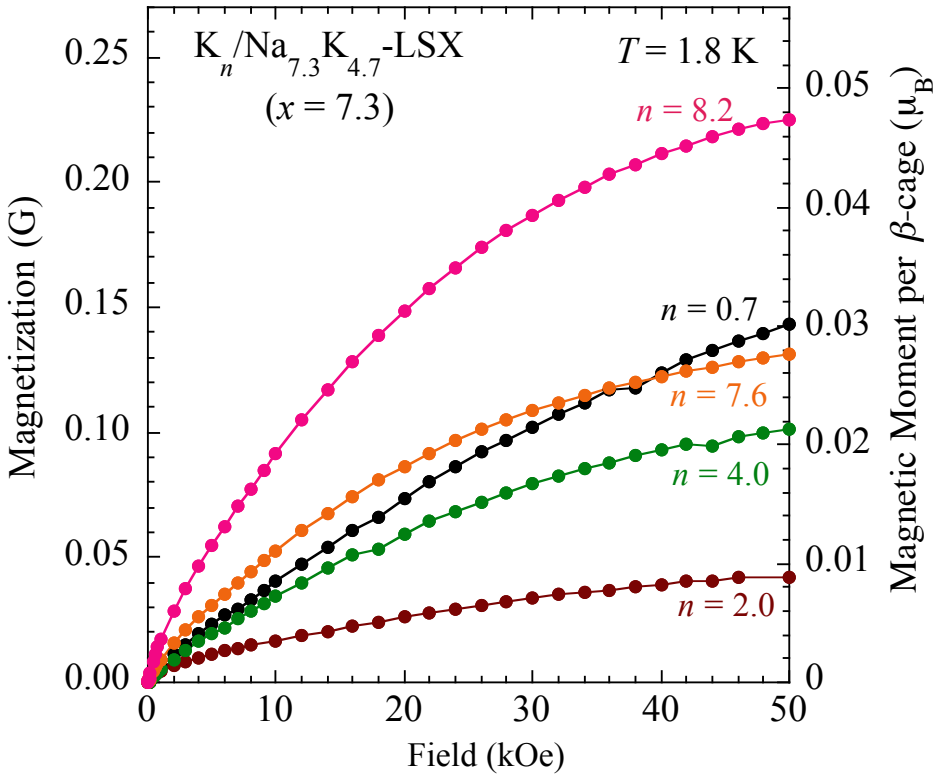

Fig. 3.7. Magnetization curves measured at 1.8 K with applied magnetic field up to 50 kOe for $K_n/Na_{7.3}K_{4.7}$-LSX (x = 7.3) at 0.7 ≤ n ≤ 8.2.

The measurements for magnetic field dependence of magnetization, with the applied magnetic field up to 50 kOe at the temperature of 1.8 K, were investigated for $K_n/Na_{7.3}K_{4.7}$-LSX (x = 7.3) at various loading densities samples. In plotted figures, we have already extracted the temperature independent magnetization term, for example

the diamagnetism, which is caused by quartz glass tube. Figure 3.7 shows the temperature dependence of magnetization for $K_n/Na_{7.3}K_{4.7}$-LSX (x = 7.3) samples at $0.7 \leq n \leq 8.2$. These samples have the paramagnetic properties. The magnetization curves exhibit paramagnetic behaviors, such as Brillouin function, as can be see in Fig. 3.7.

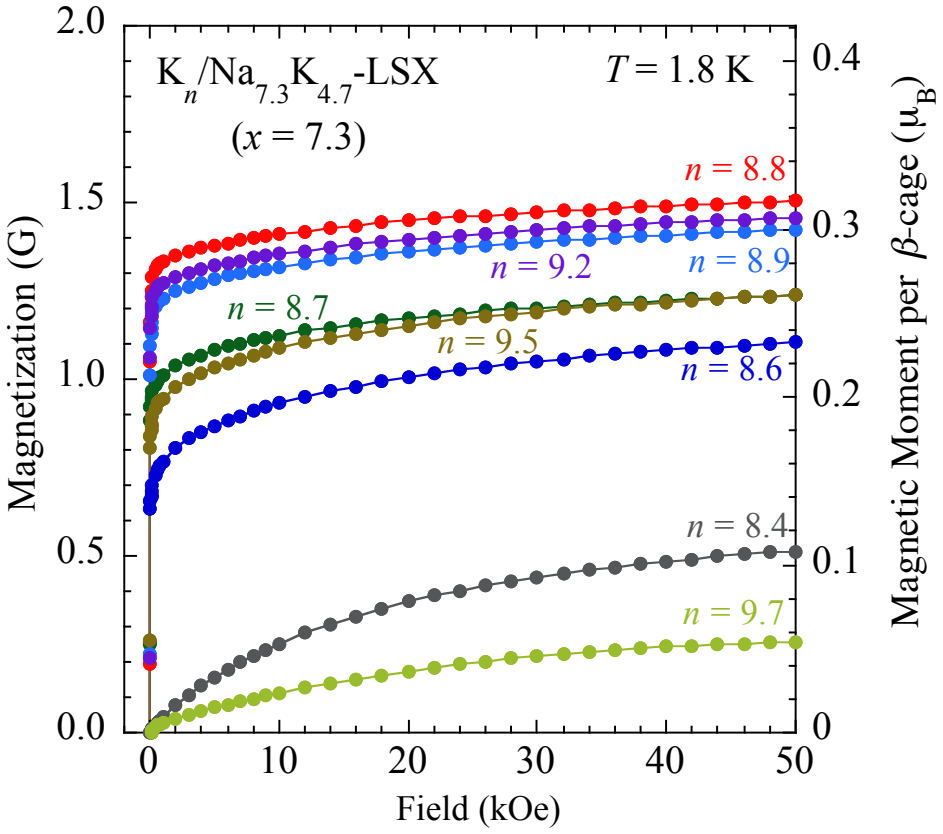

Fig. 3.8. Magnetization curves measured at 1.8 K with applied magnetic field up to 50 kOe for $K_n/Na_{7.3}K_{4.7}$-LSX (x = 7.3) at $8.4 \leq n \leq 9.7$.

The magnetization curves at 1.8 K for higher loading density samples at $8.4 \leq n \leq 9.7$, where including ferromagnetic samples, are plotted in Fig. 3.8. Paramagnetic behavior is also observed at the sample with n = 8.4. With increasing loading density, however, the magnetization curve suddenly changes its behavior for the sample with n = 8.6. For this sample, at lower applied magnetic field region the magnetization curve shows a quick increasing. At higher applied magnetic field the magnetization curve is seems to be saturated. This behavior of the temperature dependence of magnetization is typically property for ferromagnetic sample. The others samples, whose have

ferromagnetic properties $8.7 \leq n \leq 9.5$, have similar behaviors of magnetization curves when compare with that of sample with $n = 8.6$. The differences of the value of magnetic saturation at the highest applied magnetic field of 50 kOe are also seen. While for the highest loading density sample with $n = 9.7$, the paramagnetic magnetization curve is obtained consistently with paramagnetic properties of this sample.

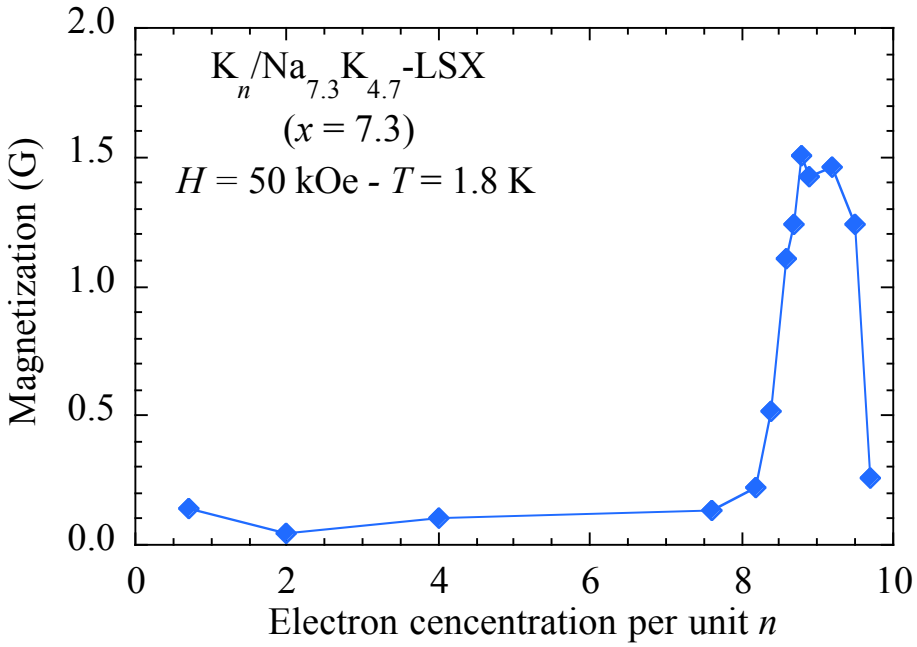

Fig. 3.9. Magnetization at 50 kOe as a function of K loading density for samples $K_n/Na_{7.3}K_{4.7}$-LSX (x = 7.3).

The magnetization at 50 kOe, which is extracted from the magnetization curves measured at 1.8 K, of samples $K_n/Na_{7.3}K_{4.7}$-LSX (x = 7.3) is plotted in Fig. 3.9 as a function of K loading density n. As shown in this figure, the magnetization is quite small at low loading density region $n < 8$. For higher loading density samples, the magnetization abruptly increases and shows a sharp peak at $n \approx 9$. Afterward, the magnetization quickly decreases. The highest value of magnetization at 50 Oe is ≈ 1.5 G, observed for the sample with $n = 8.8$. The increase and decrease of magnetization

at 50 kOe coincide with the occurrence of ferromagnetic properties in samples $K_n/Na_{7.3}K_{4.7}$-LSX (x = 7.3).

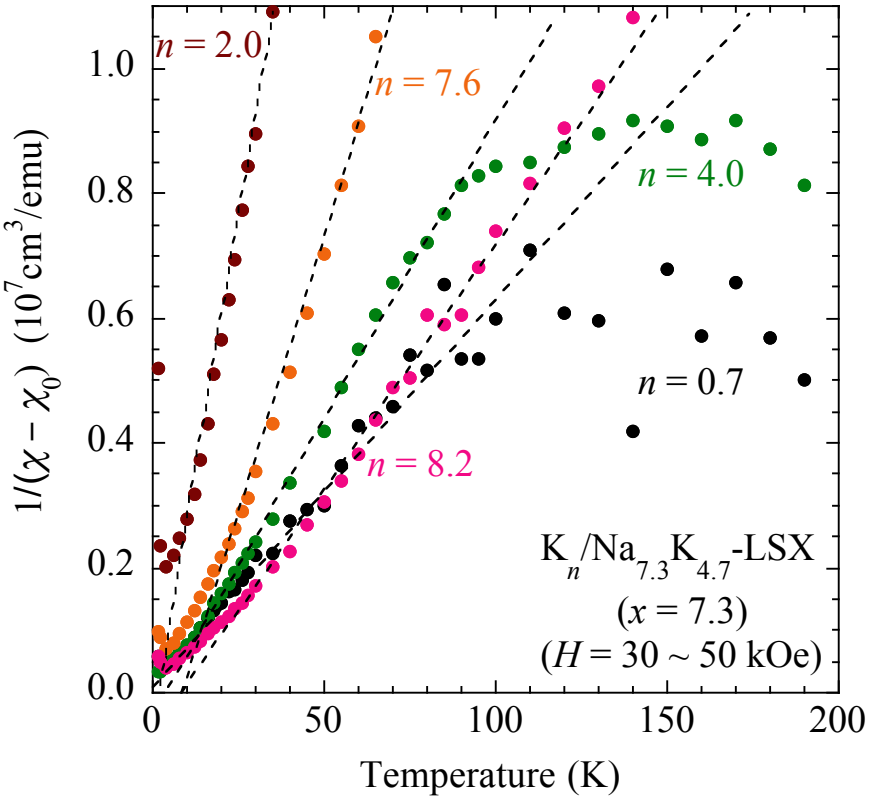

Fig. 3.10. Temperature dependence of the reciprocal of magnetic susceptibility for $K_n/Na_{7.3}K_{4.7}$-LSX (x = 7.3) at $0.7 \leq n \leq 8.2$.

Figure 3.10 shows the temperature dependence of the reciprocal of magnetic susceptibility, which determined by the difference of magnetization between applied magnetic field of 30 and 50 kOe, in $K_n/Na_{7.3}K_{4.7}$-LSX (x = 7.3) at lower loading density samples $0.7 \leq n \leq 8.2$. For samples with n = 0.7, 4.0 and 8.2, the reciprocal of magnetic susceptibility does not obey the Curie – Weiss law well at higher temperature region, especially for samples with n = 0.7 and 4.0 at temperature larger than ~ 80 K. The broken lines are plotted in the figure in order to guide eyes for Curie – Weiss fitting. A similar plots of the temperature dependence of the reciprocal of magnetic susceptibility in $K_n/Na_{7.3}K_{4.7}$-LSX (x = 7.3) at higher loading density

samples 8.4 ≤ n ≤ 9.7 are displayed in Fig. 3.11. Differently with samples at lower loading density, the samples at 8.4 ≤ n ≤ 9.7 exhibit a well fitting with the Curie – Weiss law at higher temperature region. In addition a remarkable loading density dependence of the Curie constant is obtained from this figure. At lower temperature region in both Fig. 3.10 and Fig. 3.11, we can see the saturation effect of the magnetization, which is caused by high magnetic field, in the values of the reciprocal of magnetic susceptibility.

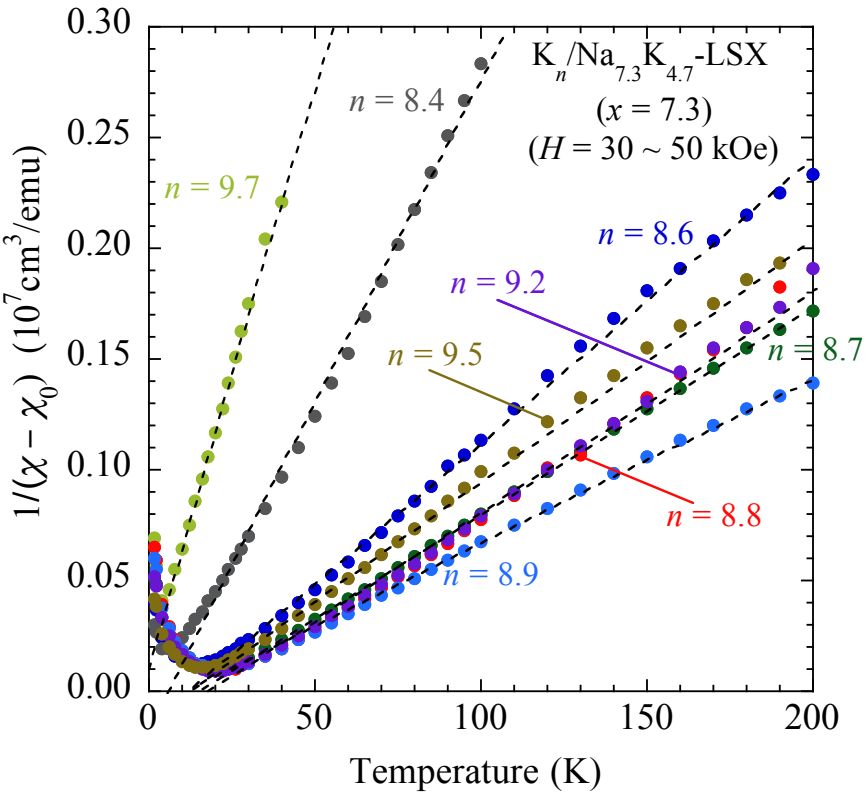

Fig. 3.11. Temperature dependence of the reciprocal of magnetic susceptibility for $K_n/Na_{7.3}K_{4.7}$-LSX (x = 7.3) at 8.4 ≤ n ≤ 9.7.

From the experimental data of the temperature dependence of reciprocal of magnetic susceptibility, we perform the estimation of the Curie constant and Weiss temperature for samples $K_n/Na_{7.3}K_{4.7}$-LSX (x = 7.3).

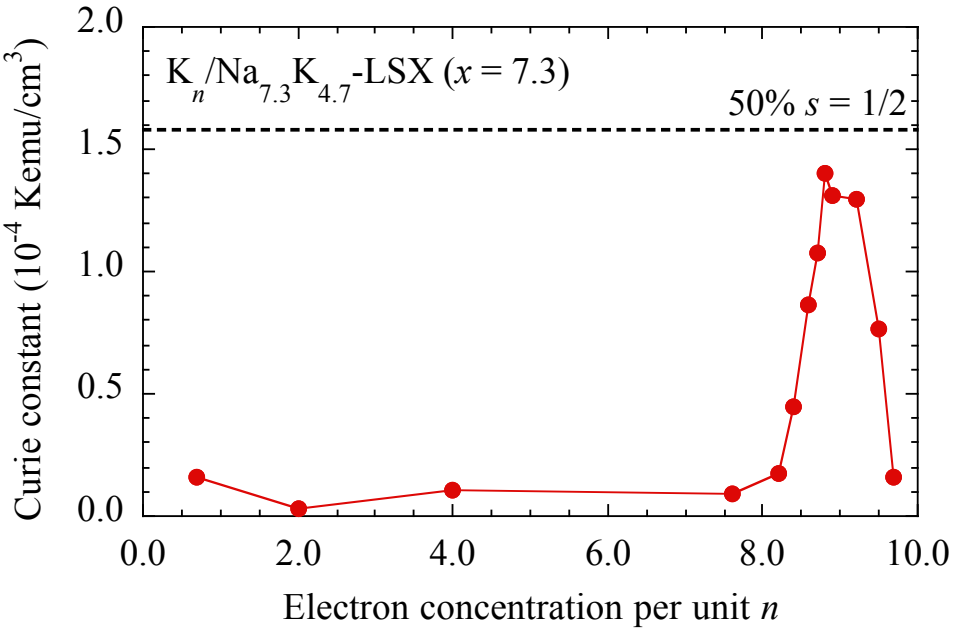

Fig. 3.12. K-loading density n dependence of the Curie constant for samples $K_n/Na_{7.3}K_{4.7}$-LSX (x = 7.3).

Figure 3.12 shows the K loading density dependence of the Curie constant for samples $K_n/Na_{7.3}K_{4.7}$-LSX (x = 7.3). At lower loading density samples n < 8, the values of Curie constant are very small, indicating there is no sign for the existence of magnetic moment in these samples. At n > 8, values of Curie constant start to increase and show a broad peak with maximum value of 1.4 (10^{-4} Kemu/cm^3) at n = 8.8. This value is close to the value of 1.6 (10^{-4} Kemu/cm^3), which is the value of Curie constant estimated for the case of 50 % of β-cages occupied by spin ½. The dotted line is plotted together in Fig. 3.12 in order to exhibit this value. At higher loading density samples, the Curie constant decreases down to nearly zero at the sample with n = 9.7. Above results obviously show that there is formation of magnetic moment in $K_n/Na_{7.3}K_{4.7}$-LSX (x = 7.3) at higher loading density samples. These results are also relates with the observed of ferromagnetic properties at higher loading density samples. From the magnetization curves, the saturated magnetization of ferromagnetic samples in $K_n/Na_{7.3}K_{4.7}$-LSX (x = 7.3) is estimated of ≈ 1.5 G. The value of magnetization, which is estimated from the Curie constant, is of around ≈ 70 % of saturated magnetization. That means most of magnetic moments estimated from the

Curie constant are participate in the ferromagnetic magnetization. On the other hand, the increase and decrease behavior of the Curie constant may have close relation with the appearance of optical reflection bands in reflectance spectra of $K_n/Na_{7.3}K_{4.7}$-LSX (x = 7.3). This will be discussed later in this chapter in details.

The loading density dependence of Weiss temperature for $K_n/Na_{7.3}K_{4.7}$-LSX (x = 7.3) is displayed in Fig. 3.13. With increasing loading density, values of Weiss temperature gradually increase. In the region where we observe ferromagnetic properties, Weiss temperature has positive values and the behavior of loading density dependence of Weiss temperature is quite similar with that of Curie temperature. However the values of Weiss temperature is little bit larger than the values of Curie temperature. It may be caused by the inhomogeneous distribution of the stronger ferromagnetic interaction between magnetic moments.

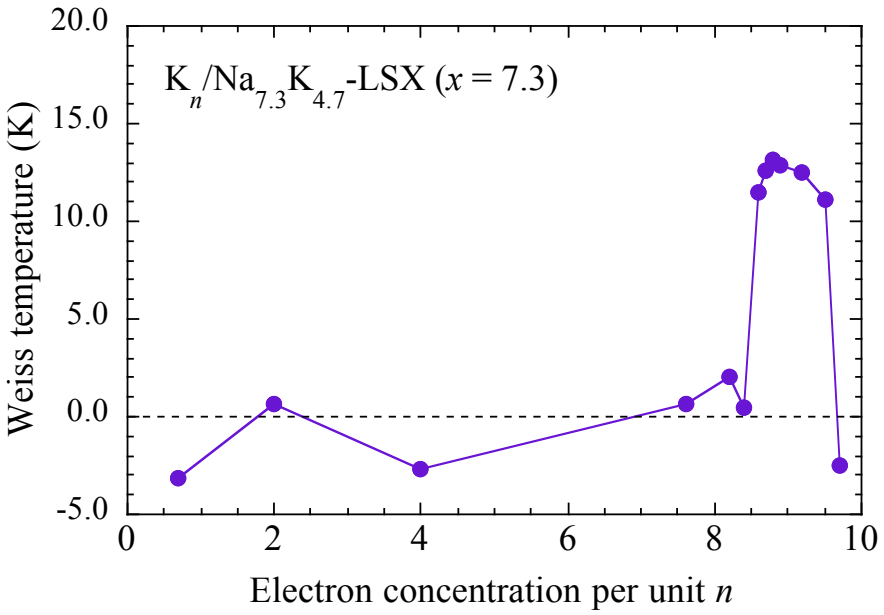

Fig. 3.13. K-loading density n dependence of Weiss temperature for samples $K_n/Na_{7.3}K_{4.7}$-LSX (x = 7.3).

The estimated Curie constant, Weiss temperature and asymptotic Curie temperature of samples $K_n/Na_{7.3}K_{4.7}$-LSX (x = 7.3) are plotted together at higher loading density region in Fig. 3.14. As seen in this figure, in ferromagnetic phase, where the

ferromagnetic properties occur, the Weiss temperature has positive values and similar with those of extrapolated Curie temperature. This observed behavior in loading density dependence of Weiss temperature and extrapolated Curie temperature typically appear in the ferromagnetic material.

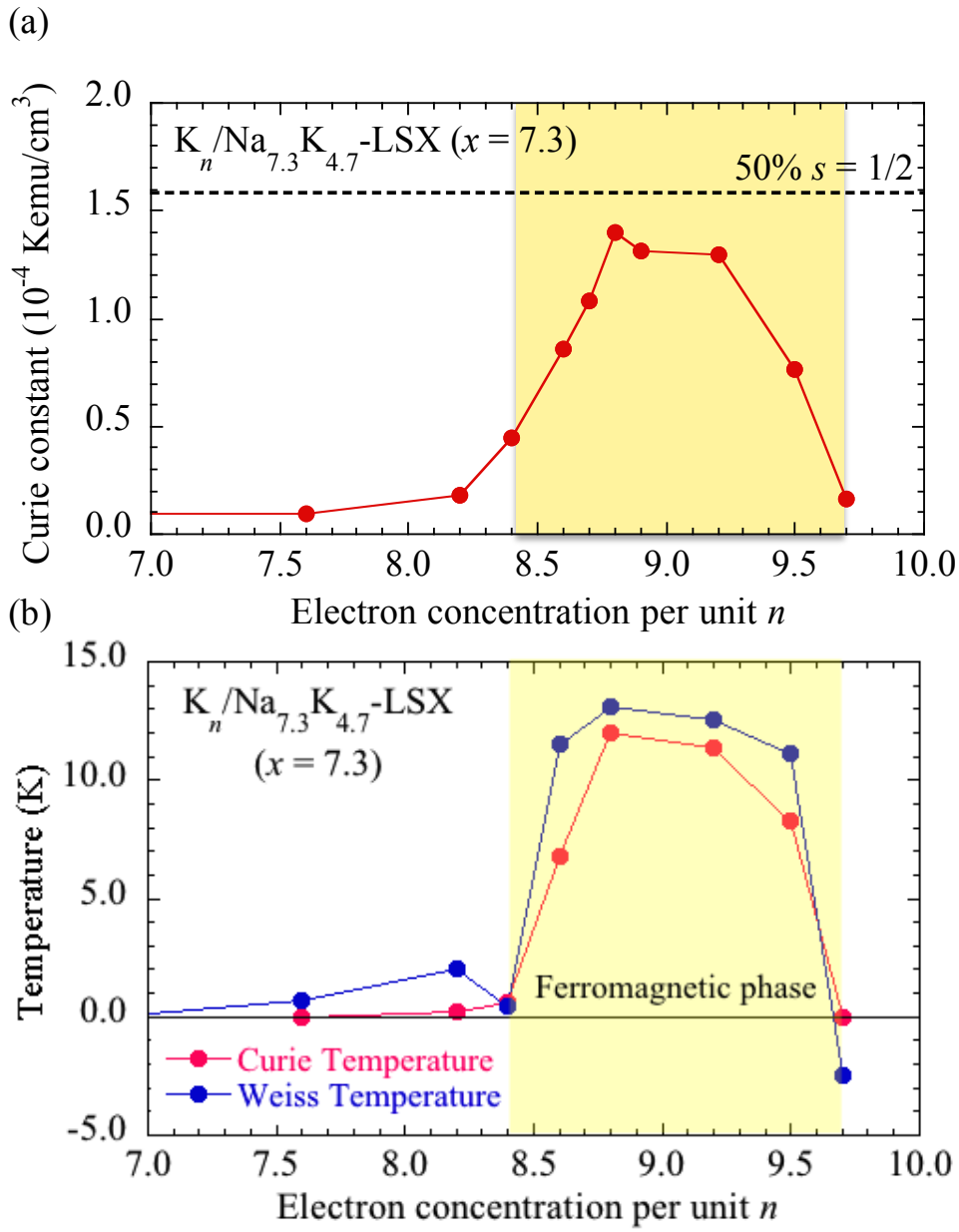

Fig. 3.14. Curie constant (a), Weiss temperature and Curie temperature (b) as a function of K loading density n for $K_n/Na_{7.3}K_{4.7}$-LSX (x = 7.3) at higher n region.

3.1.3 Electric transport properties

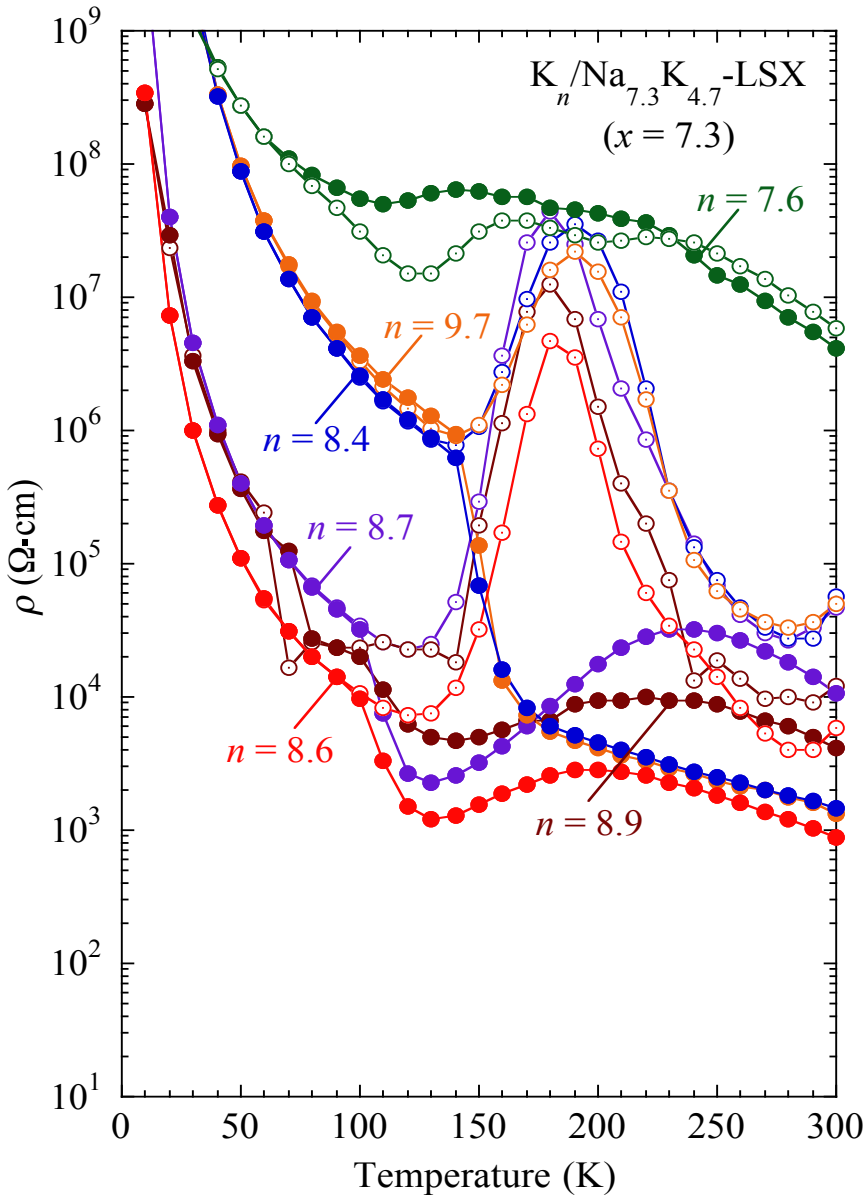

Fig. 3.15. Temperature dependence of electrical resistivity ρ for $K_n/Na_{7.3}K_{4.7}$-LSX (x = 7.3) at various loading densities measured in cooling and warming processes. The solid circles and open circles with dots correspond to the cooling and warming process, respectively.

The temperature dependence of electrical resistivity ρ for $K_n/Na_{7.3}K_{4.7}$-LSX (x = 7.3) at various loading densities, including both paramagnetic and ferromagnetic samples, is displayed in Fig. 3.15. The electrical resistivity was measured from 300 K down to

10 K with the cooling and warming processes, which is indicated by solid and open circles, respectively. For the sample with n = 7.6, a paramagnetic sample, the value of resistivity at room temperature is very high, in the order of 10^7 Ω·cm. With decreasing temperature the resistivity gradually increase with some anomalies at around ≈ 240 K and ≈ 120 K and exceeds the value of 10^9 Ω·cm below 40 K. In warming process, the temperature dependence of electrical resistivity shows a deviation with that of cooling process. It is attributed to the thermal hysteresis. At higher loading density paramagnetic sample n = 8.4, we observed the decreasing of the value of resistivity at room temperature to 10^3 Ω·cm when compare with the case of sample n = 7.6. In the cooling process, the resistivity gradually increases down to around ≈ 150 K. Below this temperature, the resistivity quickly increases and shows a kink at 140 K. At lower temperature, the resistivity exceeds the value of 10^9 Ω·cm below 40 K. There is no deviation between the resistivity in the cooling and warming processes at lower temperature region ≤ 140 K. However the resistivity exhibits a large deviation at the temperature > 140 K, and shows a peak at ≈ 190 K. It is interesting that the behavior of the temperature dependence of electrical resistivity in cooling and warming processes in paramagnetic samples with n = 8.4 and 9.7 look like quite similar. These samples lie just below and above the ferromagnetic phase at $8.6 \leq n \leq 9.5$. In addition the temperature dependence of electrical resistivity for ferromagnetic samples with n = 8.6, 8.7 and 8.9 also show similar behavior. These samples have the value of resistivity in the order of 10^3 Ω·cm – 10^4 Ω·cm at 300 K. In the cooling process, the resistivity gradually increases and shows a broad peak at ≈ 200 K. A kink at around ≈ 100 K is observed at lower temperature region. The value of resistivity increase up to the order of 10^8 Ω·cm at 10 K for samples with n = 8.6 and 8.9, while the value of resistivity of the sample with n = 8.7 exceeds 10^9 Ω·cm below 20 K. With increasing temperature the resistivity shows a minimum at around ≈ 120 K and a peak at around ≈ 180 K. These results obviously show that all of samples, including paramagnetic and ferromagnetic samples, are basically in insulating state. The origin of kinks observed at ≈ 140 K and ≈ 100 K in cooling processes, peaks observed at ≈ 180 K and ≈ 190 K observed in warming processes and the thermal hysteresis is not well known at the present stage. However we did not observe any anomalies at these temperatures in the magnetic susceptibility as shown in Fig. 3.10 and Fig. 3.11. Therefore the

anomalies observed in the temperature dependence of electrical resistivity are thought to have no relation with the magnetic properties of samples.

Recently, a ^{23}Na NMR investigation has been carried out in the melting and freezing phase transition of the Na-K alloy of the eutectic composition confined in a geometry silica porous glass, which forms an intermetallic compound of Na_2K. The temperature dependence of Knight shift in the cooling and warming process are irreversible. With decreasing temperature, the Knight shift slowly decreases and shows a step like at ≈ 210 K. Differently from the cooling process, the Knight shift smoothly increase in the warming process. These results imply a larger thermal hysteresis of Na_2K eutectic alloy. The smoothly changes, which is observed in the Knight shift, can be assigned to the continuous structural transformation in the Na_2K eutectic alloy [81]. A similar mechanism can be considered as the origin of anomalies in the resistivity. Some structural changes, which caused by cation distribution, may lead to the formation of kinks, peaks and thermal hysteresis as observed in the temperature dependence of electrical resistivity for $K_n/Na_{7.3}K_{4.7}$-LSX (x = 7.3) samples.

3.2 Discussion on $K_n/Na_{7.3}K_{4.7}$-LSX (x = 7.3)

3.2.1 Discussion on electronic states and magnetic moments of clusters

As we mentioned earlier, the optical reflection bands at 2.4 eV and 2.8 eV, which observed in the optical reflectance spectra, can be attributed to the resonant excitation of s-electrons confined in the β-cage clusters. On the other hand, we observed an optical absorption band at 2.6 eV in the optical absorption spectrum of dilute sample for $K_n/Na_{7.3}K_{4.7}$-LSX (x = 7.3). This band is also assigned to the excitation of s electron in the clusters, which formed in β-cages. In this case, the ground state and optical excited state are both well localized within clusters in β-cages. It is noted that the energies of optical excitation are slightly different for these bands. The differences may be come from the differences of the cation distribution or configuration and the kind of alkali cations in zeolite framework located at β-cage. The appearance of the optical reflection bands at 2.4 eV for the sample with n = 4.0 and 7.6, as can be seen in optical reflectance spectra, are assigned to the formation of spin-singlet state (nonmagnetic) clusters in β-cages because the values of Curie constant are very small for these samples. However the reflection bands at 2.8 eV, observed for the samples with $n > 7.6$, may imply the formation of clusters in β-cage with different spin states. The optical reflection bands at 2.8 eV appears firstly in the sample with n = 8.2. It grows, keeps the spectra intensity up to the sample with n = 9.5 and then becomes broader at $n > 9.5$.

As seen in Fig. 3.14 (a), the loading density dependence of Curie constant also exhibits similar behavior with observed in optical reflectance spectra at loading density $n > 7.6$. The value of Curie constant gradually increases from the sample with n = 8.2 to n = 8.8, keeps its values up to the sample with n = 9.2 and then quickly decreases at $n > 9.2$. According to the relation between the appearance of optical reflection bands at 2.8 eV and the increasing of the value of Curie constant at $n > 7.6$, the optical reflection bands at 2.8 eV can be assigned to the formation of spin-doublet state (magnetic) clusters in β-cages. However a slight discrepancy can be found in $8.2 \leq n \leq 8.8$, where the growth of the value of Curie constant appears little bit later than that of optical reflection bands at 2.8 eV. Moreover, at the loading density $n > 9.2$ the value of Curie constant decreases while the optical reflection bands at 2.8 eV still keeps its spectra intensity. The s-electron excitations appear in the optical spectra independently with the spin states of clusters. Therefore the optical excitation of s-

electron in β-cage clusters, as observed in the reflectance spectra, includes both of singlet-spin state and doublet-spin state. Hence the delayed growth of the value of Curie constant with appearance of optical reflection band at 2.8 eV can be explained by the coexistence of spin-singlet and spin-doublet clusters. The decreasing of value of Curie constant at $n > 9.2$ is may be caused by the decreasing of spin-doublet clusters. The spin-singlet clusters dominate in the system simultaneously when the second s electrons occupy the spin-doublet clusters. At higher loading density $n = 9.7$, most of clusters are occupied by spin-singlet states, leading to small values of Curie constant while the optical reflection spectra still keep its intensity.

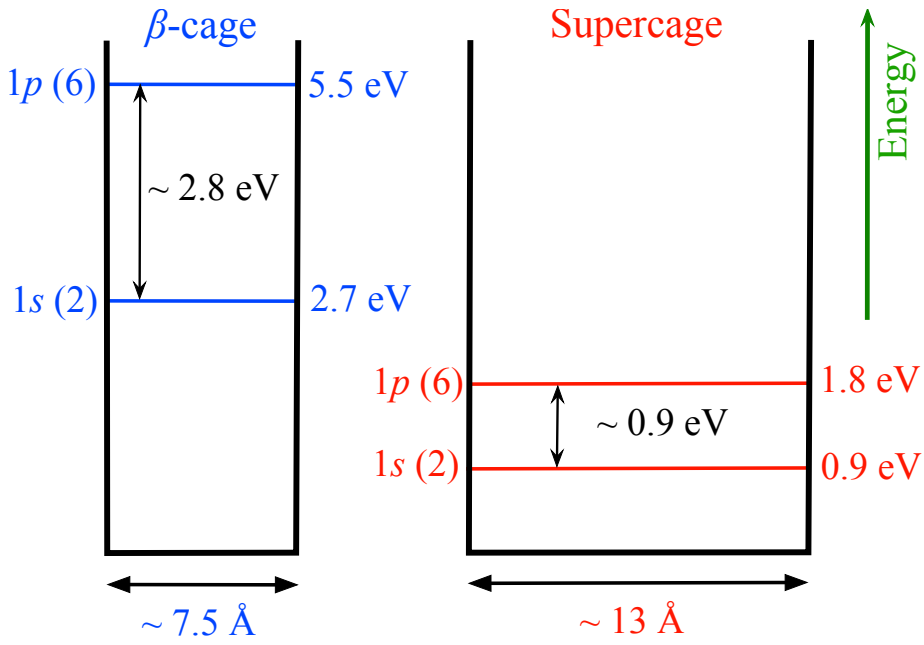

Fig. 3.16. Schematic illustration of model of spherical well potential with the quantum states 1s and 1p with corresponding kinetic energy for β-cage and supercage.

If we consider a model of a spherical well potential with the diameter of 13 Å for supercage and 7.5 Å for β-cage, the kinetic energies of a free electron at the 1s-state and 1p-state for supercage will be estimated as 0.9 eV and 1.8 eV, respectively. And corresponding kinetic energies for β-cage will be 2.7 eV and 5.5 eV. The schematic illustration of spherical well potential models for β-cage and supercage are plotted in Fig. 3.16. The s electrons will occupy 1s-state and 1p-state of the supercages preferentially at lower loading density due to the lower kinetic energies of large

diameter of supercage when we ignore the interaction of cations in zeolite framework and s electrons. According to this model, the 1s-state and 1p-state of supercages will be fully occupied by two s-electrons and six s-electrons, respectively. These s electrons are provided by the K atoms, which loaded into zeolite LSX. There are now totally eight s-electrons, corresponding to K-loading density n = 8, in supercages. With increasing loading density, the ninth and tenth s electrons can occupy β-cages because of the increasing in the Fermi energy. The real system, however, there are existences of correlation between s-electrons within clusters and the interaction between the cations in zeolite framework and s electrons. Hence we proposed a simple model for the distribution of s-electrons in the loading density region $8 \leq n \leq 10$. Figure 3.17 plots the illustration for this simple model. The average number of s-electrons occupy β-cages can be changed depending on the loading density n. At the loading density n = 8, both of 1s-state and 1p-state of supercages or the sp^3 hybridized states of the T_d symmetry of supercages are fully occupied by eight s electrons. Meanwhile there is no s electron in β-cages, as we can see at the left hand side figure in Fig. 3.17. At higher loading density, n = 9, the ninth s electron starts to occupy the 1s state of β-cages, leading to the formation of spin-doublet clusters in β-cages. The value of Curie constant increase and ferromagnetic properties are obtained. In optical reflectance spectra, we observed the appearance of reflection band at 2.8 eV. The spin-singlet clusters with a pair of s-electrons may not be formed at the loading density $n \leq 9$ because of strong Coulomb repulsion between s electrons. At $n > 9$, another s-electrons can come into β-cages and occupy the 1s-state, forming spin-singlet clusters in β-cages. The value of Curie constant starts to decrease due to the decreasing of spin-doublet clusters. At n = 10, all of β-cage clusters are in spin-singlet state.

According to this model, the mechanism of increasing and decreasing in the loading density n dependence of Curie constant as well as the appearance of optical reflection bands at 2.8 eV can be explained in principle schematically. A similar model has been proposed to explain the ferrimagnetic properties in the K-rich samples $x \leq 4$ [65, 21]. However the balance of potential between supercage and β-cage is quite different in the case of K-rich samples $x \leq 4$ and Na-rich sample x = 7.3. This may relate to the number of Na^+ cation in FAU framework as well as the places, where these cations are distributed. In addition, the electrical transport properties are also important in the

electronic model of sample. The K-rich samples $x \leq 4$ has been confirmed to be metallic states at higher loading density. In the meanwhile, Na-rich sample $x = 7.3$ is in insulating state even at higher loading density region.

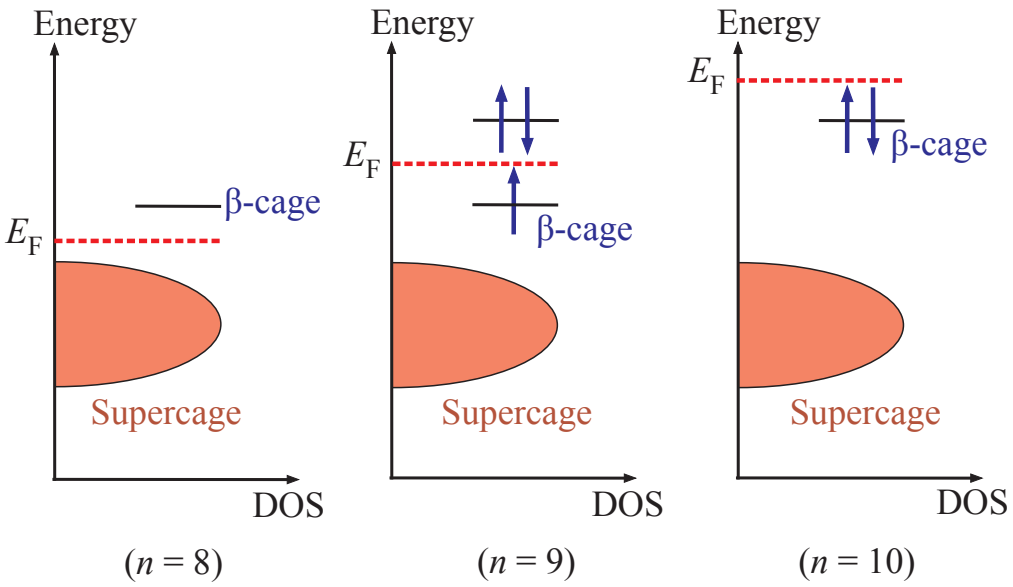

Fig. 3.17. Schematic illustration for a simple model of electronic configuration in $K_n/Na_{7.3}K_{4.7}$-LSX ($x = 7.3$) at $8 \leq n \leq 10$.

3.2.2 Discussion on electronic states and cation distribution

In our present studies, it is important to understand the electronic state of s-electron and the correlation between s-electrons. In order to do that, it is essential to consider about the position of cations, the number of cations and the kind of alkali cations in zeolite cages. In a non-loaded zeolite, cations located at site III', as seen in the crystal structure of zeolite LSX in chapter I, and other sites in supercages are attached to the negatively charged zeolite framework. These cations keep the force balance between the Coulomb attraction force, which is caused by the negative charge of zeolite framework, and the repulsion force by the Pauli exclusion principle, which is caused by cations themselves. The cations at site II, the single 6-membered ring between supercage and β-cage, are freestanding. The postion of cations located at site II are adjusted along the single 6-membered ring window in order to minimize the electrostatic field form the other cations and zeolite framework. Another cations lie at

the site I and site I', which are located at the center of the double six-membered ring and both sides of double six-membered ring, respectively. If the s electrons are loaded into zeolite LSX, these s-electrons will have the short-range interaction with surrounding cations, the long range electrostatic interaction with distant cations as well as the repulsive interaction with negative charge zeolite framework. The position of cations is then locally adjusted by the additional interaction with s-electrons to have lower energy, and this kind of interaction is called electron-phonon interaction. For the s-electrons, the final states are formed into the polarons with the cation displacements. In the case of large polaron, the size of polaron is much larger than the size of zeolite case, then the cation displacement is small, leading to free moving as a free carrier of the polaron. However in the case the cation displacement creates a electronic potential deep enough to localized the s electron quantum mechanically, the s-electron will be self-trapped as a small polaron [61]. In this case the small polaron cannot move freely due to a heavy mass. On another case, if the electronic potential is deep enough to trap the second electron despite the Coulomb repulsion between two s-electrons, the small bipolaron state will be generated.

In the case of Na_n/Na_{12}-LSX, reflection bands at 2.5 eV are observed in the reflectance spectrum at loading density $n < 2$. This band is attributed to the nonmagnetic and insulating Na-clusters in β-cage [59]. At $2 < n < 5$, reflection bands at 2.5 eV disappears and new reflection bands appear. The new reflection band is assigned to the supercage clusters. At loading density $n > 5$, another β-cage reflection bands appear at energy of 2.8 eV. The structural investigation has been carried out for Na_n/Na_{12}-LSX at the loading density $n = 9.4$ and $n = 16.7$. The results show that the site I and I' are fully occupied by Na cations despite the Coulomb repulsion between three Na cations at the double 6-membered ring [82]. This kind of cation-rich β-cage are generated at higher loading density and may have a deeper electronic potential with slight narrowing of potential size due to large cohesion energy of Na atoms. The increasing from 2.5 eV to 2.8 eV in the energy of reflection bands can be explained by the slight narrowing of the potential size. Most of these Na clusters are in nonmagnetic and insulating state at $n \leq 10$. At higher loading density $n > 11$, a thermally excited paramagnetic susceptibility has been observed in metallic phase [60, 83]. In the K-rich system ($x \leq 4$), the optical absorption spectra of dilute samples of K_δ/K_{12}-LSX ($x = 0$) and $K_\delta/Na_{4.0}K_{8.0}$-LSX ($x = 4.0$) exhibit the fact that, there is no

sign of absorption bands in β-cage. These results may imply that the number of cations distributed in β-cage could not make a deep enough well potential in order to trap electron here. In this case K-rich situation can be attributed to β-cage.

Returning to the present system $K_n/Na_{7.3}K_{4.7}$-LSX (x = 7.3), at lower loading density sample we also observed the significant bands at 2.5 eV of β-cage. Na cations are preferentially located at site I and I' in β-cage. Additional location of Na cations is site II. If the Na cations occupy these sites, they will generate a Na-rich cluster with deep electronic potential at β-cage and attract the s-electrons. The s-electrons also attract Na cations more than K cations due to higher ionization energy of Na atoms. The potential of the K-rich (Na-poor) β-cage clusters is not deep enough to attract the s-electrons. Then s electrons will move to supercage. In Na-rich (x = 7.3) system, some β-cages have eight or more Na cations. These Na-rich clusters may have deep enough potential to attract the second s-electron to stabilize spin-singlet clusters such as small bipolaron. Moreover, the distribution of Na cations in $K_n/Na_{7.3}K_{4.7}$-LSX (x = 7.3) may be not homogeneous due to stronger cohesion energy of Na atoms than that of K atoms [84]. In order to understand the formation of nonmagnetic cluster at lower loading density in $K_n/Na_{7.3}K_{4.7}$-LSX (x = 7.3), it is necessary to assume there are two types of β-cage clusters. In the first type, can be call as Na-rich β-cage cluster, the β-cage have enough Na cations together with s-electron to stabilize nonmagnetic clusters. In the second type, can be call as K-rich (Na-poor) β-cage cluster, the number of Na cations in β-cage is not enough to attract the s-electron at lower loading density. In the higher loading density sample n = 8.2, small amount of spin-singlet clusters are generated in Na-rich β-cage as well as most of supercages are occupied by spin-singlet Na-K alloy clusters. The supercage clusters have sp^3 closed-shell, which is fully occupied by eight s-electrons. In other word, for the case of n = 8.2 we have 8 electrons in supercage closed-shell cluster and 0.2 electrons in β-cage spin-singlet clusters. With increasing K-loading density the Fermi energy increase, K-rich (Na-poor) β-cage clusters are able to accept the s-electrons. A number of β-cage clusters have the potential shallower than the others, then spin-singlet clusters are not formed but spin-doublet clusters with unpaired s-electron. This kind of β-cage clusters may be half of total number of β-cage clusters. According to the loading density dependence of Curie constant, the maximum number of spin-doublet β-cage clusters is evaluated to be $\approx$ 45 % at the sample with n = 8.8. The remaining β-cage clusters ($\approx$ 55 %) have

deep enough potential to stabilize spin-singlet clusters. With increasing loading density, the number of spin-singlet β-cage cluster increases. And at highest loading density sample n = 9.7, most of β-cage clusters are in spin-singlet states with very small value of Curie constant while optical reflection band at 2.8 eV still exist.

3.2.3 Model of superexchange ferromagnetism

In the previous studies on lower Na-concentration samples ($x \leq 4$), a metallic transition is observed at higher loading density samples. These samples also exhibit the ferrimagnetic properties. The observed ferrimagnetism could be explained by the model of non-equivalent magnetic sublattices, one of which form the itinerant electron system in the supercage cluster network and the other has the localized magnetic moment in β-cage clusters, with antiferromagnetic coupling. Differently with ferrimagnetic properties, in the present higher Na-concentration sample (x = 7.3), we observed the ferromagnetic properties by localized magnetic moments in β-cage clusters. According to the structure of zeolite LSX, the direct exchange interaction between the adjacent β-cages is very rare because the β-cages are well separated by the double six-membered ring. However, β-cage clusters can have the interaction with the supercage cluster via single six-membered ring. In the case of sodalite, where β-cages are arranged in a body centered cubic structure with sharing window of single six-membered ring of β-cages, an antiferromagnetic ordering has been obtained below the Néel temperature of 48 K [16, 85]. A finite transfer energy of s electrons between Na^{3+}_4 clusters in adjacent β-cage clusters has also been investigated [86]. Hence, in order to clarify the origin of ferromagnetic ordering between the magnetic moment in adjacent β-cage clusters, we consider a model of indirect magnetic exchange interaction. There are several kinds of indirect magnetic exchange interaction. For example, in metallic materials, indirect magnetic exchange interaction such as the Zener's double exchange interaction or the Ruderman-Kittel-Kasuya-Yosida (RKKY) interaction can be considered as the candidate for the origin of magnetic ordering. Inn the present study, however, the samples at higher Na-concentration x = 7.3 exhibit the insulating properties together with ferromagnetism. The most plausible indirect magnetic exchange interaction would be the superexchange interaction, which normally appears in the insulating phase. Therefore, we propose a possibility of superexchange ferromagnetism because it applicable to the transport properties,

magnetic properties and also to the geometrical configuration between magnetic moments in the second nearest neighbor β-cages via the supercage clusters. In the ordinary model of superexchange interaction is proposed for the indirect magnetic interaction between magnetic ions through the ligand oxygen orbitals in the transition metal oxides. The sign of the exchange coupling can be determined by the bonding angle between the magnetic ions, as given by the Goodenough-Kanamori-Anderson rules [70, 75, 77, 78]. In the case of 180^0 bonding, where the d-electrons of magnetic ions hybridize with the same p-orbital of oxygen atoms, the kinetic exchange dominates and an antiferromagnetic interaction is realized. If the bonding angle is 90^0, the d-electrons of magnetic ions will hybridize with the orthogonalized p-orbital of oxygen atoms. Then there is no kinetic exchange interaction, and the potential exchange interaction will dominate the ferromagnetic interaction [75].

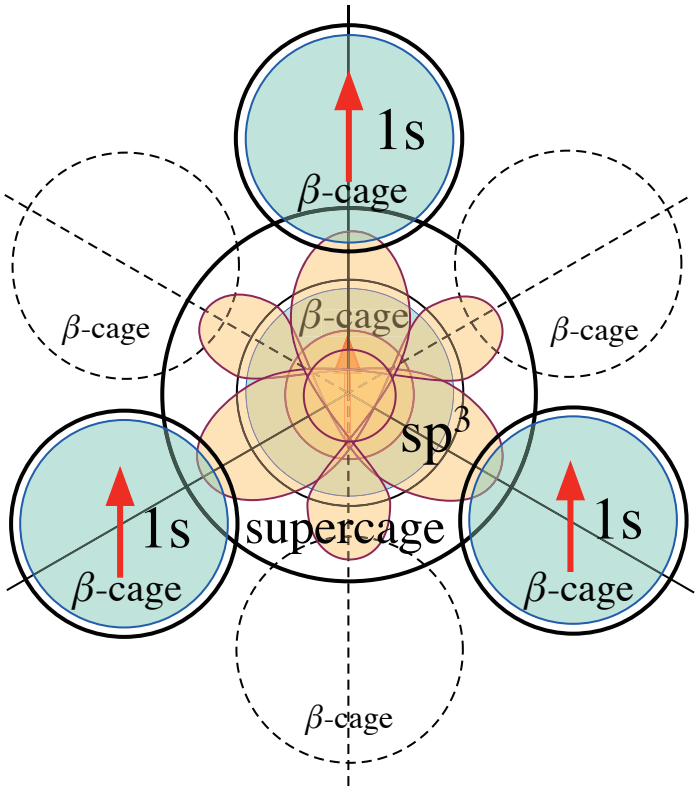

Fig. 3.18. Schematic illustration of the model of ferromagnetic superexchange interaction between localized magnetic moments in β-cage clusters through the sp^3-like states in supercage.

A similar model of superexchange ferromagnetism can be proposed for samples $K_n/Na_{7.3}K_{4.7}$-LSX (x = 7.3) at n > 8. Fig. 3.18 shows the schematic illustration of the model of superexchange ferromagnetism. In this model the sp^3-like hybridized orbital with eight electrons is realized in supercage, as a substitute for oxygen atoms in transition metal oxides. Four magnetic β-cage clusters surround the supercages cluster, as a substitute for magnetic ions. One supercage is connected to ten β-cages. Among these ten β-cages, four of them have sharing sing six-membered ring window with supercage and they are in tetrahedral arrangement with T_d symmetry. The other six β-cages are connected to the supercage through single four-membered ring. The four β-cage clusters have unpaired s electrons in 1s-like state. They are assumed to have the mutual interaction through the supercage. Namely the hybridization of 1s-like states in four surrounding β-cages and four orthogonalized sp^3-like states of supercage is proposed. In a similar way with ordinary model of superexchange interaction, the orthogonalized sp^3-like orbital will reduce the kinetic exchange interaction, leading to the domination of potential exchange interaction. As a result, the ferromagnetic interaction is realized.

The calculation for a similar electron correlation in the sp^3 hybridized state in CH_4 molecule has been investigated [87-89]. In terms of the other six β-cage clusters, they do not have the interaction with mentioned supercage, because the sharing window single four-membered ring is too narrow. They also connect two four β-cages mentioned above through the double six-membered ring but the interaction is not expected. β-cages, which belongs to the four β-cages clusters mentioned above can exhibit the mutual interaction with each others through the nearest neighbor supercage in a tetrahedral arrangement. Meanwhile supercages do not have interaction with adjacent ones. The arrangement of interaction between β-cages network and supercage network without the intra-network interaction generate a double bipartite lattice or double zincblende structure. If we assume the magnetic network is realized in only one of double bipartite network then the ferromagnetic properties can be generated via superexchange interaction between localized magnetic moments at half of β-cages. This model is able to explain consistently the ferromagnetic properties at lower temperature observed for $K_n/Na_{7.3}K_{4.7}$-LSX (x = 7.3) with the 45% occupation magnetic moments in β-cage clusters network. At this stage, unfortunately we do now have any direct evidence of the alternating ordering or β-cage clusters. Another

possibility that the magnetic moments are random distribution at half of β-cages, leading to the formation of two independent ferromagnetic networks, where both of these two networks have the magnetic moments above the percolation limit of fcc lattice $\approx$ 20 %.

Chapter IV

Experimental results and discussion on $K_n/Na_{5.1}K_{6.9}$-LSX (x = 5.1)

The samples of K-loaded $Na_{5.1}K_{6.9}$-LSX (x = 5.1) have also been investigated. In this chapter, the experimental results of $K_n/Na_{5.1}K_{6.9}$-LSX (x = 5.1) at various loading densities will be presented. Along with discussion on physical properties of K-loaded $Na_{5.1}K_{6.9}$-LSX (x = 5.1), the comparison on the system of Na-K alloy clusters in zeolite LSX will be shown.

4.1 Experimental results of $K_n/Na_{5.1}K_{6.9}$-LSX (x = 5.1)

4.1.1 Optical properties

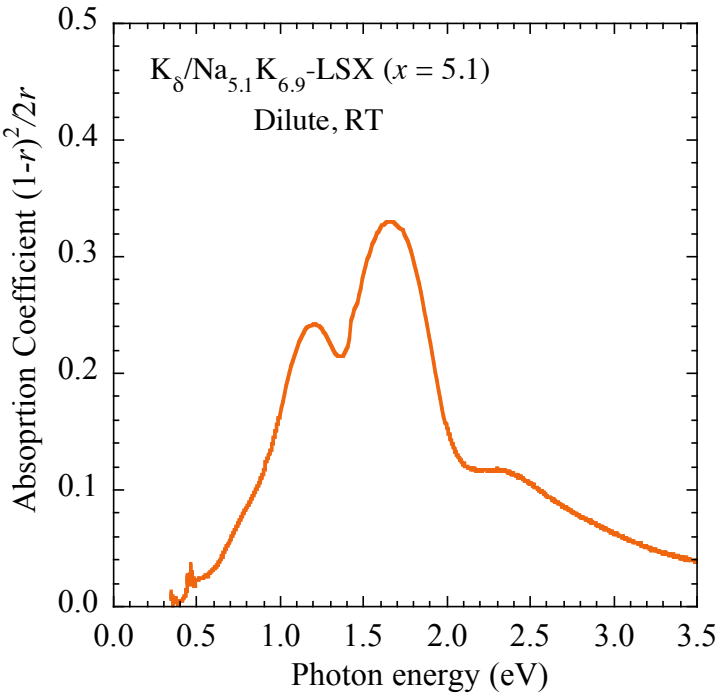

Fig. 4.1. Absorption spectrum measured at room temperature for dilute sample $K_\delta/Na_{5.1}K_{6.9}$-LSX (x = 5.1).

The optical absorption spectrum of dilute loading density sample $K_\delta/Na_{5.1}K_{6.9}$-LSX (x = 5.1) measured at room temperature is displayed in Fig. 4.1. As seen in this figure, a continuous absorption bands are observed at lower photon energy region < 2 eV. In

addition, a small shoulder was also observed at ≈ 2.4 eV. On the other hands, we also observed a sharp structure at ≈ 0.45 eV. The intensity of this structure is very weak when compare with that of main structures. This weak absorption may be caused by proton H^+ [90], which sometimes remained in zeolite after the ion-exchange procedure. The observed continuous absorption bands in the dilute sample of $x = 5.1$ is quite similar with that of K-rich samples ($x \leq 4.0$), as mentioned in chapter I. According to these results, these continuous absorption bands here is can be mainly attributed to the formation of clusters in supercage network.

Figure 4.2 shows the optical reflectance spectra of $K_n/Na_{5.1}K_{6.9}$-LSX ($x = 5.1$) measured at room temperature for various loading K-loading densities n from $n = 4.0$ to $n = 9.3$. As seen in this figure, at lower loading density samples $n = 4.0$, there is no remarkable reflection band observed in the reflectance spectra. At higher loading density sample with $n = 4.9$, a reflection band is observed at energy of ≈ 0.7 eV. This reflection band keeps its intensity up to highest loading density samples $n = 9.3$. At sample with $n = 5.9$, a reflection bands appear at energy of ≈ 2.4 eV and then grow up with increasing loading density at $n = 7.0$ and 7.8. At samples with $n = 8.1$, reflection bands at ≈ 2.4 eV becomes broader when compare with that of samples with $5.9 \leq n \leq 7.8$. At higher loading density sample $n = 8.2$, a new reflection band appears at energy of ≈ 2.8 eV. This reflection band keep the intensity when increasing the loading density up to $n = 8.9$. At highest loading density sample $n = 9.3$, the reflection band at ≈ 2.8 eV slightly increases its spectral width. The optical reflection bands at ≈ 2.4 eV and ≈ 2.8 eV, whose observed in reflectance spectra of $K_n/Na_{5.1}K_{6.9}$-LSX ($x = 5.1$), are basically assigned to the excitation of electron in β-cage clusters with different distribution of cations in zeolite framework. Similar optical reflection bands have also been observed at $x = 7.3$ samples, as shown in the previous chapter. The appearance of these reflection bands may have close relation with the formation of the magnetic moments in β-cage clusters as well as the behavior of loading density dependence of the Curie constants. The discussion for this issue will be given later in details. The sharp structures at ≈ 0.45 eV at higher loading density samples come from undesired OH absorption of the quartz glass tube.

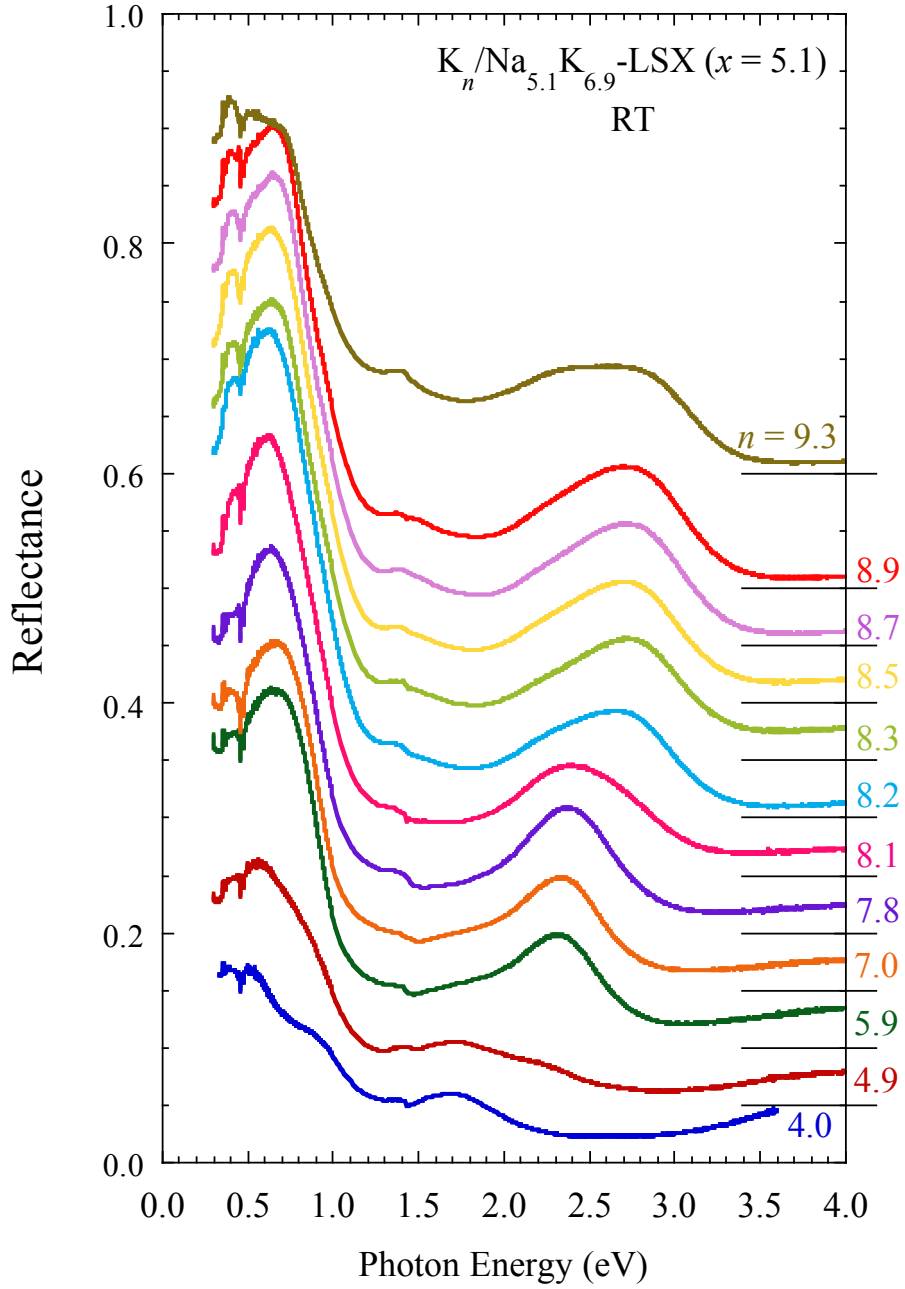

Fig. 4.2. Optical reflectance spectra of $K_n/Na_{5.1}K_{6.9}$-LSX (x = 5.1) measured at room temperature for various loading densities n.

4.1.2 Magnetic properties

Figure 4.3 exhibits the temperature dependence of magnetization, measured under weak applied magnetic field of 10 Oe, for $K_n/Na_{5.1}K_{6.9}$-LSX (x = 5.1) at various

loading densities *n*. At low loading density samples $1.2 \leq n \leq 8.1$, curves of the temperature dependence of magnetization exhibit paramagnetic properties. However at sample with $n = 8.2$, with decreasing temperature the magnetization steeply increases below ≈ 8 K and reaches the maximum value of magnetization at ≈ 3 K then decreases at lower temperature down to 1.8 K. At higher loading density samples $8.3 \leq n \leq 8.9$, similar behaviors of the temperature dependence of magnetization are observed. The temperature where the magnetization starts to increase with decreasing temperature is different for these samples. The maximum value of the magnetization is observed for the sample with $n = 8.5$ of ≈ 0.55 G at ≈ 6 K. In order to investigate more detailed in magnetic properties of these samples, an extend measurement is carried out for the samples with $n = 8.5$. By using the ^{3}He refrigerator, we measured the temperature dependence of magnetization with the temperature range down to 0.5 K. As we can see in Fig. 4.3, below 1.8 K the magnetization has the tendency to decrease with decreasing temperature down to lowest temperature of 0.5 K. The behaviors of the temperature dependence of magnetization for the samples at $8.2 \leq n \leq 8.9$ resemble the P-type or M-type ferrimagnetic properties. At highest loading density sample $n = 9.3$, we observed the paramagnetic behavior. According to above results, the ferrimagnetic properties have been observed for samples $K_n/Na_{5.1}K_{6.9}$-LSX ($x = 5.1$) at $8.2 \leq n \leq 8.9$. The mechanism of ferrimagnetic ordering in these samples will be discussed later in details.

From the temperature dependence of magnetization measured under low applied magnetic field, we estimate the asymptotic Curie temperature (T_C) for samples $K_n/Na_{5.1}K_{6.9}$-LSX ($x = 5.1$). The loading density dependence of Curie temperature is displayed in Fig. 4.4. At low loading density samples $n < 8.2$, the Curie temperature are zero because all of samples in this region show paramagnetic properties. However, we observe suddenly increase of the Curie temperature at sample with $n = 8.2$. The Curie temperature then shows a peaks at $n = 8.5$, and gradually decreases with increasing loading density. The largest Curie temperature is ≈ 12 K observed in the sample with $n = 8.5$.

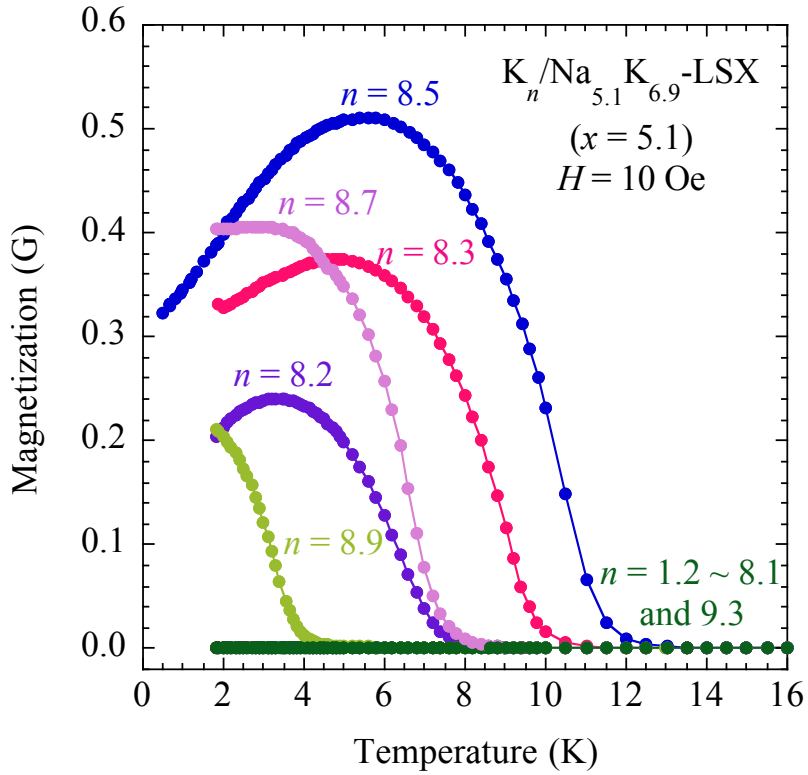

Fig. 4.3. Temperature dependence of magnetization in $K_n/Na_{5.1}K_{6.9}$-LSX (x = 5.1) measured under applied magnetic field of 10 Oe for various loading densities n.

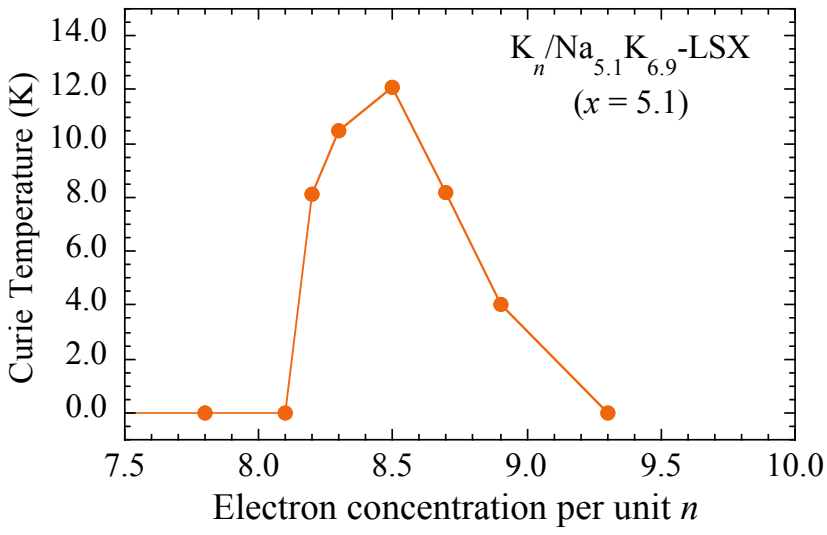

Fig. 4.4. Asymptotic Curie temperature as a function of K-loading density n for $K_n/Na_{5.1}K_{6.9}$-LSX (x = 5.1).

Magnetization curves, measured at 1.8 K with applied magnetic field up to 50 kOe, for paramagnetic samples in $K_n/Na_{5.1}K_{6.9}$-LSX (x = 5.1) are plotted in Fig. 4.5. Temperature independence magnetization component such as a diamagnetism of quartz glass tube is extracted from this plot. All of samples in Fig. 4.5, $n < 8.2$, show paramagnetic properties. As we see in this figure, the paramagnetic magnetization curves are observed for all samples. These results are coincidence with the paramagnetic properties obtained from the temperature dependence of magnetization. The magnetization increases quite linear with increasing applied magnetic field.

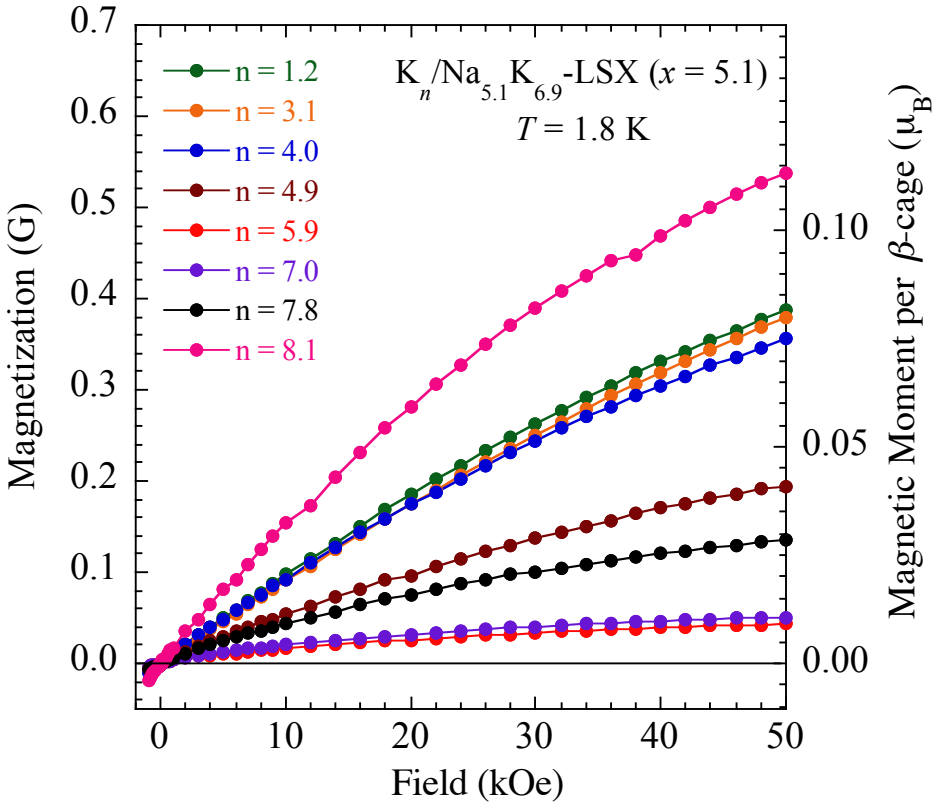

Fig. 4.5. Magnetization curves measured at 1.8 K with applied magnetic field up to 50 kOe for paramagnetic samples in $K_n/Na_{5.1}K_{6.9}$-LSX (x = 5.1) at loading density $1.2 \leq n \leq 8.1$.

Magnetization curves for ferrimagnetic samples in $K_n/Na_{5.1}K_{6.9}$-LSX (x = 5.1), however, show quite different behavior. As seen in Fig. 4.6, which plots the magnetization curves for ferrimagnetic samples ($8.2 \leq n \leq 9.3$) in $K_n/Na_{5.1}K_{6.9}$-LSX (x = 5.1) measured at 1.8 K and applied magnetic field up to 50 kOe, at low applied

magnetic field we observed a sudden increase of magnetization. Then the magnetization increases linearly with increasing the applied magnetic field. The magnetization curves of these ferrimagnetic samples do not show saturation even at highest applied magnetic field of 50 kOe. In addition, the paramagnetic behavior has been observed in the magnetization curve of sample with $n = 9.3$.

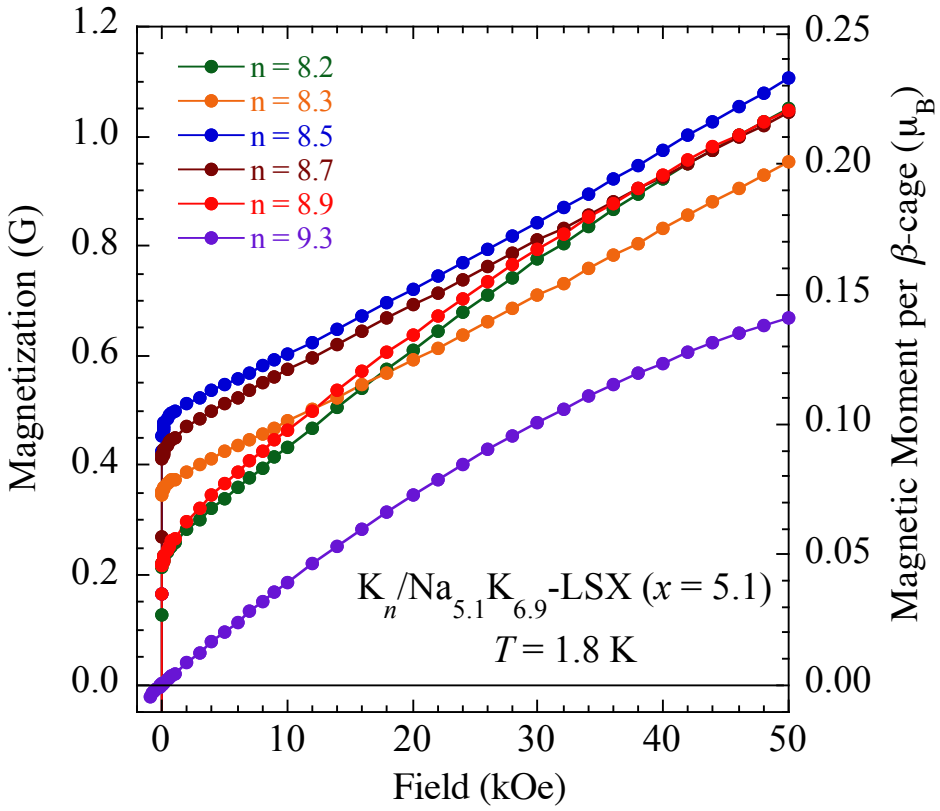

Fig. 4.6. Magnetization curves measured at 1.8 K with applied magnetic field up to 50 kOe for ferrimagnetic samples in $K_n/Na_{5.1}K_{6.9}$-LSX ($x = 5.1$) at $8.2 \leq n \leq 9.3$.

The linear increasing of magnetization curve have been observed for ferrimagnetic samples at $x = 5.1$. A separation plot of magnetization curve for sample with $n = 8.5$ is displayed in Fig. 4.7. At low applied magnetic field, the magnetization shows a quick increase. Differently with the behavior of magnetization curves, which were observed for samples at $x = 7.3$, the magnetization exhibits a linear increasing behavior even at higher applied magnetic field. This kind of magnetization curve is typically observed in ferrimagnetic materials.

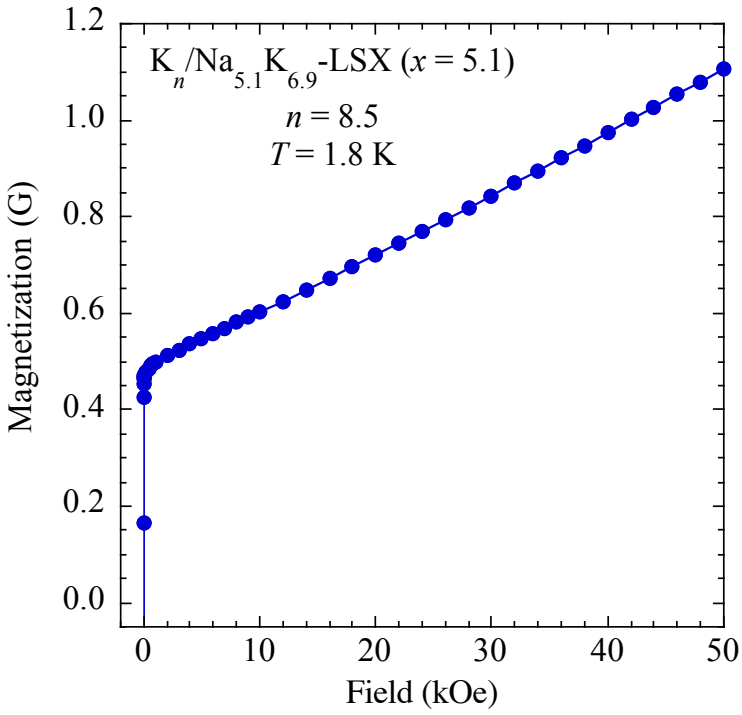

Fig. 4.7. Linear increase behavior in magnetization curves measured at 1.8 K with applied magnetic field up to 50 kOe for $K_n/Na_{5.1}K_{6.9}$-LSX (x = 5.1) at n = 8.5.

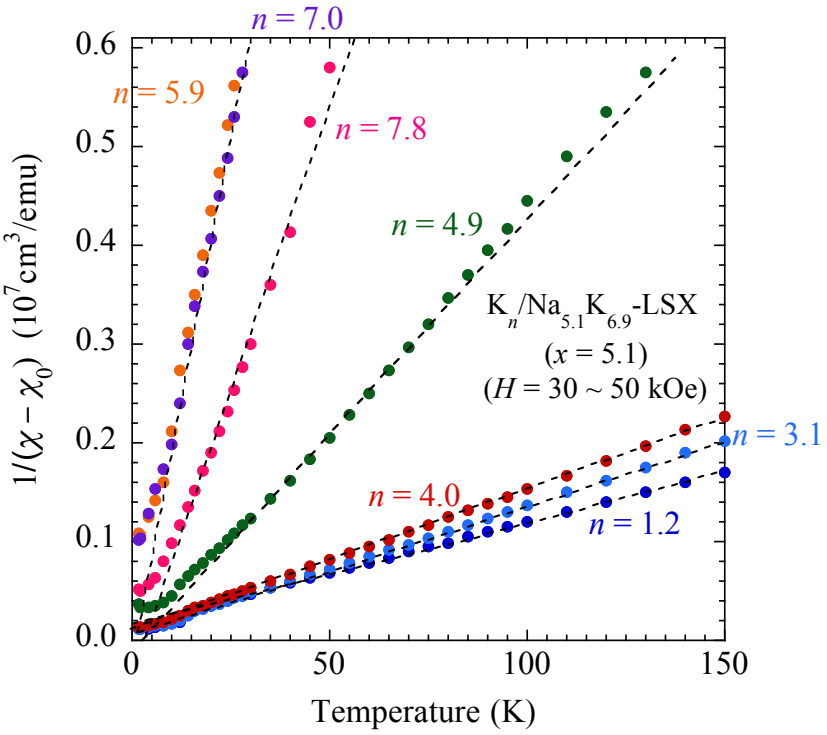

Fig. 4.8. Temperature dependence of the reciprocal of magnetic susceptibility for $K_n/Na_{5.1}K_{6.9}$-LSX (x = 5.1) at $1.2 \leq n \leq 7.8$.

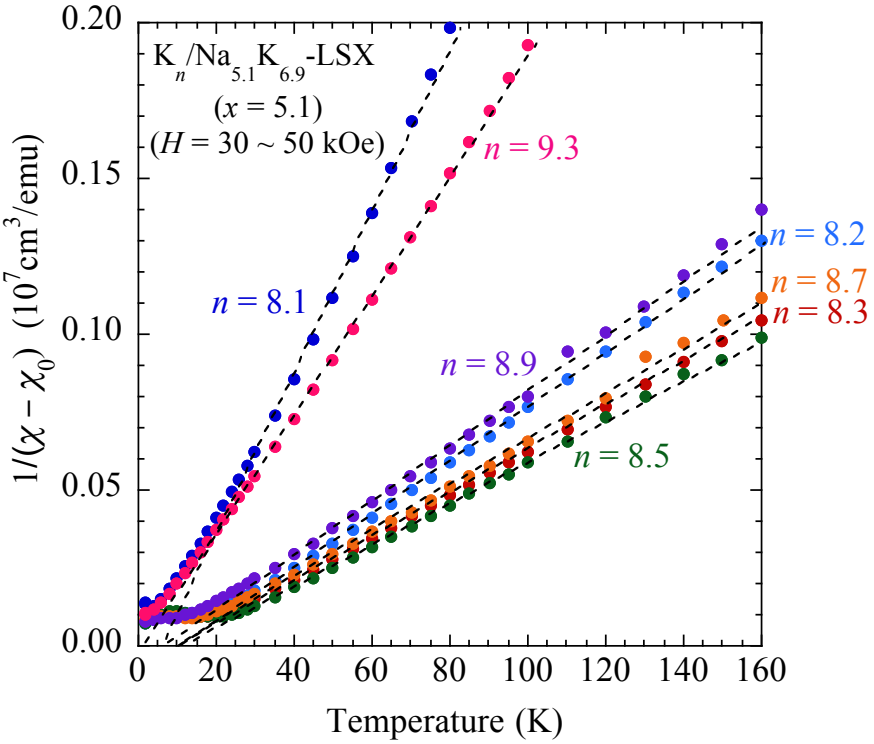

Fig. 4.9. Temperature dependence of the reciprocal of magnetic susceptibility for $K_n/Na_{5.1}K_{6.9}$-LSX (x = 5.1) at 8.1 ≤ n ≤ 9.3.

Figure 4.8 and Fig. 4.9 show the temperature dependence of the reciprocal of magnetic susceptibility for $K_n/Na_{5.1}K_{6.9}$-LSX (x = 5.1) at loading densities 1.2 ≤ n ≤ 7.8 and 8.1 ≤ n ≤ 9.3, respectively. As we can see in these figures, the reciprocal of magnetic susceptibility at higher temperature region for all samples obey the Curie – Weiss law and the broken lines are plotted together for the guide eye of the Curie – Weiss law in these samples. The observed results of reciprocal of magnetic susceptibility imply a remarkable loading density n dependence of the Curie constants.

From the temperature dependence of the reciprocal magnetic susceptibility, we estimate the Curie constant and Weiss temperature samples $K_n/Na_{5.1}K_{6.9}$-LSX (x = 5.1). Figure 4.10 shows the K-loading density n dependence of Curie constant for $K_n/Na_{5.1}K_{6.9}$-LSX (x = 5.1) at various loading densities. The dotted line corresponds to Curie constant of 50% β-cages occupied by magnetic moments with spin ½, 1.6 x 10^{-4} K·emu/cm^3. At low loading density samples, n ≤ 4.0, the Curie constants have finite values between 0.8 ~ 1 x 10^{-4} K·emu/cm^3. With increasing loading density n,

Curie constants quickly decrease down to almost zero at samples with $5.9 \leq n \leq 7.8$. At higher loading density samples $n > 7.8$, the Curie constants suddenly increase and show a narrow peak at $n = 8.5$. The maximum value of Curie constant is observed for sample at $n = 8.5$ with value of 1.51×10^{-4} K·emu/cm^3. This value is nearly approximated with value Curie constant for the case of 50% β-cages occupied by magnetic moments with spin ½. The behavior of K-loading density dependence of Curie constant in $K_n/Na_{5.1}K_{6.9}$-LSX ($x = 5.1$) at higher loading density region $n > 8$ seems to be similar with that of $K_n/Na_{7.3}K_{4.7}$-LSX ($x = 7.3$), where a sharp peak of the Curie constant has been observed. However, differently with samples $K_n/Na_{7.3}K_{4.7}$-LSX ($x = 7.3$), the Curie constant of samples $K_n/Na_{5.1}K_{6.9}$-LSX ($x = 5.1$) shows finite values at lower loading densities $n < 6$ and even at the highest loading density paramagnetic sample $n = 9.5$.

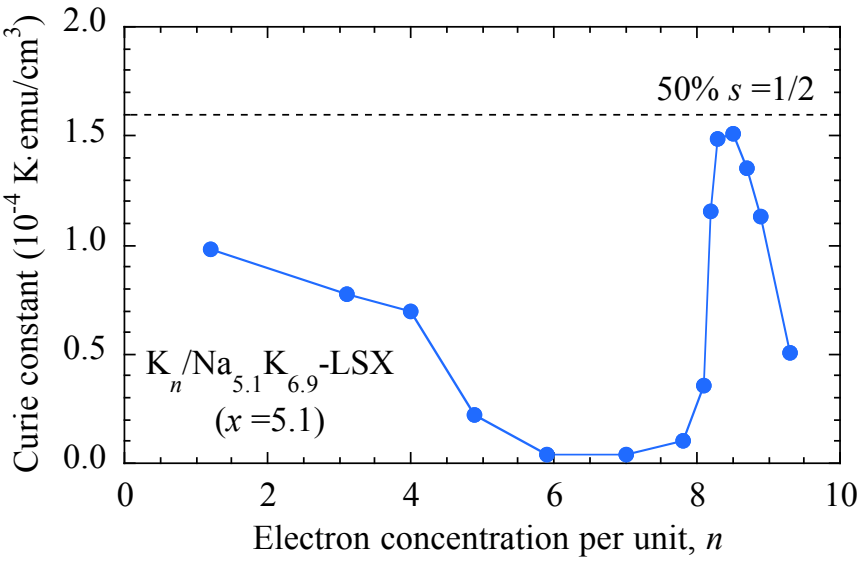

Fig. 4.10. K-loading density n dependence of the Curie constant for $K_n/Na_{5.1}K_{6.9}$-LSX ($x = 5.1$).

K-loading density n dependence of Weiss temperature for $K_n/Na_{5.1}K_{6.9}$-LSX ($x = 5.1$) is plotted in Fig. 4.11. At low loading density samples $n \leq 4.0$, Weiss temperatures have negative values. As seen in this figure, the values of Weiss temperature increase to positive value for sample witn $n > 4.0$ with increasing loading density n.

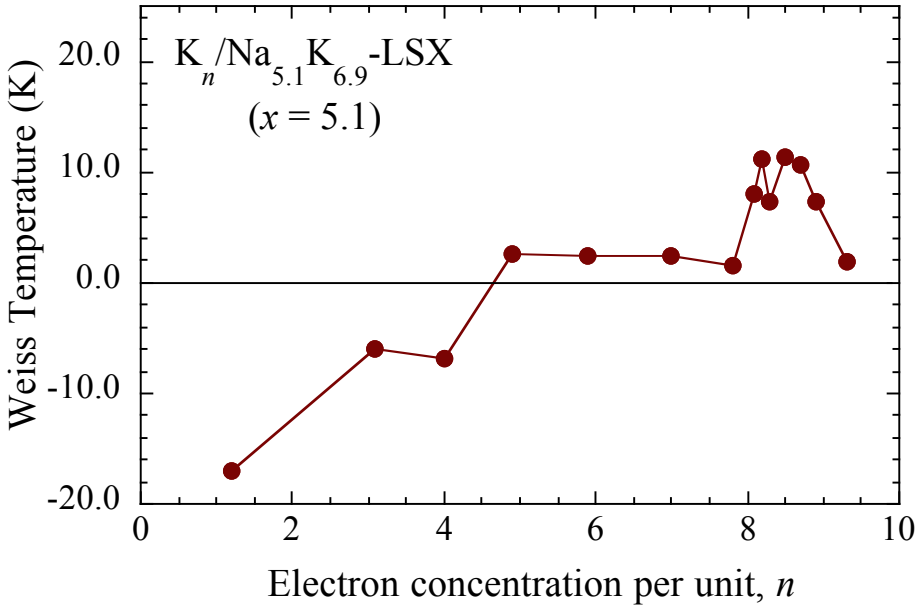

Fig. 4.11. K-loading density n dependence of the Weiss temperature for $K_n/Na_{5.1}K_{6.9}$-LSX (x = 5.1).

4.1.3 Electric transport properties

Temperature dependence of electrical resistivity ρ for $K_n/Na_{5.1}K_{6.9}$-LSX (x = 5.1) at various loading densities is plotted in Fig. 4.12. The solid circles and open circles with dots correspond to the cooling and warming process, respectively. For the sample with n = 4.0, the value of electrical resistivity is very high at room temperature, in the order larger than 10^6 Ω·cm. With decreasing temperature, the electrical resistivity steeply increases and exceeds the value of 10^9 Ω·cm below 190 K. There is nearly no deviation observed in the electrical resistivity of n = 4.0 between cooling and warming processes. At sample with n = 5.9, the value of electrical resistivity at room temperature decreases when compare with that of sample with n = 4.0. The electrical resistivity slightly increases with decreasing temperature and then shows a minimum at around 70 K. As seen in the figure, the behavior of electrical resistivity in cooling and warming process indicate that there is a thermal hysteresis at sample with n = 5.9. The origin of the thermal hysteresis is not well known at this stage. A

possibility can be considered that the thermal hysteresis relates to some structure changes, which may be caused by cations distribution.

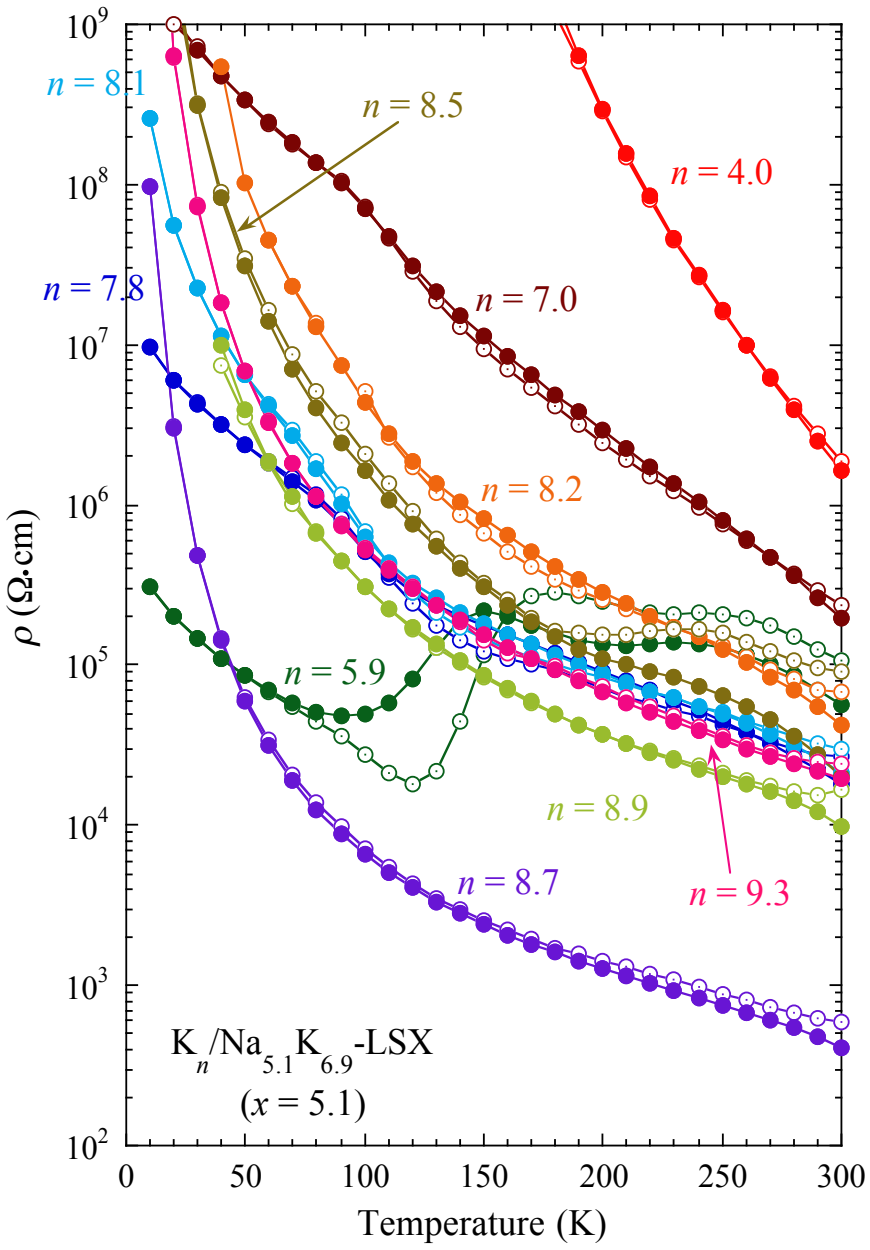

Fig. 4.12. Temperature dependence of electrical resistivity ρ for $K_n/Na_{5.1}K_{6.9}$-LSX (x = 5.1) at various loading densities measured in cooling and warming processes. The solid circles and open circles with dots correspond to the cooling and warming process, respectively.

At higher loading density samples, n = 7.0 and 7.8, the value of electrical resistivity at room temperature is still high, larger than the order of 10^5 Ω·cm. The behavior of temperature dependence of electrical resistivity in this sample is quite similar with that of sample with n = 4.0. The electrical resistivity shows linear increase behavior with decreasing temperature but a small thermal hysteresis is observed at sample with n = 7.8. The value of electrical resistivity at sample with n = 7.0 exceeds the order of 10^9 Ω·cm below 20 K, while sample at n = 7.8 has the value of electrical resistivity in the order of 10^7 Ω·cm at lowest temperature 10 K. For sample with n = 8.1, the electrical resistivity has the magnitude in the order of 10^4 Ω·cm at room temperature. With decreasing temperature, the electrical resistivity gradually increases. Below 100 K, the electrical resistivity increases more quickly and reaches the order 10^8 Ω·cm at 10 K. It is interesting that another samples at higher loading densities $8.2 \leq n \leq 9.3$ show similar behavior of the temperature dependence of electrical resistivity with sample n = 8.1. These samples, except n = 8.7, have the value of electrical resistivity in the order between 10^4 Ω·cm and 10^5 Ω·cm at room temperature. A significant decrease of the value of electrical resistivity, in the order of 10^3 Ω·cm, is observed at sample with n = 8.7. At low temperature region, the values of electrical resistivity of all samples are very high, in the order larger than 10^8 Ω·cm. According to above results of electrical resistivity for samples in $K_n/Na_{5.1}K_{6.9}$-LSX (x = 5.1), although samples show differences in magnitude of the electrical resistivity as well as the behavior of the temperature dependence but basically all of samples, including ferrimagnetic samples ($8.2 \leq n \leq 8.9$), are in insulating state.

4.2 Discussion on $K_n/Na_{5.1}K_{6.9}$-LSX (x = 5.1)

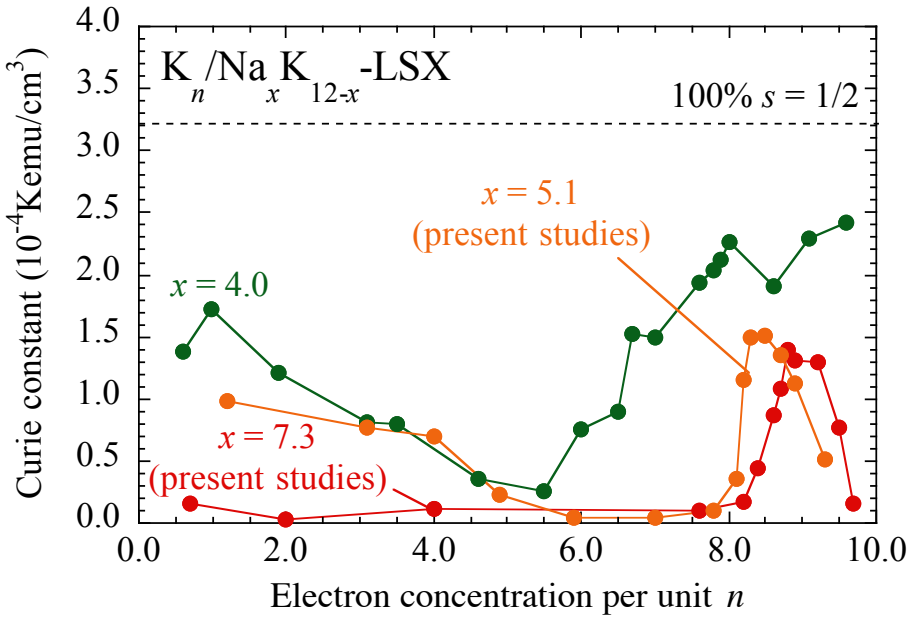

Fig. 4.13. K-loading density dependence of Curie constant for K_n/Na_4K_8-LSX (x = 4.0), $K_n/Na_{5.1}K_{6.9}$-LSX (x = 5.1) and $K_n/Na_{7.3}K_{4.7}$-LSX (x = 7.3).

As mentioned above, we observed the ferrimagnetic properties for $K_n/Na_{5.1}K_{6.9}$-LSX (x = 5.1) at $8.2 \leq n \leq 8.9$. In order to understand the ferrimagnetic properties in these samples, discussions on magnetic properties related optical properties and electrical transport properties for $K_n/Na_{5.1}K_{6.9}$-LSX (x = 5.1) will be given in this section. Figure 4.13 displays the K-loading density dependence of Curie constant for K-rich sample K_n/Na_4K_8-LSX (x = 4.0), intermediate sample $K_n/Na_{5.1}K_{6.9}$-LSX (x = 5.1) and Na-rich sample $K_n/Na_{7.3}K_{4.7}$-LSX (x = 7.3). As described in previous section, the finite values of Curie constants observed for x = 4.0 and x = 5.1 at $n < 6$ indicate that there is formation of magnetic moments in these samples. On the other hand, in optical reflectance spectra, there is no indication of clusters formed in β-cages. The finite values of Curie constants at lower loading density region can be caused by the magnetic moments, which is formed in supercage clusters. At higher loading density region $n > 6$, however, quite different behaviors of the loading density dependence of Curie constants are observed between x = 4.0 and x = 5.1 samples. In the case of x = 4.0, the Curie constants increase with increasing the loading density at $n > 6$. In

addition a clear increasing component, which guided by the broken line, is observed for samples x = 4.0. This component appears coincident with the observed N-type ferrimagnetic properties at $6.7 \leq n \leq 8.0$. The N-type ferrimagnetic ordering requires two magnetic sublattices. A model of non-equivalent magnetic sublattices was used to explain the N-type ferrimagnetic properties for samples at x = 4.0. In this model, the authors proposed two magnetic sublattices coupled with antiferromagnetic interaction, one of which form the itinerant electron network in supercage clusters and the other has the localized magnetic moments in β-cage clusters. The increasing in the Curie constants for samples x = 4.0 at $n > 6$ with additional increasing component can be attributed to the formation magnetic moments in both supercage and β-cage clusters.

For samples x = 5.1 at $n > 6$, the Curie constants are almost zero at $6 < n < 8$, then suddenly increase at $n > 8$, showing a narrow peak at n = 8.5 and decrease at higher loading density samples. The maximum value of Curie constant is approximately 50 % β-cage clusters occupied by magnetic moments with spin ½. This behavior of the Curie constant is also observed for higher Na-concentration samples x = 7.3, which is seen in Fig. 4.13. The samples at x = 7.3 show nearly pure ferromagnetism at specific region of loading density n. The ferromagnetic properties are provided by the superexchange interaction between magnetic moments in β-cage clusters through closed-shell nonmagnetic supercage clusters network. The increasing and decreasing of the Curie constants for samples x = 5.1 indicate that the magnetic moments were generated in samples x = 5.1 and may relate to the appearance of reflection bands at ≈ 2.4 and ≈ 2.8 eV in reflectance spectra. If we assume the spherical potential well with the diameter of β-cage 7.5 Å, the estimated kinetic energy of electron in 1s and 1p-state are 2.7 and 5.5 eV, respectively. Therefore the optical excitation energy of a free electron from 1s- to 1p-state will be 2.8 eV. The energy of reflection bands, which is mentioned above, is very close to this value. Hence the reflection bands in reflectance spectra for samples x = 5.1 at higher loading density region is mainly assigned to the excitation of electrons in β-cage clusters. According to the experimental results from magnetic and optical properties, the localized magnetic moments are thought to be formed only in β-cage clusters network for samples x = 5.1 at higher loading density region, where we observed the ferrimagnetic properties. At this stage, we met a challenge for understanding the magnetic properties for samples x = 5.1. We obviously observed the ferrimagnetic properties for samples x = 5.1 at $8.2 \leq n \leq 8.9$.

In this region we obtained the increasing and decreasing of the Curie constants, which assigned to the formation of magnetic moments in *β*-cage clusters. How does the ferrimagnetic ordering appear in samples $x = 5.1$.

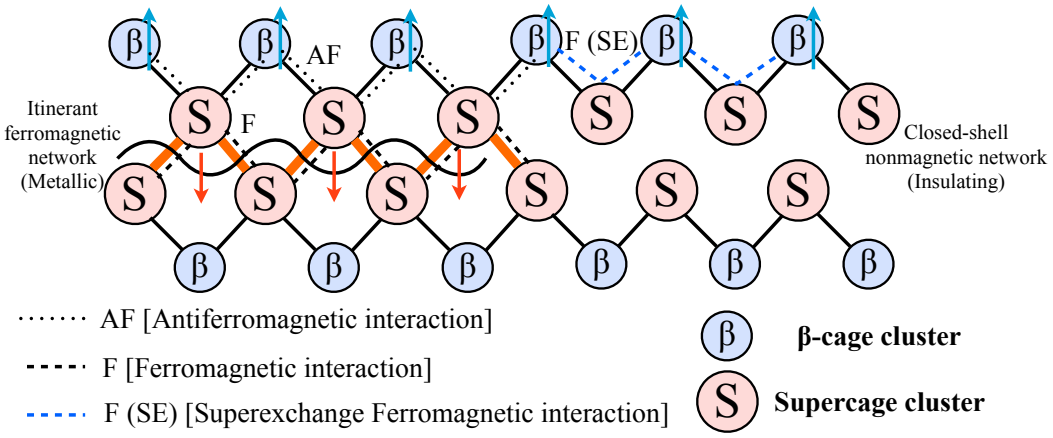

Fig. 4.14. Geometry schematic illustration for ferrimagnetic interaction and superexchange ferromagnetic interaction in zeolite LSX sample. AF, F and F (SE) stand for Antiferromagnetic, Ferromagnetic and Superexchange Ferromagnetic interaction, respectively. The magnetic interaction in the case of sample $K_n/Na_{5.1}K_{6.9}$-LSX ($x = 5.1$) seems to be a mixture state of these two magnetic interactions.

In order to clarify the origin of ferrimagnetic properties in samples $x = 5.1$, it is essentially to mention the electrical transport properties and formation of magnetic ordering in vicinity samples with $x = 5.1$ such as $x = 4.0$ and $x = 7.3$. The electrical resistivity measurements in zeolite LSX show us the electrical transport properties of supercage cluster network, where supercages are connected to each other via 12-membered rings. It provides us important information for discussing the magnetic properties of samples. For the case of samples $x = 4.0$, we found clear N-type ferrimagnetic properties. The results of electrical resistivity measurements show that these samples are in metallic state [65]. The supercage clusters are in metallic state at higher loading density samples at K-rich clusters. Hence, the supercage clusters are proposed to be itinerant ferromagnetic network since metallic properties, while *β*-cage

clusters network has localized magnetic moments. The antiferromagnetic coupling between localized magnetic moments in β-cage clusters network and itinerant ferromagnetic network in supercage clusters leads to N-type ferrimagnetism in samples x = 4.0. In case of samples x = 7.3, nearly pure ferromagnetic and insulating properties were observed. Supercage clusters are proposed to be a closed-shell nonmagnetic network. The localized magnetic moments can be generated in β-cage clusters network at higher loading density region. A model of superexchange interaction between localized magnetic moments in β-cage clusters network via closed-shell nonmagnetic network in supercage clusters has been considered in order to eplain the origin of neary pure ferromagnetism in samples x = 7.3. A geometry schematic illustration for the ferrimagnetic interaction and superexchange ferromagnetic interaction is plotted in Fig. 4.14.

Return to the case of samples with x = 5.1, we observed insulating behavior for all samples. The suddenly changing from metallic properties at x = 4.0 to insulating properties at x = 5.1 may be caused by the role of the fifth Na^+ cations. As mentioned earlier the electrical transport properties of whole sample are mainly determined by electrical transport state of supercage clusters network. This indicate that with increasing only one Na^+ cation in framework of zeolite LSX from x = 4.0 to x = 5.1, supercage clusters network suddenly changed from metallic to insulating property. In order to explain this issue, it is necessary to assume that the fifth Na^+ cation stabilized Na-rich clusters in the supercage clusters network in case of x = 5.1. In addition, the distribution of Na^+ cation may be inhomogeneous. In order to explain the ferrimagnetic properties in samples x = 5.1, where the localized magnetic moments formed in β-cage clusters network and insulating behavior of supercage clusters network, we propose a possibility of Anderson localization for the supercage clusters network. In principle the system with Anderson localization has insulating behavior and nonmagnetic state. However in real system, such as in the case of zeolite LSX, if the system has strong electron correlation, we can expect a state for Anderson localization ferromagnetic network in supercage clusters. In this scene, the magnetic properties in samples x = 5.1 will be disorder ferrimagnetism. The magnetic interaction, which provides disorder ferrimagnetic properties in samples x = 5.1, may be a mixture or co-existence of magnetic interaction between the case of x = 4.0 and x = 7.3.

The magnetic properties, the electric transport properties as well as the formation of magnetic moments in the case of samples with x = 4.0, 5.1 and 7.3 are summarized in Table 4.1.

Table 4.1. Summary of magnetic properties of K_n/Na_4K_8-LSX (x = 4.0), $K_n/Na_{5.1}K_{6.9}$-LSX (x = 5.1) and $K_n/Na_{7.3}K_{4.7}$-LSX (x = 7.3).

Na concentration	**x = 4.0**	**x = 5.1 (present studies)**	**x = 7.3 (present studies)**
Supercage cluster network	Itinerant ferromagnetic network (Metallic)	Anderson localization ferromagnetic network (Insulating)	Closed-shell nonmagnetic network (Insulating)
β-cage cluster network	Localized Magnetic Moment	Localized Magnetic Moment	Localized Magnetic Moment
Magnetic properties	N-type Ferrimagnetic	Disorder Ferrimagnetic	Nearly Pure Ferromagnetic

4.3 Overview of the system of Na-K alloy clusters in zeolite LSX

As mentioned earlier, the system of Na-K alloy clusters in zeolite LSX previously has been studied by K-loading on Na_xK_{12-x}-LSX with lower Na-concentration (K-rich) samples $0 \le x \le 4.0$ [64-67]. In the present studies, we have investigated the properties of Na-K alloy clusters at higher Na-concentration (Na-rich) sample by K-loading on $Na_{7.3}K_{4.7}$-LSX (x = 7.3) and an intermediate Na-concentration sample $Na_{5.1}K_{6.9}$-LSX (x = 5.1), which is can be called as intermediate sample hereafter. In this section, we are going to make a briefly comparison on the physical properties between the previous ($0 \le x \le 4.0$) [66], the present (x = 5.1 and 7.3) studies and the higher x = 7.8 [91] in order to have a more clearly understanding on the present studies as well as the whole system.

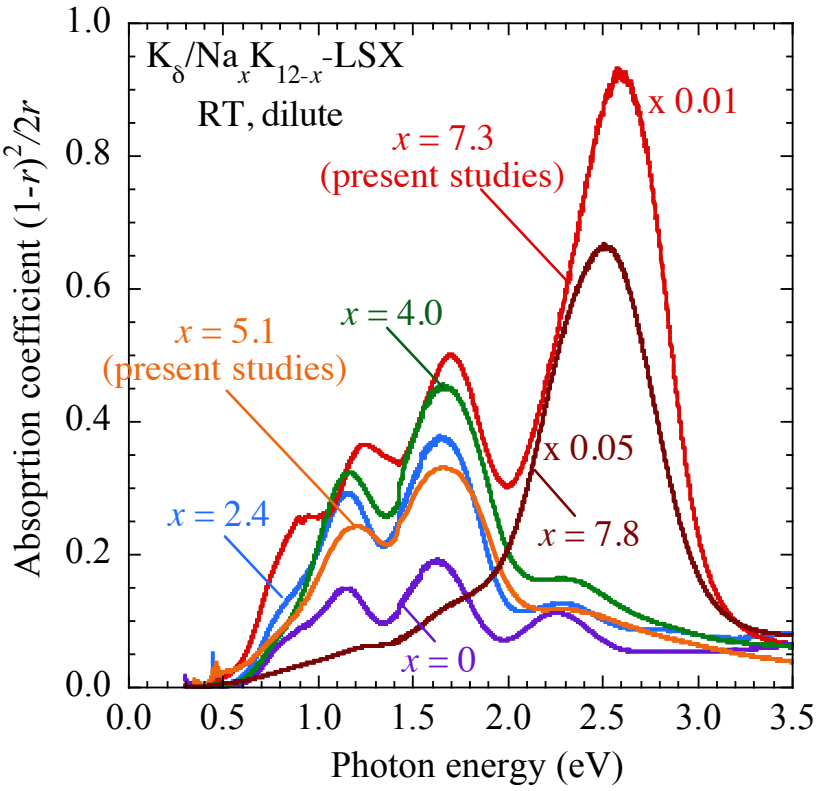

Fig. 4.15. Absorption spectra measured at room temperature for dilute samples K_δ/Na_xK_{12-x}-LSX for x = 0, 2.4, 4.0, 5.1, 7.3 and 7.8.

The optical absorption spectra at dilute loading density δ of the present Na-rich sample $K_\delta/Na_{7.3}K_{4.7}$-LSX (x = 7.3), intermediate sample $K_\delta/Na_{5.1}K_{6.9}$-LSX (x = 5.1) and the previous K-rich samples $K_\delta/Na_{4.0}K_{8.0}$-LSX (x = 4.0), $K_\delta/Na_{2.4}K_{9.6}$-LSX (x =

2.4), K_δ/K_{12}-LSX (x = 0) as well as $K_\delta/Na_{7.8}K_{4.2}$-LSX (x = 7.8) are plotted together in Fig. 4.15 for comparison. As mentioned earlier, at low photon energy region the optical absorption spectra of the previous K-rich samples ($x \leq 4.0$) show continuous absorption bands, which are attributed to the supercage clusters. There is no evidence for the formation of clusters in β-cage.

In the present studies, the optical absorption spectrum of intermediate sample x = 5.1 exhibits quite similar continuous absorption bands with that of previous K-rich samples ($x \leq 4.0$). However at Na-rich sample $K_\delta/Na_{7.3}K_{4.7}$-LSX (x = 7.3), a clear absorption appears at ≈ 2.6 eV, which is assigned to the excitation of s-electron in β-cage clusters. Differently with K-rich samples ($x \leq 4.0$) and intermediate sample x = 5.1, Na-rich sample $K_\delta/Na_{7.3}K_{4.7}$-LSX (x = 7.3) exhibit the coexistence of supercage and β-cage clusters. At K-rich samples ($x \leq 4.0$) and intermediate sample x = 5.1, the s-electron of guest K atoms has the tendency to occupy quantum states of supercage clusters due to lower kinetic energy. The β-cage clusters in these samples may be K-rich clusters, and they have higher kinetic energy for occupation of s-electron. The situation, however, is quite different at Na-rich sample $K_\delta/Na_{7.3}K_{4.7}$-LSX (x = 7.3). Since the larger number of Na^+ cations in the framework of zeolite LSX, the Na^+ cations can be distributed at cation sites in both of supercage and β-cage. Accutally Na^+ cations are preferred to occupy cation sites I and I' inside β-cage. Another Na^+ cations will be located at cation site II. All of these cation sties can influence the electronic potential of β-cage clusters. If the Na^+ cations are larger enough to deepen the well potential of β-cage, then s-electrons can be trapped here and form clusters as observed at dilute loading density sample $K_\delta/Na_{7.3}K_{4.7}$-LSX (x = 7.3).

The sample at higher Na-concentration $K_n/Na_{7.8}K_{4.2}$-LSX (x = 7.8) recently has been studied [91]. The optical absorption spectra of dilute sample $K_\delta/Na_{7.8}K_{4.2}$-LSX (x = 7.8) exhibit a single absorption band at around 2.6 eV, which is similarly observed at dilute loading density sample $K_\delta/Na_{7.3}K_{4.7}$-LSX (x = 7.3). The result suggests that the cluster is generated in only β-cage at $K_\delta/Na_{7.8}K_{4.2}$-LSX (x = 7.8).

In Fig. 4.16, the typical temperature dependence of magnetization (M-T) measured under a weak applied magnetic field of 10 Oe for the previous K-rich samples K_n/Na_xK_{12-x}-LSX ($x \leq 4.0$), the present intermediate sample $K_n/Na_{5.1}K_{6.9}$-LSX (x = 5.1), Na-rich sample $K_n/Na_{7.3}K_{4.7}$-LSX (x = 7.3) and the highest Na-concentration

sample $K_n/Na_{7.8}K_{4.2}$-LSX (x = 7.8) are displayed together. The samples are selected for whose have the highest Curie temperatures. As seen in this figure, all of samples show spontaneous magnetization at low temperature region.

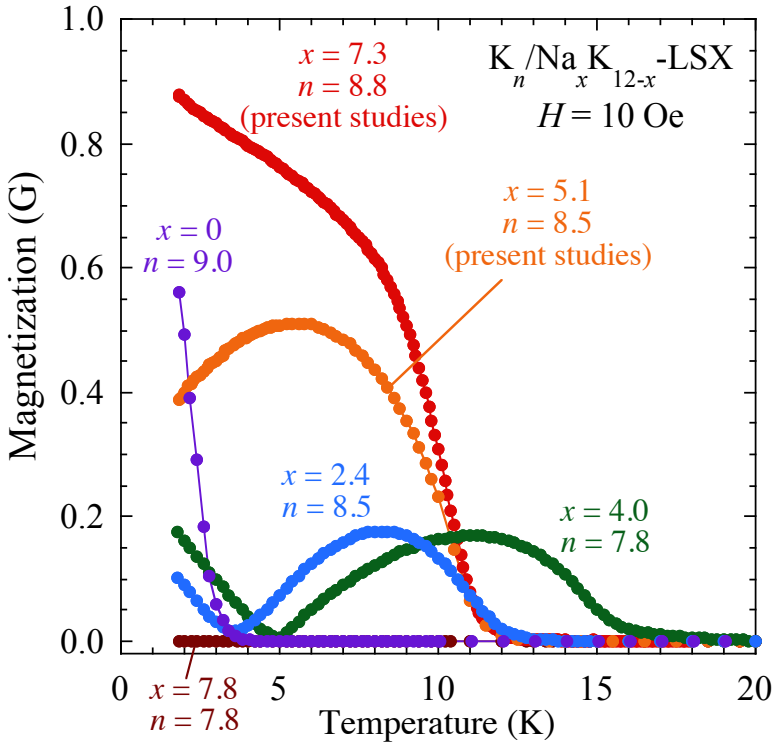

Fig. 4.16. Typical temperature dependence of magnetization measured under a weak applied magnetic field of 10 Oe of K_n/Na_xK_{12-x}-LSX for x = 0, 2.4, 4.0, 5.1, 7.3 and 7.8. The value of loading density n is chosen for the highest Curie temperature sample.

For the previous K-rich samples K_n/Na_xK_{12-x}-LSX ($x \leq 4.0$), N-type ferrimagnetic properties have been observed for samples with x = 2.4 and x = 4.0, and sample with x = 0 show ferrimagnetism with different kind of M-T curves. The ferrimagnetic properties in K-rich samples K_n/Na_xK_{12-x}-LSX ($x \leq 4.0$) can be explained by a model of two nonequivalent magnetic sublattices in supercage and β-cage clusters networks coupled antiferromagnetically. The supercage clusters behaves nearly itinerant ferromagnetism network while localized magnetic moments are stabilized in β-cage clusters network. Electrons in supercage and β-cage clusters networks can have

antiferromagnetic interaction through the sharing window between supercage and *β*-cage.

At higher higher Na-concentration sample, the present studies have showed that intermediate sample $K_n/Na_{5.1}K_{6.9}$-LSX (x = 5.1) still exhibits the ferrimagnetic properties. However the Na-rich sample $K_n/Na_{7.3}K_{4.7}$-LSX (x = 7.3) does not show ferrimagnetic properties but nearly pure ferromagnetic property. The ferromagnetism for sample with x = 7.3 has been explained by model of superexchange interaction between localized magnetic moments in *β*-cage clusters network via closed-shell state of supercage clusters. These results obviously indicate that the magnetic properties in K_n/Na_xK_{12-x}-LSX samples system strongly depend on Na-concentration x as well as K-loading density n. With increasing Na-concentration the electronic states and the potential balance between supercage and *β*-cage clusters have been changed, leading to the variation of magnetic properties as observed from experimental results. At the highest Na-concentration sample $K_n/Na_{7.8}K_{4.2}$-LSX (x = 7.8), there is no evidence for the magnetic ordering at any value of K-loading density n.

In addition, the magnetization curves of mentioned above samples also exhibit different behaviors. Figure 4.17 displays typical magnetization curves for the previous K-rich samples K_n/Na_xK_{12-x}-LSX ($x \leq 4.0$), the present intermediate sample $K_n/Na_{5.1}K_{6.9}$-LSX (x = 5.1), Na-rich sample $K_n/Na_{7.3}K_{4.7}$-LSX (x = 7.3) and the highest Na-concentration sample $K_n/Na_{7.8}K_{4.2}$-LSX (x = 7.8) measured at 1.8 K with applied magnetic field up to 50 kOe. For K-rich samples $x \leq 4.0$, the magnetization abruptly increases at lower applied magnetic field, then the magnetization linearly increases at higher applied magnetic field. The magnetization curves of these samples do not exhibit saturation behavior even at the highest applied magnetic field of 50 kOe. The linear increase behavior of the magnetization curve is typically observed in the ferrimagnetic materials.

Similarly with the previous samples x = 2.4 and 4.0, the present intermediate sample $K_n/Na_{5.1}K_{6.9}$-LSX (x = 5.1) also display linear increase behavior in the magnetization curve. This result coincides with ferrimagnetic properties observed in sample with x = 5.1. The magnetization curve of ferromagnetic Na-rich sample x = 7.3 displays quite different behavior. At lower applied magnetic field, the magnetization also suddenly increases. However, oppositely with K-rich samples $x \leq 4.0$ and intermediate sample x

= 5.1, at higher applied magnetic field, the magnetization curve of Na-rich sample x = 7.3 seems to be saturation. This kind of behavior of magnetization curve is characteristic for ferromagnetic materials. At x = 7.8, the paramagnetic magnetization curve can be seen.

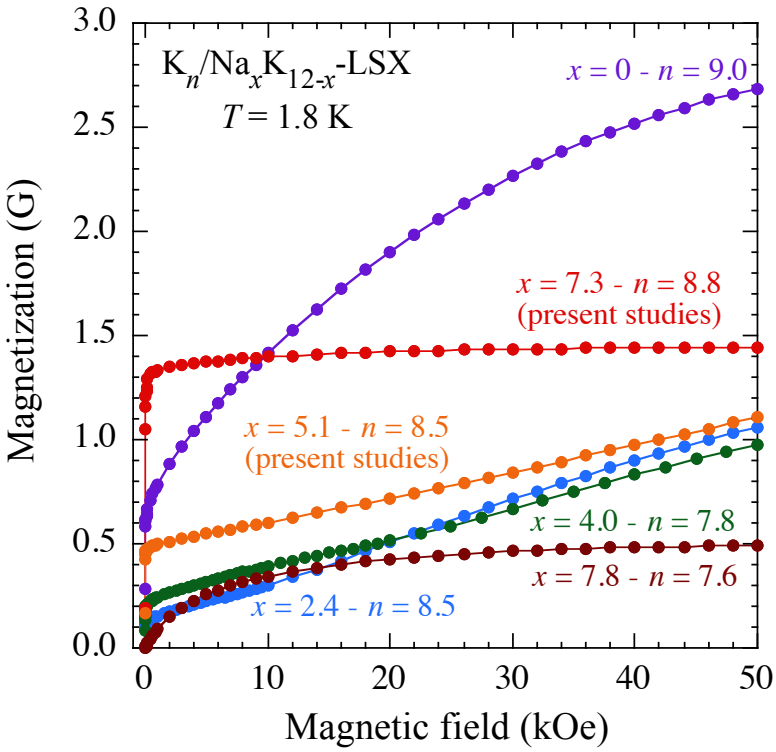

Fig. 4.17. Typical magnetization curves measured at 1.8 K with applied magnetic field up to 50 kOe of K_n/Na_xK_{12-x}-LSX for x = 0, 2.4, 4.0, 5.1, 7.3 and 7.8.

The K-loading density dependence of Curie temperature of previous K-rich samples K_n/Na_xK_{12-x}-LSX ($x \leq 4.0$), the present intermediate sample $K_n/Na_{5.1}K_{6.9}$-LSX (x = 5.1), Na-rich sample $K_n/Na_{7.3}K_{4.7}$-LSX (x = 7.3) and the highest Na-concentration sample $K_n/Na_{7.8}K_{4.2}$-LSX (x = 7.8) is shown in Fig. 4.18. For K-rich samples $x \leq 4.0$, the ferrimagnetic phases have been observed at $8.7 \leq n \leq 9.2$, $7.5 \leq n \leq 9.4$ and $6.7 \leq n \leq 8.0$ for x = 0, 2.4 and 4.0, respectively. The ferrimagnetic phase systematically shift to lower K-loading density region with increasing Na-concentration x. The shifting of ferrimagnetic phase can be explained by the ability to enter β-cage of electrons.

However at higher Na-concentration, in the present intermediate sample $K_n/Na_{5.1}K_{6.9}$-LSX (x = 5.1), the ferrimagnetic phase shifts to higher K-loading density region 8.2 ≤ n ≤ 8.9. In addition the ferromagnetic phase of Na-rich sample $K_n/Na_{7.3}K_{4.7}$-LSX (x = 7.3) has been observed at 8.6 ≤ n ≤ 9.5. These results clearly show that above x = 4.0, the magnetic phase has the tendency to shift to higher K-loading density region with increasing Na-concentration. The Curie temperature are almost zero at x = 7.8 due to no magnetic ordering of samples at all K-loading densities.

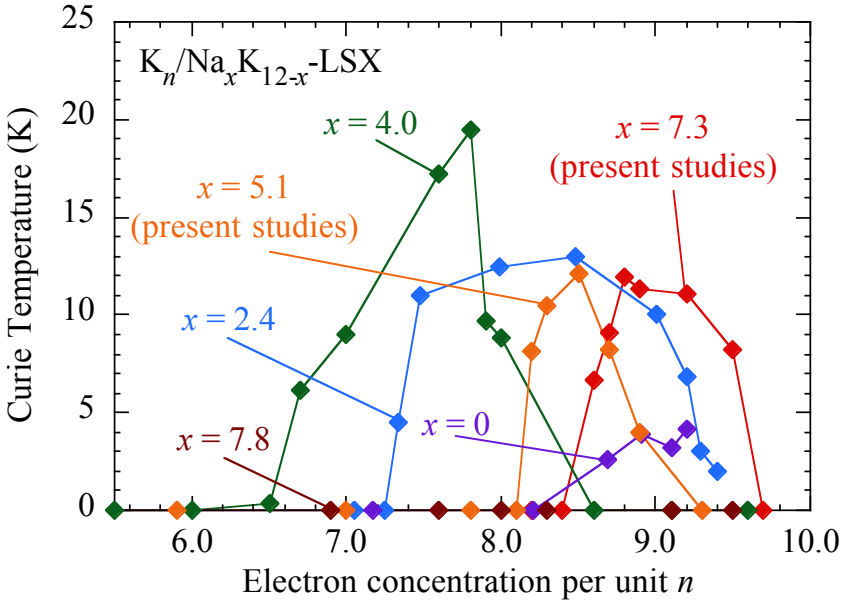

Fig. 4.18. Curie temperature as a function of K-loading density n of K_n/Na_xK_{12-x}-LSX for x = 0, 2.4, 4.0, 5.1, 7.3 and 7.8.

The Curie constants of the previous K-rich samples K_n/Na_xK_{12-x}-LSX (x ≤ 4.0), the present studies intermediate sample $K_n/Na_{5.1}K_{6.9}$-LSX (x = 5.1), Na-rich sample $K_n/Na_{7.3}K_{4.7}$-LSX (x = 7.3) and the highest Na-concentration sample $K_n/Na_{7.8}K_{4.2}$-LSX (x = 7.8) are plotted as a function of K-loading density n in the Fig. 4.19. Larger differences have been observed in the behavior of K-loading density dependence between the previous and the present studies. For the previous K-rich samples x ≤ 4.0, the Curie constant has finite values at lower loading density region. At the loading density n ~ 3, the sharp peak is observed in the Curie constant of K-rich samples x ≤

4.0. This peak eventually is explained by the polaron effect including electron correlation as mentioned earlier. At higher loading density, the Curie constant slightly decreases and then increases at loading density $n > 6$. That means at lower loading density region, there are evidences for the formation of magnetic clusters in these samples. In addition, the optical reflectance spectra pointed out that there is no sign of β-cage clusters at lower loading density $n < 6$. Therefore, finite values of Curie constant in this region can be attributed to the magnetic moments in supercage clusters network. In the loading density region, where ferrimagnetic phase is observed, the values Curie constant are comparable with nearly 100% of β-cages are occupied by magnetic moment with spin ½. In the ferrimagnetic phase, the magnetic moments are assumed to realize in both of supercage and β-cage clusters network in order to explain the ferrimagnetic properties.

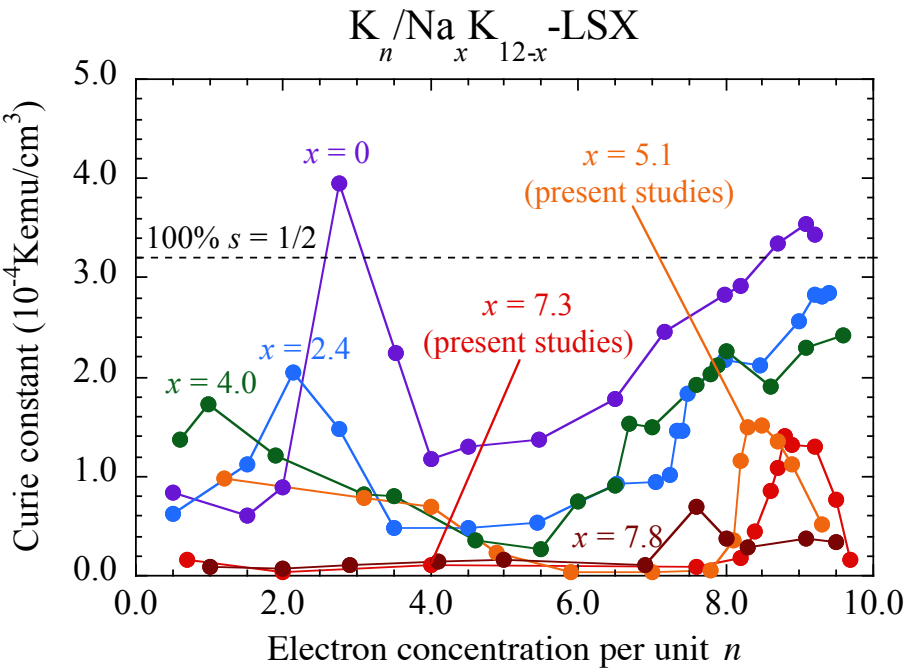

Fig. 4.19. Curie constant as a function of K-loading density n of K_n/Na_xK_{12-x}-LSX for $x = 0$, 2.4, 4.0, 5.1, 7.3 and 7.8.

In the present studies, the intermediate sample $x = 5.1$, the K-loading density dependence of the Curie constant exhibit quite interesting behavior. At low loading density, $n < 6$, finite values of the Curie constant have been observed. This implies that there is amount of magnetic moments were formed in these samples. The

magnetic moments are probably realized in supercage clusters network because there is no evidence for the formation β-cage cluster in optical spectra of these samples. This behavior seems to be similar with the case of K-rich samples $x \leq 4.0$. At $6 < n < 8$, however, the values of the Curie constant are almost zero. And at $n > 8$, the Curie constant shows an increase and decrease behavior. Differently with lower K-loading density region, at higher one, the Curie constant varies similar with that of Na-rich sample $x = 7.3$. Interestingly the behavior of K-loading density dependence of Curie constant of intermediate sample $x = 5.1$ seems to be a crossover like between K-rich samples $x \leq 4.0$ and Na-rich sample $x = 7.3$.

For Na-rich sample $x = 7.3$, the value of Curie constant at lower loading density region $n < 8$ are almost zero. This result indicates that the magnetic moments do not exist in this loading density region. All of clusters are formed in the sample should be in spin singlet state. At higher loading density $n > 8$, the increasing and decreasing of Curie constant have been observed. The Curie constant displays a narrow peak at loading density $n \sim 9$. Simultaneously in the optical reflectance spectra, a growth of reflection band at ≈ 2.8 eV, which is assigned to the excitation of s-electron between quantum states of β-cage clusters, has been found. Hence the increasing and decreasing of Curie constant are attributed to the formation of spin doublet clusters in β-cage network. The maximum value of the Curie constant at Na-rich sample $x = 7.3$ just corresponds to 45% occupancy of magnetic moment in β-cage clusters network. A hypothesis of coexistence of spin singlet and doublet clusters in β-cage network has been considered. The inhomogeneous distribution of Na^+ cations in Na-rich sample $x = 7.3$, in which some β-cage clusters have enough Na^+ cations to stabilize singlet clusters despite of strong Coulomb repulsion between two electrons in narrow space and some other β-cage clusters are lack of Na^+ cations to do that. This possibility can be used to explain the increasing and decreasing of Curie constant as well as its values. At $x = 7.8$, even a slight increase of the Curie constant at $n = 7.8$ but the Curie constant are basically very small at all K-loading density. In addition, there is no observation of magnetic ordering at $x = 7.8$. These results indicate that the spin-singlet clusters are stabilized at all loading density at $x = 7.8$. The summary on the magnetic properties of this samples system is given in Table 4.2.

Table 4.2. Magnetic properties of K_n/Na_xK_{12-x}-LSX, where x = 0, 1.0, 1.5, 2.4, 4.0, 5.1 and 7.3.

Sample name	Na-concentration	Magnetic property	Magnetic phase
$K_n/Na_{7.8}K_{4.2}$-LSX	x = 7.8	Non-magnetic	- - - - - - - - - - - -
$K_n/Na_{7.3}K_{4.7}$-LSX (present studies)	x = 7.3	Nearly pure ferromagnetic	$8.6 \leq n \leq 9.5$
$K_n/Na_{5.1}K_{6.9}$-LSX (present studies)	x = 5.1	Disorder ferrimagnetic	$8.2 \leq n \leq 8.9$
$K_n/Na_{4.0}K_{8.0}$-LSX	x = 4.0	N-type ferrimagnetic	$6.7 \leq n \leq 8.0$
$K_n/Na_{2.4}K_{9.6}$-LSX	x = 2.4	N-type ferrimagnetic	$7.5 \leq n \leq 9.4$
$K_n/Na_{1.5}K_{10.5}$-LSX	x = 1.5	Ferrimagnetic	$8.0 \leq n \leq 9.2$
$K_n/Na_{1.0}K_{11.0}$-LSX	x = 1.0	Ferrimagentic	$8.25 \leq n \leq 9.2$
$K_n/K_{12.0}$-LSX	x = 0	Ferrimagnetic	$8.7 \leq n \leq 9.2$

According to the experimental results, the mechanism of magnetic properties of sample at higher Na-concentration seems to be varied depending on the Na-concentration. The distribution of additional Na^+ cations may strongly influent to the electronic states of both supercage and β-cages. At x = 4.0, a model of non-equivalent magnetic sublattices has been proposed in order to explain the N-type ferrimagnetism. In this model the supercage cluster may have a narrowband, with increasing the Fermi energy, s-electron can enter β-cage and localized magnetic moments appear here. Simultaneously, the Fermi energy stays in the narrowband with high density of state and stabilize the itinerant ferromagnetism in supercage clusters network. The energy level of β-cage is considered as lower when compare with that of supercage because most of Na^+ cations are located in β-cage. The antiferromagnetic interaction can be

expected between localized magnetic moments in β-cages and itinerant electrons in supercage network. As a results the N-type ferrimagnetism occurs at specific region of K-loading density n. The situation is changed with only one additional Na^+ cations, as observed at x = 5.1. The fifth Na^+ cations may strongly modify the electronic state of supercage network. The electrical resistivity measurement has confirmed the insulating state of supercage network at x = 5.1. In order to explain the ferrimagnetism at x = 5.1, a co-existence or mixture of itinerant ferromagnetism and close shell state are assumed for supercage clusters network at x = 5.1. Because of higher Na-concentration, the level of supercage can be at lower state when compare with that of x = 4.0. That means higher K-loading density n is required for the formation of localized magnetic moments in β-cages. The disorder ferrimagnetism then realizes at x = 5.1 but the magnetic phase shifts to higher n region. At Na-rich sample x = 7.3, additional Na^+ cations can contribute to supercage network. As a consequence, the spin-singlet states or close shell states are generated in supercage clusters network. The Curie constants are very small at low loading density region. On the other hand, insulating properties are also observed at all of samples. Because of contribution of the sixth and seventh Na^+ cations, the potential of supercage become deeper, the appearance of localized magnetic moments occur at higher K-loading density. The maximum of the Curie constant at x = 7.3 indicates that it is just around 45% of β-cages are occupied by spin-doublet. The remaining β-cage clusters may be in spin-singlet or empty states due to the possibility of inhomogeneous distribution of Na^+ cations. The ferromagnetic ordering of localized magnetic moments in β-cages then can be explained by the model of superexchange interaction. At x = 7.8, there is no observation of long range magnetic ordering. The Curie constants are also very small for all samples. The spin-singlet states are considered to realize in both of supercage and β-cage. Even the optical spectrum imply the appearance of clusters in β-cages, but most of β-cages clusters may be in spin-singlet state because of large electron phonon coupling S, which is caused by large number of Na^+ cations.

In order to have the discussion on the magnetic properties of the system of Na-K alloy clusters in zeolite LSX at higher Na-concentration sample $x \geq 4.0$, it is necessary to take into account the effect of electron – phonon coupling. At first, let me introduce the energy states of empty, one electron occupancy and two electrons occupancy in

the case of considering electron – phonon coupling *S*. As seen in Fig. 4.20 (a), if one electron occupy an empty state together with the influence of electron – phonon coupling *S*, the energy level of one electron occupancy will be - *S*. However due to equivalent one electron occupancy state with different spin direction, the total energy of one electron occupancy would be - 2*S*. In a similar process, the energy of two electrons occupancy is then - 4*S*. However when two electrons occupy a same energy state, we have the Coulomb repulsion *U* between these electrons. As a result, the final energy of two electrons occupancy is *U* - 4*S*. In a simple illustration, the energy difference between two electrons occupancy and one electron occupancy states will be given by subtracting *U* - 4*S* for - 2*S*, and we obtain the energy difference is *U* - 2*S* as shown in Fig. 4.20 (b).

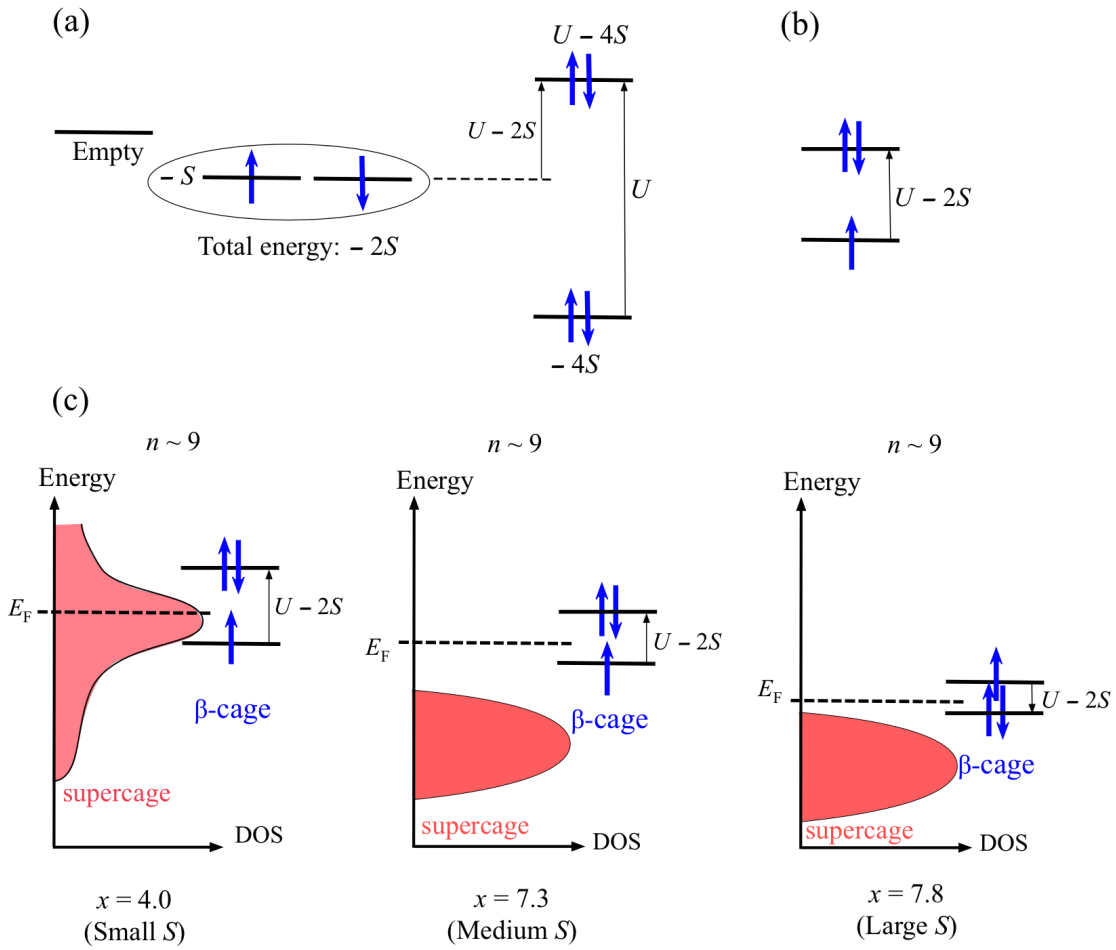

Fig. 4.20. Illustration for the empty, one electron occupancy, two electrons occupancy state with accounting electron-phonon coupling (*S*) (a), energy difference between one and two electrons occupancy states (b), and schematic illustration of electronic state for K_n/Na_xK_{12-x}-LSX with $x \geq 4.0$ at equivalent loading density.

Now let's coming back to the situation for the sample K_n/Na_xK_{12-x}-LSX with $x \geq 4.0$. The samples with Na-concentration $x = 4.0$, $x = 7.3$ and $x = 7.8$ at the same average K-loading density $n = 9$ is considered. The simple illustration of the x dependence is shown in Fig. 4.20 (c). In the case of $x = 4.0$, the supercage cluster has the narrow band with large density of state (DOS) in order to satisfy the condition for the appearance of metallic itinerant ferromagnetism electron network in supercage. The energy of β-cage cluster is assumed to stay near the narrow band of supercage. Because of small contribution of electron – phonon coupling S, $U > 2S$, then the one electron occupancy state is more stable than the of two electrons occupancy. When the Fermi energy increases and stays at the narrow band with large DOS, one electron can occupy the β-cage state. This electron may be expected to have the antiferromagnetic interaction with the itinerant ferromagnetic electron in supercage. As a consequence, the N-type ferrimagnetic properties are observed at $x = 4.0$. If the loading density n is continuously increased, two electrons state will be stabilized and the ferrimagnetic properties are then suppressed. However, the situation is quite different in the case of $x = 7.3$. The number of Na^+ cations increases when compare with that of $x = 4.0$. The additional Na^+ cations will deepen the potential of supercage and raise the effect of electron – phonon coupling S but the one electron occupancy state is still more stable than that of two electrons occupancy. At the K-loading density $n = 9$, the supercage cluster is fully occupied by eight electrons. The supercage cluster forms closed-shell state and insulating network. The ninth electron can be localized in β-cage with increasing the Fermi energy. The localized electrons in β-cages can have the superexchange ferromagnetic interaction with each other via the closed-shell state of supercage clusters. The nearly pure ferromagnetic properties are observed at specific region of n in $x = 7.3$. Similarly with $x = 4.0$, second electron can occupy β-cage and stabilize the non-magnetic cluster here with increasing loading density. As observed in the experimental results, the ferromagnetic properties at $x = 7.3$ disappear at higher loading density $n = 9.7$. At $x = 7.8$, large electron – phonon coupling S strongly vary the electronic state in both of supercage and β-cage. The supercage potential is deeper that that of $x = 7.3$ while two electrons occupancy state becomes more stable in β-cage because of large S, $U < 2S$. Therefore, the non-magnetic state is stabilized at $x = 7.8$. There is no evidence of magnetic ordering and small values of the Curie constant have been observed at any K-loading density n.

Chapter V
Summary

5.1 Summary

The Na-rich sample $K_n/Na_{7.3}K_{4.7}$-LSX (x = 7.3) has been successfully prepared at various loading densities n from dilute to saturation one. The magnetic, optical, electric transport properties of these samples were investigated in details.

Nearly pure ferromagnetic properties have been observed at $8.6 \leq n \leq 9.5$. The Curie constant shows the increasing and decreasing, implying the formation of localized magnetic moment consistently with the appearance of ferromagnetic phase. The Curie constant shows a narrow peak at $n \sim 9$ and the maximum value of Curie constant corresponds to 45% occupancy of magnetic moments with spin ½ in β-cage. In addition, the ferromagnetic phase shift to higher region of K-loading density when compare with that of ferrimagnetic phase observed in K-rich samples K_n/Na_xK_{12-x}-LSX ($x \leq 4.0$).

The optical absorption spectrum of dilute Na-rich samples $K_n/Na_{7.3}K_{4.7}$-LSX (x = 7.3) shows a continuous absorption band at lower photon energy region and a significant absorption band at ≈ 2.6 eV. These results indicate the formation of clusters in both supercages and β-cages. For higher loading density samples of Na-rich $K_n/Na_{7.3}K_{4.7}$-LSX (x = 7.3), the optical reflectance spectra exhibit the appearance of reflection bands at ≈ 2.4 eV for samples with loading density $n < 8$. The growth of new reflection bands at ≈ 2.8 eV is seen for samples with loading density $n > 8$. Both of reflection bands at ≈ 2.4 and ≈ 2.6 eV are attributed to excitation of s-electron in β-cage clusters, but the spin states of these clusters are spin singlet and doublet states, respectively. The growth of reflection bands at ≈ 2.8 eV coincides with increasing and decreasing of Curie constant. Therefore the magnetic moments are assigned to magnetic electrons in β-cage clusters.

The electrical resistivity measurements for Na-rich samples $K_n/Na_{7.3}K_{4.7}$-LSX (x = 7.3) have revealed that all of samples are basically in insulating state. Thermal hysteresis behavior has been observed in some samples however the thermal

hysteresis may have no relation with the magnetic properties of sample. The origin of the thermal hysteresis may be attributed to some structural changes.

According the insulating nature of Na-rich samples $K_n/Na_{7.3}K_{4.7}$-LSX (x = 7.3), the mechanism of long range magnetic ordering in these samples can come from an indirect exchange interaction because rarely interaction between magnetic moments in neighbor β-cage clusters. A model of superexchange ferromagnetic interaction has been proposed in order to explain the ferromagnetic properties of Na-rich samples $K_n/Na_{7.3}K_{4.7}$-LSX (x = 7.3). In this model, the localized magnetic moments are realized in β-cage clusters at higher K-loading density n. The magnetic interaction between these localized magnetic moments is provided by superexchange ferromagnetic interaction through sp^3-like state of supercage clusters.

In addition, the investigation on the optical, the magnetic and the electric transport properties of the intermediate Na-concentration sample $K_n/Na_{5.1}K_{6.9}$-LSX (x = 5.1) at various K-loading densities has also been carried out. The optical absorption spectrum of dilute loading density sample for $Na_{5.1}K_{6.9}$-LSX (x = 5.1) show similar behavior with that of K-rich samples $x \leq 4.0$, where the observed continuous absorption bands are assigned to the formation of supercage clusters. The optical reflectance spectra of $K_n/Na_{5.1}K_{6.9}$-LSX (x = 5.1) at various loading density up to saturated sample with n = 9.3 exhibits the appearance of reflection bands at 2.4 and 2.8 eV. These kind reflection bands are also found in the case of sample with x = 7.3 and are basically attributed to the excitation of electrons in β-cage clusters. The growth of reflection bands at 2.8 eV is consistent with the increasing in the Curie constant as well as the appearance of spontaneous magnetization.

The spontaneous magnetization has been observed in $K_n/Na_{5.1}K_{6.9}$-LSX (x = 5.1) at $8.2 \leq n \leq 8.9$. The shape of temperature dependence of magnetization and the observed spin-flop behavior indicate the ferrimagnetic properties of these samples. In addition, interesting behavior of the Curie constant likely intermediate behavior between K-rich samples $x \leq 4.0$ and Na-rich sample x = 7.3. On the other hand, the insulating states are confirmed for all of samples with x = 5.1. In order to understand the ferrimagnetic properties of samples with x = 5.1 at higher K-loading density n in the insulating scene, a consideration on the disorder ferrimagnetic properties with the

Anderson localization state of supercage clusters network and localized magnetic moments in β-cage clusters network has been proposed.

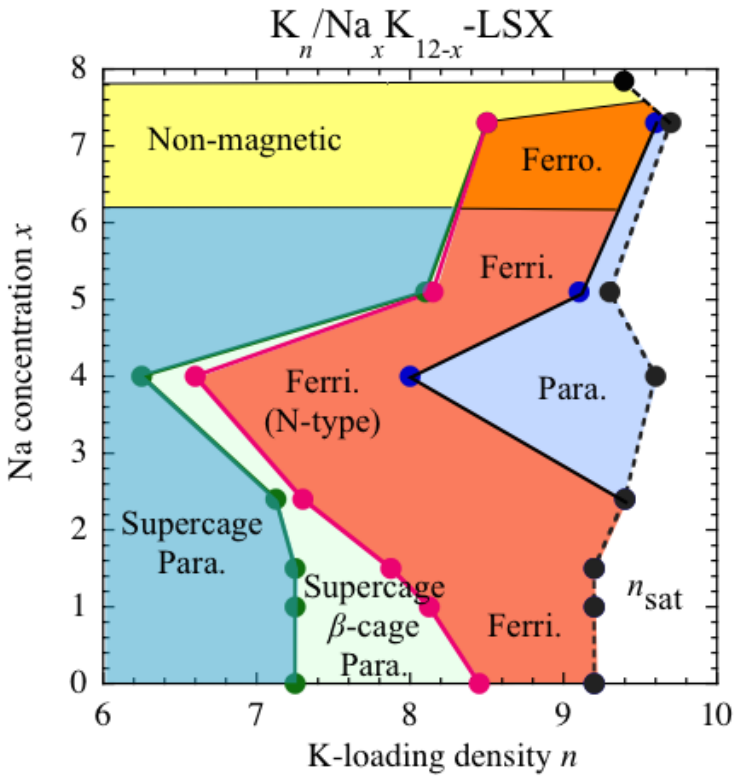

Fig. 5.1. Phase diagram of magnetic properties of sample system K_n/Na_xK_{12-x}-LSX.

The phase diagram of magnetic properties of sample system K_n/Na_xK_{12-x}-LSX is shown in Fig. 5.1. According to the experimental results, with increasing Na-concentration, the disorder ferrimagnetism and nearly pure ferromagnetism have been observed in $K_n/Na_{5.1}K_{6.9}$-LSX (x = 5.1) and $K_n/Na_{7.3}K_{4.7}$-LSX (x = 7.3) samples, respectively. Differently with K-rich samples $x \leq 4.0$, the ferrimagnetic and ferromagnetic phase tend to be shifted to higher K-loading density region with increasing Na-concentration. Above x = 4.0, the addition Na^+ cations strongly vary the electronic state of supercage and β-cage clusters network. At low loading density region, the addition Na^+ cations may modify the supercage network as observed in the changing from paramagnetic state to non-magnetic state of supercage clusters as well as the changing in the electronic transport properties. At higher loading density, instead of pure ferrimagnetism, the magnetic properties of sample system K_n/Na_xK_{12-x}-LSX systematically vary to disorder ferrimagnetic and then to nearly pure

ferromagnetic properties at intermediate Na-concentration sample x = 5.1 and Na-rich sample x = 7.3. A consideration on the variability of electronic state of clusters, which caused by the number of Na^+ cations, is needed to take account. At K-rich samples, the localized magnetic moments in β-cage clusters network stabilize the itinerant ferromagnetic supercage clusters network and cause ferrimagnetic properties. At higher Na-concentration samples, the appearance of localized magnetic moments in β-cage clusters network requires higher loading density because the potential balance between β-cage and supercage has been changed by the influence of number Na^+ cations to supercage network. In addition the supercage cluster network is modified to co-existence of itinerant ferromagnetic and non-magnetic state. As a results, when the localized magnetic moments realizes in β-cage, we observed the disorder ferrimagnetic properties in samples with x = 5.1. Higher Na-concentration, the number of Na^+ cations caused the non-magnetic state for supercage network due to high electron-phonon coupling, as a results the superexchange ferromagnetism has been found at x = 7.3. These results clearly show us the sensitivity of magnetic properties of of sample system K_n/Na_xK_{12-x}-LSX to the Na-concentration x and K-loading density n. At x = 7.8, there is no observation of magnetic ordering at all any value of K-loading density n.

5.2 Future research plans

As mention earlier, in the samples system K_n/Na_xK_{12-x}-LSX the distribution cations themselve in unloaded sample as well as the changing in location of cations depend on K-loading density n are important factors because they directly affect the electronic state of clusters in supercage and β-cage. The detailed investigation of the cations distribution is expected to help clarify the properties of system.

In addition, beside of intermediate Na-sample $K_n/Na_{5.1}K_{6.9}$-LSX (x = 5.1) and Na-rich sample $K_n/Na_{7.3}K_{4.7}$-LSX (x = 7.3), the studies on other samples at higher Na-concentration (x > 4.0) are worthwhile to carry out in order to understand the role of Na-concentration on the magnetic properties of samples system K_n/Na_xK_{12-x}-LSX.

List of references

[1] F. A. Cotton, Inorg. Chem. **3 (9)**, 1217 (1964).

[2] W.A. de Heer, Rev. Mod. Phys. **65**, 611 (1993).

[3] P.W. Robbins, D. Bray, M. Dankert, A. Wright Science. **158**, 1536 (1967).

[4] R. Kubo, J. Phys. Soc. Jpn. **17**, 975 (1962).

[5] W.D. Knight, K. Clemenger, W.A. de Heer, W.A. Saunders, M.Y. Chou, and M.L.

Choen, Phys. Rev. Lett. **52**, 2141 (1984).

[6] W. Ekardt, Phys. Rev. B **29**, 1558 (1984).

[7] W.P. Halperin, Rev Mod Phys. **58**, 533(1993).

[8] T. Welker and T.P. Martin, J Chem Phys **70**, 5683 (1979).

[9] Y. Nozue, T. Kodaira, and T. Goto, Phys. Rev. Lett. **68**, 3789 (1992).

[10] Y. Nozue, T. Kodaira, S. Ohwashi, T. Goto, and O. Terasaki, Phys. Rev. B **48**, 12253 (1993).

[11] T. Nakano and Y. Nozue, J. Comput. Meth. Sci. Eng. **7**, 443 (2007).

[12] T. Nakano, Y. Ikemoto, and Y. Nozue, J. Magn. Magn. Mater. **226-230**, 238 (2001).

[13] T.C. Duan, T. Nakano, and Y. Nozue, J. Magn. Magn. Mater. **310**, 1013 (2007).

[14] T.C. Duan, T. Nakano, and Y. Nozue, e-J. Surf. Sci. Nanotech. **5**, 6 (2007).

[15] T.C. Duan, PhD dissertation, Osaka University, 2008.

[16] V.I. Srdanov, G.D Stucky, E. Lippmaa, and G. Engelhardt, Phys. Rev. Lett. 80, 2449 (1998).

[17] T. Nakano, M. Matsuura, A. Hanazawa, K. Hirota, and Y. Nozue, Phys. Rev. Lett. **109**, 167208 (2012).

[18] T. Nakano, R. Suehiro, A. Hanazawa, K.Watanabe, I.Watanabe, A. Amato, F. L. Pratt, and Y. Nozue, J. Phys. Soc. Jpn. **79**, 073707-1 (2010).

[19] D. T. Hanh, T. Nakano, and Y. Nozue, J. Phys. Chem. Solids **71**, 677 (2010).

[20] T. Nakano, K. Goto, I. Watanabe, F. L. Pratt, Y. Ikemoto, and Y. Nozue, Physica B 374-375, **21** (2006).

[21] T. Nakano, D. T. Hanh, Y. Ohwaki, Y. Nozue, N. H. Nam, and S. Araki, J. Kor. Phys. Soc. **63**, 512 (2013).

[22] T. Nakano, D. T. Hanh, Y. Nozue, N. H. Nam, T. C. Duan, and S. Araki, J. Kor. Phys. Soc. **63**, 699 (2013).

[23] A. F. Cronsted, Akad. Handl., Stockholm, 18 (1756) 120. Source: E. M. Flanigen, "Introduction to Zeolite Science and Practice", 2nd edition, Elsevier Science, Amsterdam, 9 (2001).

[24] Zeolite (natural), USGS Mineral Commodity Summaries (2011).

[25] D. W. Break, "Zeolite Molecular Sieves", Krieger, Malabar, Florida (1984).

[26] R. M. Barrer, Pure and Appl. Chem. **51**,1091 (1979).

[27] L .B. McCusker, F. Liebau and G. Engelhardt, Pure and Applied Chemistry (2001).

[28] J. Ward, W. J. Catal. **9**, 225 (1967).

[29] Chapter 3, Introduction to Zeolite Science and Practice, 2nd edition, Elsevier Science, Amsterdam. p. 37 (2001).

[30] P. C. Leung, K. B. Kunz, K. Seff, and I. E. Maxwell, J. Phys. Chem. **79**, 2157 (1975).

[31] J. V. Smith and J. M. Bennett, Am. Mineral. **66**, 777 (1981).

[32] Ch. Baerlocher, W. M. Meier and D. H. Olson, "Atlas of Zeolite Framework Types", 5th edition, Elsevier, London (2001).

[33] Y. Lee, S. W. Carr, and J. B. Parise, Chem. Mater. **10**, 2561 (1998).

[34] H. Guesmi, P. Massiani, H. Nouali, and J. L. Paillaud, Micropor. Mesopor. Mater. **159**, 87 (2012).

[35] G. Vitale, C. F. Mellot, L. M. Bull, and A. K. Cheetham, J. Phys. Chem. B **101**, 4559 (1997).

[36] P. E. Pickert, J. A. Rabo, E. Dempsey, and V. Schomaker, Proc. Intern. Congr., 3rd Amsterdam **1**, 714 (1964).

[37] T. Kodaira, Y. Nozue, S. Ohwashi, T. Goto and O. Terasaki, Phys. Rev. B **48**, 12245 (1993).

[38] T. Nakano, PhD Dissertation, Tohoku University (2001).

[39] T. Nakano, Y. Ikemoto and Y. Nozue, Eur. Phys. J. D **9**, 505 (1999).

[40] T. Nakano, Y. Ikemoto and Y. Nozue, Physica B **281&282**, 688 (2000).

[41] T. Nakano, D. Kiniwa, A. Matsuo, K. Kindo and Y. Nozue, J. Mag.

Mag. Mat. 310, e295 (2007).

[42] I. Dzyaloshinsky, J. Phys. Chem. Solids 4, 241 (1958).

[43] T. Moriya, Phys. Rev. Lett. 4, 228 (1960).

[44] T. Moriya, Phys. Rev. 120, 91 (1960).

[45] M. Tachiki, J. Phys. Soc. Jpn. 25, 686 (1968).

[46] N. P. Blake, V. I. Srdanov, G. D. Stucky and H. Metiu, J. Chem. Phys. 104, 8721 (1996)

[47] P. H. Kasai, J. Chem. Phys. **43**, 3322 (1965).

[48] J. A. Rabo, C. L. Angell, P. H. Kasai and V. Schomaker, Discuss. Faraday Soc. **41**, 328 (1966).

[49] J. A. Rabo and P. H. Kasai, Prog. Solid State Chem. **9**, 1 (1975).

[50] Y. Ikemoto, T. Nakano. M. Kuno and Y. Nozue, Mol. Cryst. And Lid. Cryst. **341**, 453 (2000).

[51] R. M. Barrer and J .F. Cole, J. Phys. Chem. Solids **29**, 1755 (1968).

[52] V. I. Srdanov, K. Haug, H. Metiu and G. D. Stucky, J. Phys. Chem. **96**, 9039 (1992).

[53] A. R. Armstrong, P. A. Anderson, L. J. Woodall and P. P. Edwards, J. Am. Chem. Soc. **117**, 9087 (1995).

[54] L. J. Woodall, P. A. Anderson, A. R. Armstrong and P. P. Edwards, J. Chem. Soc., Dalton Trans. 719 (1996).

[55] P. P. Edwards, M. R. Harrison, J. Klinowski, S. Ramdas, J. M. Thomas, D. C. Johnson and C. J. Page, J. Chem. Soc., Chem. Commun. 982 (1984).

[56] Ikemoto, T. Nakano and Y. Nozue, Proceedings of the 12th International Zeolite Conference, Baltimore, 1998, Material Research Society, **3**, 2103 (1999).

[57] Y. Ikemoto, T. Nakano, M. Kuno, Y. Nozue and T. Ikeda, J. Magn. Magn. Mater. **226-230**, 299 (2001).

[58] Y. Ikemoto, PhD Dissertation, Tohoku University (1997).

[59] T. Nakano, T. Mizukane and Y. Nozue, J. Phys. Chem. Solids **71**, 650 (2010).

[60] Y. Nozue, Y. Amako, R. Kawano, T. Mizukane and T. Nakano, J. Phys. Chem. Solids **73**, 1538 (2012).

[61] Y. Toyozawa, Prog. Theor. Phys. **26**, 29 (1961).

[62] C. Higashikawa, Master Thesis, Osaka University (2006).

[63] T. Nakano, D. T. Hanh, Y. Ohwaki, Y. Nozue, N. H. Nam and S. Araki, J. Korean Phys. Soc. **63**, 512 (2013).

[64] T. Nakano, K. Goto, I. Watanabe, F. L. Pratt, T. Ikemoto and Y. Nozue, Physica B **374-375**, 21 (2006).

[65] D. T. Hanh, T. Nakano and Y. Nozue, J. Phys. Chem. Solids **71**, 677 (2010).

[66] D. T. Hanh, PhD Dissertation, Osaka University (2009).

[67] T. Nakano, D.T. Hanh, Y. Ohwaki, Y. Nozue, N. H. Nam, T. C. Duan and S. Araki, J. Korean Phys. Soc. **63**, 699 (2013).

[68] W. Heisenberg, Z. Phys. **49**, 619 (1928).

[69] C. G. Shull and J. S. Smart, Phys. Rev. **76**, 1256 (1948).

[70] P. W. Anderson, Phys. Rev. **79**, 350 (1950).

[71] H. A. Kramers, Physica **1**, 182 (1934).

[72] M. Suzuki and I. S. Suzuki, Lecture note on solid state physics – Superexchange interaction (2009).

[73] M. Opel, J. Phys. D: Appl. Phys. **45**, 033001 (2012).

[74] G. T. Rado and H. Suhl, Magnetism, Academic Press, New York (1963).

[75] P. W. Anderson, Phys. Rev. **115**, 2 (1959).

[76] J. Kanamori, Magnetism, Baifukan, Tokyo (1969).

[77] J. B. Goodenough, Phys. Rev. **100**, 564 (1955).

[78] J. Kanamori, J. Phys. Chem. Solid **10**, 87 (1959).

[79] Quantum Design, MPMS XL Optional Manual (1999).

[80] P. Kubelka and F. Munk, Z. Tech. Phys. **12**, 593 (1931).

[81] E.V. Charnaya, M.K. Lee, C.Tien L. J. Chang, Z.-J.Wu, Y. A.Kumzerov, and A. S. Bugaev, Phys. Rev. B **87**, 155401 (2013).

[82] T. Ikeda, T. Nakano, and Y. Nozue, J. Phys. Chem. C **118**, 23202 (2014).

[83] M. Igarashi, T. Nakano, P. T. Thi, Y. Nozue, A. Goto, K. Hashi, S. Ohki, T. Shimizu, A. Krajnc, P. Jegliˇc, and D. Arˇcon, Phys. Rev. **87**, 075138 (2013).

[84] M. Tchaplyguine, S. Legendre, A. Rosso, I. Bradeanu, G. Ohrwall, S. E. Canton, T. Andersson, N. Mårtensson, S. Svensson, and O. Bjorneholm, Phys. Rev. B **80**, 033405 (2009).

[85] G. Vitale, C. F. Mellot, L. M. Bull, and A. K. Cheetham, J. Phys. Chem. B **101**, 4559 (1997).

[86] K. Nakamura, T. Koretsune and R. Arita, Phys. Rev. B **80**, 174420 (2009).

[87] G. Stollhoff and P. Fulde, J. Chem. Phys. **73**, 4548 (1980).

[88] F. Pfirsch, M.C. Bohm and P. Fulde, Z. Phys. B **60**, 171 (1985).

[89] P. Fulde, Correlated Electrons in Quantum Matter, World Scientific Publishing, (2012).

[90] J. Weikamp and L. Puppe, Catalysis and Zeolite: Fundamental and applications, Spinger, Berlin, 128 (1999).

[91] T. Goto, Master Thesis, Osaka University (2011).

Publications

I. Peer reviewed paper

- L. M. Kien, T. Goto, D. T. Hanh, T. Nakano and Y. Nozue, "Ferromagnetism of Na-K alloy clusters incorporated in zeolite low-silica X", Journal of the Physical Society of Japan **84**, 064718 (2015).

II. Presentations

1. L. M. Kien, T. Goto, D. T. Hanh, T. Nakano and Y. Nozue, "Electrical resistivity and magnetic properties of Na-K alloy clusters in zeolite LSX", Oral presentation at the spring meeting of The Physical Society of Japan (Abstract no. 24pAC-4), Tokyo, Japan (2015).
2. L. M. Kien, T. Goto, D. T. Hanh, T. Nakano and Y. Nozue, "Ferromagnetic and optical properties of Na-K alloy clusters in zeolite LSX II", Oral presentation at the autumn meeting of The Physical Society of Japan (Abstract no. 9aAL-2), Nagoya, Japan (2014).
3. L. M. Kien, T. Goto, D. T. Hanh, T. Nakano and Y. Nozue, "Magnetic and optical properties of Na-K alloy clusters in zeolite LSX", Oral presentation at the spring meeting of The Physical Society of Japan (Abstract no. 27pAN-3), Kanagawa, Japan (2014).
4. L. M. Kien, T. Goto, D. T. Hanh, T. Nakano and Y. Nozue, "Magnetic properties of Na-K alloy clusters in Na-rich low-silica X zeolite", Poster presentation at the International Symposium on Frontiers in Materials Science (Poster no. PO1.54), Hanoi, Vietnam (2013).
5. L. M. Kien, T. Goto, D. T. Hanh, T. Nakano and Y. Nozue, "Magnetic properties and electrical resistivity of Na-K alloy clusters in zeolite LSX at high Na concentration II", Oral presentation at the autumn meeting of The Physical Society of Japan (Abstract no. 27pDF-3), Tokushima, Japan (2013).
6. L. M. Kien, T. Goto, D. T. Hanh, T. Nakano and Y. Nozue, "Magnetic properties of Na-K alloy clusters incorporated in low-silica X zeolite at higher

Na-concentration", Poster presentation at the International Symposium of Intercalation Compounds (Poster no. PII-30), Sendai, Japan (2013).

7. L. M. Kien, T. Goto, D. T. Hanh, T. Nakano and Y. Nozue, "Magnetic properties and electrical resistivity of Na-K alloy clusters in zeolite LSX at high Na concentration", Oral presentation at the spring meeting of The Physical Society of Japan (Abstract no. 26aXF-2), Hiroshima, Japan (2013).
8. L. M. Kien, T. Goto, D. T. Hanh, T. Nakano and Y. Nozue, "Magnetism of Na-K alloy clusters in zeolite LSX at higher Na-concentrations III", Oral presentation at the autumn meeting of The Physical Society of Japan (Abstract no. 18pEC-2), Yokohama, Japan (2012).
9. L. M. Kien, T. Goto, D. T. Hanh, T. Nakano and Y. Nozue, "Magnetic properties of Na-K alloy clusters in zeolite LSX at high Na concentration", Poster presentation at the International Workshop on Advanced Materials and Nanotechnology (Poster no. P36), Hanoi, Vietnam (2012).
10. L. M. Kien, T. Goto, D. T. Hanh, T. Nakano and Y. Nozue, "Magnetism of Na-K alloy clusters in zeolite LSX at higher Na-concentrations II", Oral presentation at the autumn meeting of The Physical Society of Japan (Abstract no. 22aTD-3), Toyama, Japan (2011).